CONSTRAINING PORE PRESSURE PREDICTION USING SEISMIC INVERSION

A Thesis

by

HAIDER ABDULAAL H AL ABDULAAL

Submitted to the Office of Graduate and Professional Studies of
Texas A&M University
in partial fulfillment of the requirements for the degree of

MASTER OF SCIENCE

Chair of Committee,	Richard L. Gibson, Jr.
Committee Members,	Mark Everett
	Walter Ayers
	Bobby Reece
Head of Department,	Michael Pope

May 2016

Major Subject: Geophysics

ABSTRACT

This paper addresses utilizing borehole acoustic logs to predict pore pressure at the borehole and employing seismic inversion to extrapolate these predictions. We implemented common approaches with our proposed quality control steps to constrain the pore pressure prediction at the borehole using acoustic logs and normal compaction trend analysis. We formulated a research method to enable integration of multidisciplinary data sets with different scales to constrain our prediction.

The contribution of the research is that it adapts post-stack deterministic and stochastic seismic inversion within a user-defined mesh based on geological settings in order to predict pressure. The study was carried out on offshore data from the Gulf of Mexico, where undercompaction is considered the primary source of overpressure. Results within connected sand bodies showed relatively close numerical pressure values when compared to disconnected sand bodies. The predicted pressure gradient could be used to infer pressure across specific formations along a vertical wellbore trajectory.

DEDICATION

To my parents who gave me the gift of life,

To my wife who lovingly shares my life,

And my friends who defined my life.

ACKNOWLEDGEMENTS

This research could not have been possible to pursue without the tremendous help, guidance and patience of my advisor, Dr. Richard L. Gibson, Jr. I had a great opportunity to learn a lot from him, as he always kept his door, thoughts and heart open for his students. Without a doubt, I am a better scientist today because I have the opportunity to work with him. I wish also to acknowledge my committee members: Dr. Mark E. Everett, Dr. Bobby Reece and Dr. Walter Ayers, all of whom I highly admire and whose feedback is greatly appreciated. In addition, I cannot forget to mention the help from Dr. Nurul Kabir who pushed me to seek the complete solution.

Amberjack data sets utilized in this paper were provided compliments of CGG. I am also grateful for CGG GeoSoftware who donated the software. Specifically, I would like to thank Mr. Robert Chelak from CGG who helped in providing the data and Mr. Sanjeev Kumar from CGG/Jason who helped with technical support.

I also wish to express my gratitude to the Ministry of Education in Saudi Arabia, who funded my studies under King Abdullah's scholarship program. Special thanks to Dr. Mohammed Alfaraj, Mr. Mohammed Nemer, Dr. Mohammed G. Al-Otaibi, Dr. Abdullah Alramadhan, Mr. Riyadh Alsaad and Dr. Aiman Bakhorji of Saudi Aramco who tremendously encouraged me to pursue graduate studies.

NOMENCLATURE

NCT	Normal Compaction Trend
RPM	Rock Physics Model
P	Pressure
t	Time
V_p	Compressional Velocity
P_{ob}	Overburden Pressure
P_c	Confining Pressure
P_c	Confining Pressure
P_d	Differential Pressure
P_e	Effective Pressure
P_p	Fluid Pore Pressure
α	Attenuation
π	3.14159265359
f	Frequency (Hz)
ω	Angular Frequency (rad/sec)
C	Clay Content (Fraction)
ϕ	Porosity (Fraction)
M	Elastic Modulus
σ	Total Stress
σ'	Effective Stress
ρ	Density
g	Gravitational Acceleration = 9.81 m/s

GOM	Gulf of Mexico
RFT	Repeat Formation Test
MDT	Modular Formation Test
FMT	Formation Multi Test
DST	Drill Stem Test
psi	Pound Per Square Inch = 6894.757 N/m^2
MCMC	Markov Chain Monte Carlo
CSSI	Constrained Sparse Spike Inversion
QC	Quality Control/Quality Check
CPU	Computer Processing Unit
CMP	Common Mid-Point
AI	Acoustic Impedance
PDF	Probability Distribution Function
CDF	Cumulative Distribution Function
AVO	Amplitude Versus Offset
EP	Effective Pressure
L.R.	Linear Regression
SGS	Sequence Gaussian Simulation
GR	Gamma Ray
RMS	Root Mean Sequare
CGG	Compagnie Générale de Gophysique
Hz	Hertz
m	Meters
ms	Millisecond
s	Second

TABLE OF CONTENTS

Page

ABSTRACT ii

DEDICATION iii

ACKNOWLEDGEMENTS iv

NOMENCLATURE v

TABLE OF CONTENTS vii

LIST OF FIGURES ix

1. INTRODUCTION 1

2. DATASET 3

2.1 Seismic 3
2.2 Wellbore Logs 3
2.3 Geological Background 7

3. RESEARCH METHODS 10

3.1 Borehole Pressure Analysis 12
3.1.1 Terzaghi's Principle 12
3.1.2 Direct Pressure Measurement Methods 14
3.1.3 Indirect Pressure Prediction Methods 14
3.1.4 Normal Compaction Trend Analysis 16
3.1.5 Bowers's Equation 18
3.1.6 Eaton's Equation 18
3.2 Seismic Inversion 19

4. RESULTS 23

4.1 Acoustic Impedance Inversion on the field data 24
4.1.1 Post-Stack Deterministic Inversion 24
4.1.2 Post-Stack Geostatistical Inversion 29
4.2 Wellbore Pressure Predicition 37
4.3 Spatial Pressure Prediction 39

4.3.1 Linear Regression Method 41
4.3.2 Cosimulation Method 45

5. CONCLUSION 55

REFERENCES 61

APPENDIX A. FIGURES 67

APPENDIX B. COMPUTER CODES 93

B.1 Pore Pressure Prediction at the Borehole: MATLAB Script 93
B.2 Log View and Crossplot: MATLAB Script 99

LIST OF FIGURES

FIGURE Page

2.1 Well locations and seismic data coverage. The green line represent a zigzag line generated from the seismic data, which we used to present the study in this paper. 4

2.2 Log view plots showing gamma ray [gAPI] within the depth of interest in red rectangular at each well. We can observe three layers within our interval as the following: (1) low gamma ray (reservoir), (2) moderate gamma ray (shaley sand) and (3) moderate to high gamma ray (shale cap). 5

2.3 Cross plot showing acoustic impedance versus density colored by gamma ray in the depth of interest. Here, we can segregate the major three layers within our interval as the following: (1) low impedance, low gamma ray and slow velocity porous sand (reservoir), (2) medium impedance, moderate gamma ray and moderate to high velocity shaley sand, (3) high impedance, moderate to high gamma ray with high velocity shale cap 6

2.4 Easting 2D zigzag seismic line representation going through Wells-1,3 and 4. Two horizons where picked above and below providing a time window of around 150 ms. The observed lateral displacement is believed to be caused by deep normal faults which is interpreted as a graben. 8

2.5 Seismic amplitude root mean square attribute for the defined 150 ms interval. The wells appeare to target the high RMS amplitude, which could represent the porous hydrocarbon-filled sand reservoir. A zigzag line was generated between the wells to illustrate results. 9

3.1 Research methodology consists of two stages. The first is the inversion stage which has two workflows which produce deterministic inversion based on CSSI and a stochastic inversion based on MCMC. Then, a second stage is implemented where we apply pressure analysis at the borehole first using Eaton's Equation and Bowers's equation. Those analyses were extrapolated beyond the borehole using two methods: the linear regression method and the statistical cosimulation method which were both transform acoustic impedance into effective pressure. 11

3.2 Pore pressure, hydrostatic pressure and lithostatic pressure versus depth. 13

3.3 Schematic diagram showing the normal compaction trend analysis on compressional velocity borehole log and its relation to pore pressure. . 17

3.4 A schematic three layers mesh model based on strata interpretation on the wedge model. Those layers are interpolated based on the mechanism of the deposition. Hence, each individual cell would be filled with the inversion process while taking into account the geological observations of the subsurface. This example illustrates a reservoir that onlap on the base layer. 22

4.1 Three Layers Mesh model based on seismic strata interpretation. Those layers are interpolated based on the mechanism of the deposition. Hence, each individual cell would be filled with the inversion process while taking into account the geological observations of the subsurface. 24

4.2 Low frequency model overlaid on top of the previously defined mesh model. The low frequency is derived from the control points (vertical wells) in this case. The mesh boundary and cell shape define the extent of the filling of each cell. Hence, honor the geological observation of the subsurface 25

4.3 Deterministic inversion in frequency domain. Merging the three different data yield a wider frequency contribution in frequency domain which would translate into a shaper wiggles in time domain, which increases the resolution of the trend merged inverted result. 26

4.4 Deterministic result at Well-1: Wellbore log measured acoustic impedance in black and inverted impedance using CSSI in blue. 28

4.5 Geostatistical inversion in frequency domain. Merging the three different data yield a wider frequency contribution in frequency domain which would translate into a shaper wiggles in time domain. This increases the resolution of the output results compared to the initial input (Modified from Dubrule, 2003). 29

4.6 Different variogram models. Reprinted from (Bohling, 2005). 32

4.7 Acoustic impedance vertical and horizontal variogram. 33

4.8 Mean of 10 simulated realizations. Simulation uses well data only and produce a geostatistical representation of the possible outcomes of the statistical heterogeneity. 34

4.9 Frequency analysis for the inverted impedance. (A-I): frequency vs. offset plot for the deterministic inversion solution, (A-II): deterministic inversion, (B-I): frequency vs. offset plot for the stochastic inversion solution and (B-II): stochastic inversion. 36

4.10 Cross plot showing acoustic impedance versus compressional velocity colored by density. Density color bar shows a linear density trend. We can also segregate three layers here: low density (potentially due to hydrocarbon) medium density and highly dense material (low porosity shaley sand). 38

4.11 Petrophysical curves plotted against depth. From left to right: (1) Compressional velocity and normal compaction trend, (2) Density, (3) Bowers's equation pore pressure (red) bounded by overburden (green) and hydrostatic pressure (blue), and (3) Eaton's equation pore pressure (blue) bounded by overburden (green) and hydrostatic pressure (red). The plot also shows results of correlation between velocity and pressure as higher velocities correlated with higher pore pressure based on the color coded points. 39

4.12 Cross plot of Eaton's equation pore pressure result vs. Bowers's equation pore pressure results color coded by compressional velocity. To visualize the similarity between the two methods, we plotted the 45-degree line to help interpret results. The estimate of the Bowers pressure is larger than the Eaton pressure estimate for values less than 6000 psi, and slightly underestimated for pressure values greater than 8000 psi. 40

4.13 Cross plot between Bowers's predicted pore pressure and Eaton's predicted pore pressure at the borehole colored by the measured density at the borehole. Density color bar shows a linear density trend and negligible variance between 4000-6000 psi. 41

4.14 The linear regression of effective pressure (in units of psi) as a function of acoustic impedance ($kg/m^3 \times m/s$) color coded by density. Linear regression showed a 67% correlation between the two properties. . . . 43

4.15 Effective pressure as a function of acoustic impedance, colored by density 44

4.16 Aerial weighted interpolation of the calculated effective pressure using wellbore data. This interpolation uses the logs only and populate the result in the stratigraphic mesh. Hence, no seismic nor inversion is used here. 48

4.17 Effective pressure calculated using the linear regression approach based on the deterministic acoustic impedance inversion. 49

4.18 Effective pressure calculated using the linear regression approach based on the mean of the 10 realizations of the geostatistically inverted acoustic impedance volume. 50

4.19 Experimental and modeled vertical variograms for effective pressure at the reservoir layer. 51

4.20 Cosimulation a priori statistical model, the probability density function at the well location based on the calculated effective pressure. PDFs are segregated based on a previously defined lithology. 52

4.21 Effective pressure section view through Wells-1,3 and 4 using (A) log aerial weighted interpolation, (B) linear regression tranformation (deterministic inversion), (C) linear regression transformation (geostatistical inversion) and (D) cosimulated transformation (geostatistical inversion). 53

4.22 Effective pressure calculated using the cosimulation approach based on the mean of the 10 realization of the geostatistically inverted acoustic impedance volume. 54

5.1 Deterministic inversion final results using CSSI. 56

5.2 Stochastic inversion final results using MCMC. 57

5.3 Effective pressure at Well-1: wellbore calculated effective pressure in blue versus Morris et. al (2015) reconstructed geostatistical pressure gradient curve in green. 58

A.1 Normal compaction trend analysis for the 5 wells. The three vertical wells show similar trend while the side track wells are off. A global NCT was derived based on the three vertical wells only. Note that only Well-1 has compressional sonic log to the surface. 68

A.2 Eaton's vs. Bowers's pore pressure prediction at borehole (Well-1). . 69

A.3 Eaton's vs. Bowers's pore pressure prediction at borehole (Well-3). . 70

A.4 Eaton's vs. Bowers's pore pressure prediction at borehole (Well-4). . 71

A.5 Eaton's vs. Bowers's pore pressure prediction across Well-1, 3, 3ST, 4 and 4ST. Eaton's pore pressure in in red and Bowers's pore pressure is in magenta. 72

A.6 Cross plot showing acoustic impedance versus compressional velocity colored by density. Density color bar shows a linear density trend. We can also segregate three layers here: low density (potentially due to hydrocarbon) medium density and highly dense material (low porosity shaley sand). 73

A.7 Cross plot showing acoustic impedance versus density colored by gamma ray. Here, we can segregate the major three layers within our interval as the following: (1) low impedance, low gamma ray and slow velocity porous sand (reservoir), (2) medium impedance, moderate gamma ray and moderate to high velocity shaley sand, (3) high impedance, moderate to high gamma ray with high velocity shale cap 74

A.8 2D Seismic line. Nota bene that there is a 280 m offset between Well-1 and the seismic line and 180 m offset between the line and Well-3. GR logs are plotted with frequency cut at 80 Hz. 75

A.9 Seismic facies interpretation (Mayall et al., 1992). 75

A.10 Low frequency model overlaid on top of the previously defined mesh model. The low frequency is derived from the control points (vertical wells) in this case. The mesh boundary and cell shape define the extent of the filling of each cell. Hence, honor the geological observation of the subsurface 76

A.11 Deterministic inversion results using CSSI algorithm: cross section view between Well-1, 3 and 4. Results are displayed in acoustic impedance colorbar and plotted on top of a wiggle raw seismic input to illustrate the amplitude vs. acoustic impedance correlation. . . 77

A.12 Deterministic inversion results using CSSI algorithm: cross section view between Well-1, 3 and 4. Results are displayed in acoustic impedance colorbar. A 80 Hz high frequency cut filter was applied to the wellbore acoustic impedance in order to illustrate the match between the well data and the inverted acoustic impedance. 78

A.13 Research methodology consists of two stages. First, the inversion stage which has two workflows which produce deterministic inversion based on CSSI and a stochastic inversion based on MCMC. Then, a second stage is implemented where we apply pressure analysis at the borehole using Eaton's Equation and Bowers's equation. Those analyses were extrapolated beyond the borehole using two methods: the linear regression method and the statistical cosimulation method which both transformed acoustic impedance into effective pressure. 79

A.14 Inversion quality control at well location. 80

A.15 Deterministic inversion final results using CSSI. 81

A.16 Mean of 10 simulated realizations. Simulation uses well data only. . . 82

A.17 A priori variogram for acoustic impedance. 83

A.18 Stochastic inversion final results using MCMC. 84

A.19 Cosimulation a priori statistical model: Vertical variogram based on calculated effective pressure at the wells, inline horizontal variogram based on the previously defined effective pressure from the linear regression and cross line horizontal variogram based based on the previously defined effective pressure from the linear regression. 85

A.20 Cosimulation a priori statistical model: Probability density function at the well location based on the calculated effective pressure. PDFs are segregated based on a previously defined lithology. 86

A.21 Effective pressure calculated using the cosimulation approach based on the mean of the 10 realization of the geostatistically inverted acoustic impedance volume. 87

A.22 Effective pressure section view through Wells-1,3 and 4 using (A) log aerial weighted interpolation, (B) linear regression tranformation (deterministic inversion), (C) linear regression transformation (geostatistical inversion) and (D) cosimulated transformation (geostatistical inversion). 88

A.23 Zoomed version of the effective pressure volume at Well-4 using (A) log aerial weighted interpolation, (B) linear regression tranformation (deterministic inversion), (C) linear regression transformation (geostatistical inversion) and (D) cosimulated transformation (geostatistical inversion). 89

A.24 Effective pressure at Well-1: Our wellbore calculated effective pressure based on our proposed method in black versus linear regression-based deterministic solution in red and linear regression-based stochastic solution in blue. Both regressions methods captured the general trend at the well location after applying the linear regression transformation from acoustic impedance to effective pressure. However, blue curve shows better correlation in comparison with the red curve. 90

A.25 The linear regression of effective pressure (psi) as a function of acoustic impedance ($kg/m^3 \times m/s$) color coded by density. Linear regression showed a 67% correlation between the two properties. 91

A.26 Effective pressure via crossing each approach value against the calculated wellbore effective pressure and against each other to determine their correlation and reduce uncertainty. Red dotted lines represent the correlation in each cross plot, black line represents the 45 degree line and data points are colored by well number: (A) the effective pressure based on the linear regression of the stochastic solution vs. the effective pressure based on the linear regression of the deterministic solution, (B) the effective pressure based on the statistically cosimulation of the stochastic solution vs. the effective pressure based on the linear regression of the stochastic solution, (C) the effective pressure based on the statistically cosimulation of the stochastic solution vs. the effective pressure based on the linear regression of the stochastic solution, (D) wellbore calculated effective pressure vs. the effective pressure based on the linear regression of the deterministic solution, (E) wellbore calculated effective pressure vs. the effective pressure based on the linear regression of the stochastic solution, (F) wellbore calculated effective pressure vs. the effective pressure based on the statistically cosimulation of the stochastic solution. 92

1. INTRODUCTION

Pore pressure prediction has become more important in assisting hydrocarbon exploration and production. Addressing pressure before commencing with the drilling stage has started to play a vital role in risk analysis, especially in deep offshore wells. Drilling problems attributed to geopressure such as formation collapse, stuck pipe, well kicks and blowouts account for 30% of the deep water drilling budget (Dutta, 2002). Hence, pore pressure prediction is an important topic to be investigated.

Pennebaker (1968) introduced a semi-standard geophysical approach involving the implementation of conventional seismic stacking velocity to predict abnormal pressure spatially. Stack velocities could be converted to an approximate form of interval velocity analysis using Dix's equation (Dix, 1955), which could be transformed into effective stress. Christensen and Wang (1985); Dvorkin et al. (1999); Sayers et al. (2002a, 2002b); Stone et al. (1983); Shapiro et al. (1985); Landrø (2001) followed similar approaches using different velocities to predict pressure spatially. However, most of those velocities were generated for imaging purposes but was not intended to be used for pore pressure analysis.

At the borehole, acceptable pressure prediction methods involve analyzing normal compaction trends (NCT) (Gutierrez et al., 2006), examining the ratio of compressional velocity to shear velocity (Vp/Vs) (Christensen and Wang, 1985; Dvorkin et al., 1999) or formulating empirical relations using wellbore log data in the GOM (Eaton, 1969; Brown and Korringa, 1975; Eberhart-Phillips et al., 1989; Bowers, 1995).

Seismic analysis has been a key element in pressure prediction, but acoustic impedance inversion has not been fully adapted. We hypothesize that if impedance decreases when pressure increases, then we can correlate impedance to pressure. In this research, we examined whether deterministic and stochastic inversion could be used to test our hypothesis. To answer this question, we applied the following steps: (1) evaluated NCTs at the borehole, (2) used NCTs to estimate pressure, (3) generated a deterministic and a stochastic inversion, and (4) correlated the transformed pressure with seismic inversion.

We tested our hypothesis on wells from the Gulf of Mexico (GOM), using constrained sparse spike inversion (deterministic) and Markov chain Monte Carlo inversion (stochastic). Results suggested that we could use seismic inversion to infer pressure. Therefore, this paper makes an explicit contribution in integrating post stack impedance inversion to predict and constrain qualitative pressure spatially, whereas most spatial pressure prediction methods emphasize seismic velocities or pre-stack inversion.

Below in our paper, we first reviewed the data set that served as the focus of our tests and applications, followed by details on the research methods and tools which were used to test our hypothesis. Then, we discussed the results and findings of applying our method on the field data. Finally, we conclude with a summary of the experimental methods and its contributions to the body of knowledge concerning pore pressure prediction and modeling.

2. DATASET

2.1 Seismic

Amberjack data sets utilized in this paper were provided compliments of CGG. The inversion flow was conducted on post-stack time-migrated 3D data from offshore in the Gulf of Mexico at the Mississippi Canyon Block 109. Seismic coverage is approximately 27 Km^2 in a rectangular shaped survey. The survey has a width of 4.2 Km and length of 6.5 Km; yielding 131 in-lines with 1 line increment and 345 cross lines with 4 lines increments (Figure 2.1).

There are $22,794$ traces which are samples at 4 ms. The data has a frequency bandwidth of 8-50 Hz, with a dominant frequency around 25 Hz. Seismic resolution at the reservoir level is approximated between 35-50 m, based on a frequency high cut filtered version of the measured compressional velocity log that ranged between 1,750 m/s to 2,500 m/s at the reservoir level.

2.2 Wellbore Logs

The sandstone formation was deposited on previously existing topography, interpreted as a graben, which was generated by deep faults. Logs include compressional sonic, shear sonic, density, gamma ray (GR), neutron porosity, resistivity and calculated saturation. Formations tops were provided with the dataset. The shear velocity is not a direct measure, as it seems to have been calculated based on compressional velocity. The interval has a high GR response, which could be attributed to the highly shale/sand lamination (Figures 2.2, 2.3). There are no caliper log data, so we can not judge the borehole washouts, which are quite common in shale.

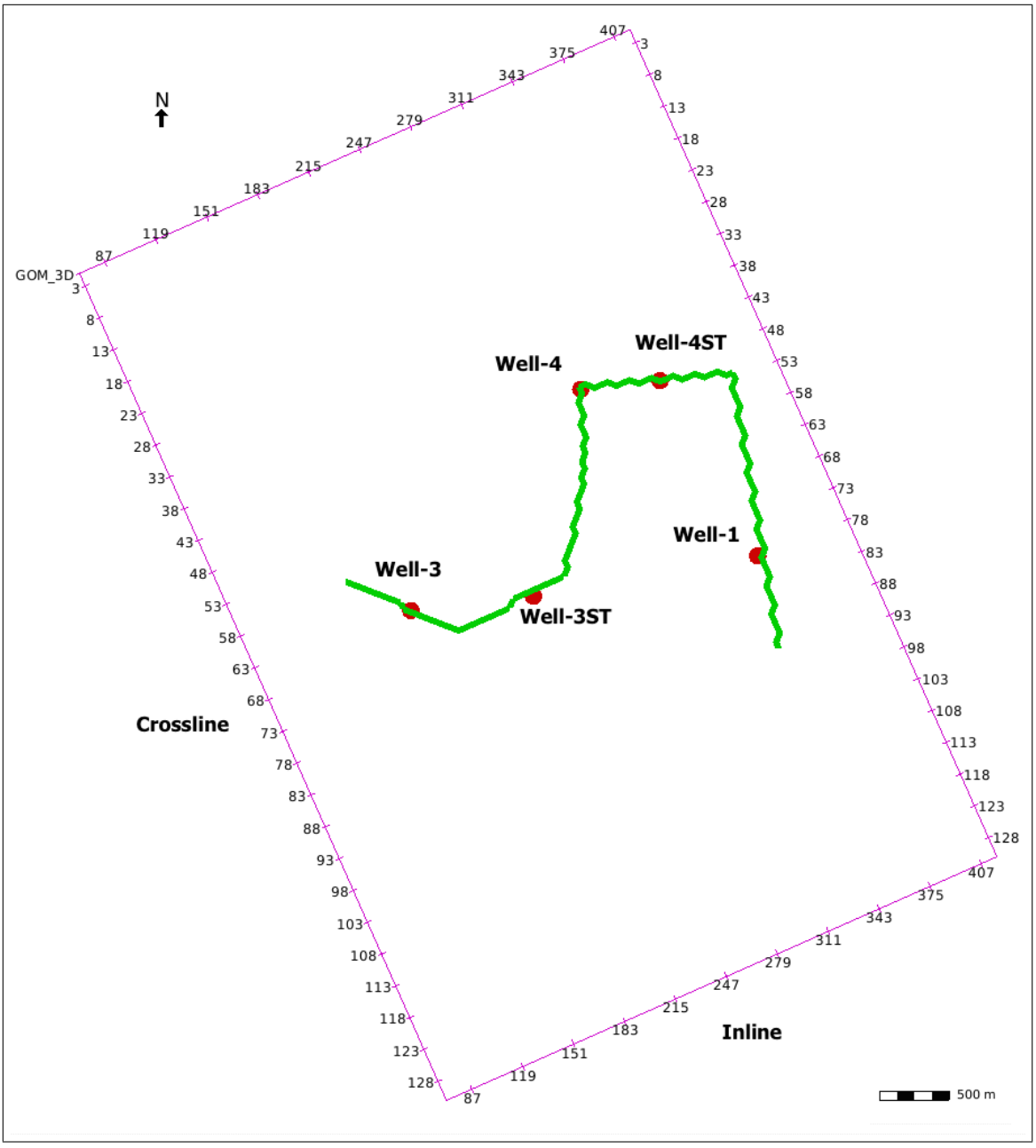

Figure 2.1: Well locations and seismic data coverage. The green line represent a zigzag line generated from the seismic data, which we used to present the study in this paper.

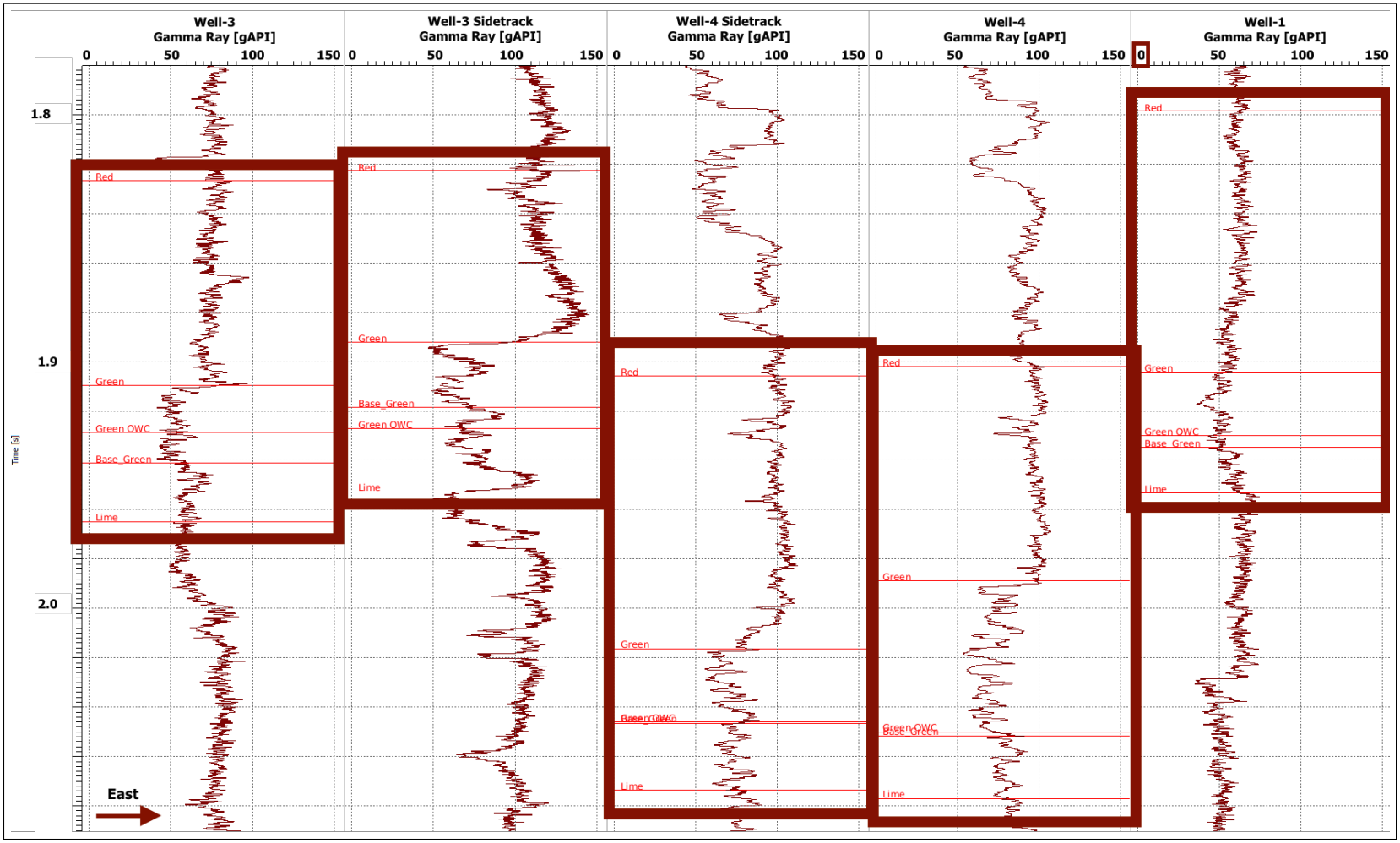

Figure 2.2: Log view plots showing gamma ray [gAPI] within the depth of interest in red rectangular at each well. We can observe three layers within our interval as the following: (1) low gamma ray (reservoir), (2) moderate gamma ray (shaley sand) and (3) moderate to high gamma ray (shale cap).

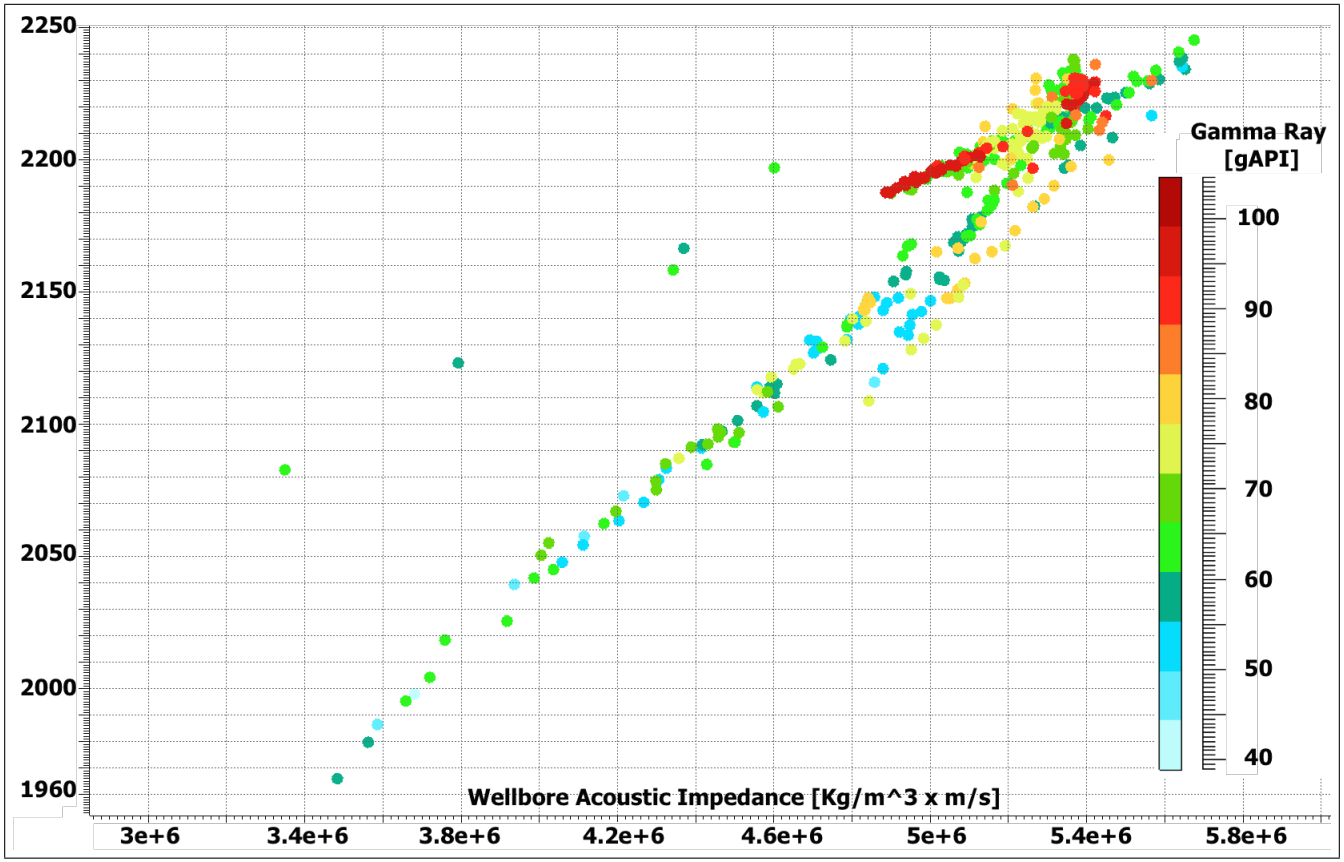

Figure 2.3: Cross plot showing acoustic impedance versus density colored by gamma ray in the depth of interest. Here, we can segregate the major three layers within our interval as the following: (1) low impedance, low gamma ray and slow velocity porous sand (reservoir), (2) medium impedance, moderate gamma ray and moderate to high velocity shaley sand, (3) high impedance, moderate to high gamma ray with high velocity shale cap

2.3 Geological Background

The Amberjack dataset is located in the Mississippi Canyon (Block 109). The reservoir is a middle Pliocene sand with an average thickness around 70 ft. The reservoir interval consists mainly of sand and shale layers. Mayall et al. (1992) showed that Well-1 has three major sand facies based on core analysis: a structureless sand, a parallel-laminated interbedded sand, and a thinly interbedded sand. Goodwin and Prior (1989) described the sequence stratigraphy of the Mississippi Canyon and pointed out that the reservoirs distribution are controlled by channels in a deltaic dominated environment.

We could conclude that the reservoir is heterogenous, as it consist of different sand strata. The upper delta accommodation space could also host upper sand along with slump-dominated shaley sand and mouth bar sands. In fact, the heterogeneity in this particular field and within the upper delta sand reservoir acts as a barrier in reservoir connectivity, or in some cases, as a buffer (Latimer et al., 1999). The basin tectonics of the area are influenced by immature salt stock that caused deep faults (Pilcher et al., 2009). We observed five seismic facies: (1) parallel, (2) subparallel, (3) topset, (4) chaotic and (5) reflection free (see appendix A for more details).

The main trapping mechanism is considered to be a structural trap. However, the hydrocarbons within the reservoir are trapped between alternating of sand and shale laterally. There are 5 wells with wireline logs; three are vertical wells (Wells-1,3 and 4) and the other two were drilled as side-tracks (Well 3-ST and 4-ST). All wells seemed to target a sand layer that has bright RMS amplitude (Figures 2.4, 2.5).

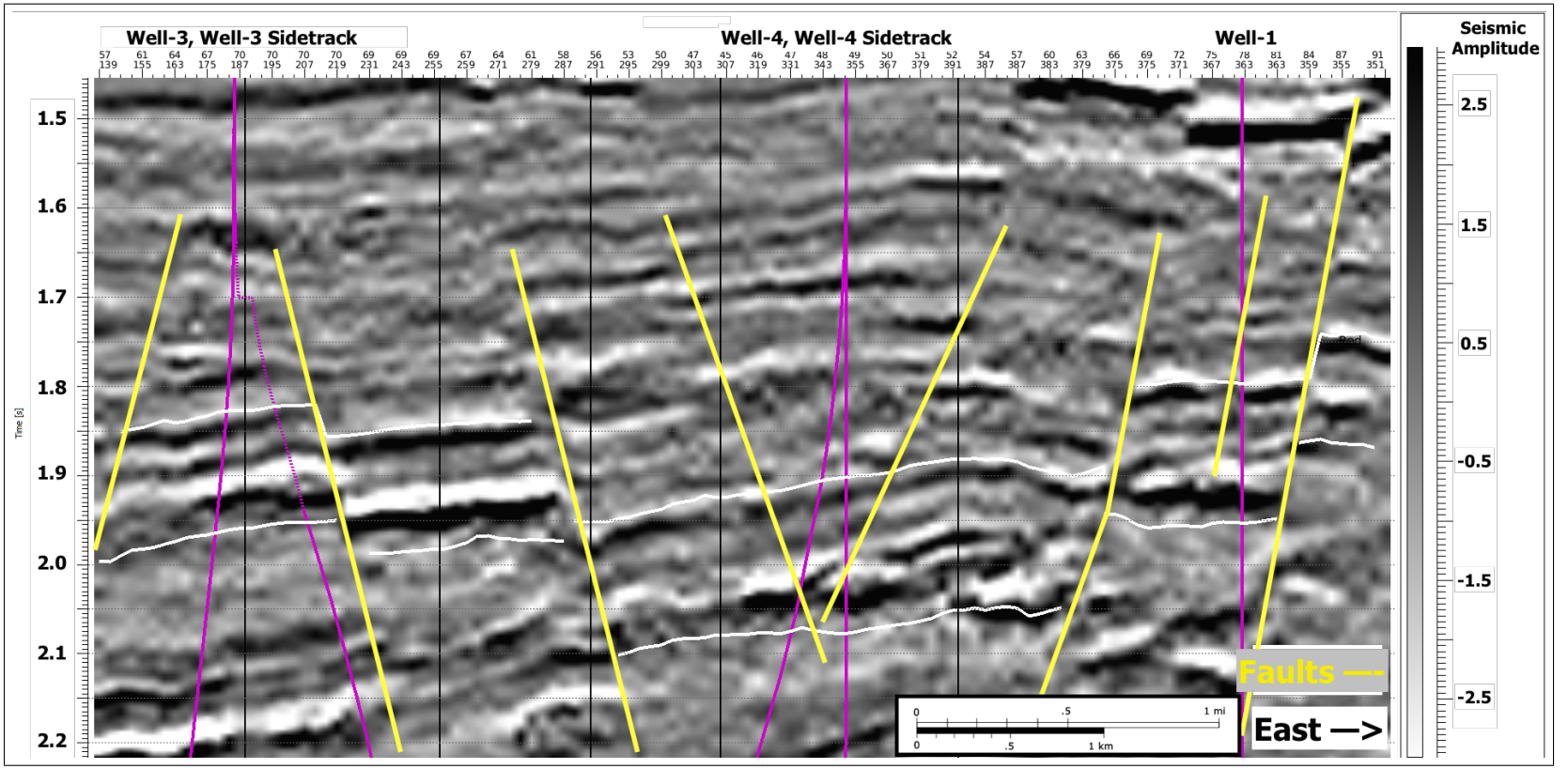

Figure 2.4: Easting 2D zigzag seismic line representation going through Wells-1,3 and 4. Two horizons where picked above and below providing a time window of around 150 ms. The observed lateral displacement is believed to be caused by deep normal faults which is interpreted as a graben.

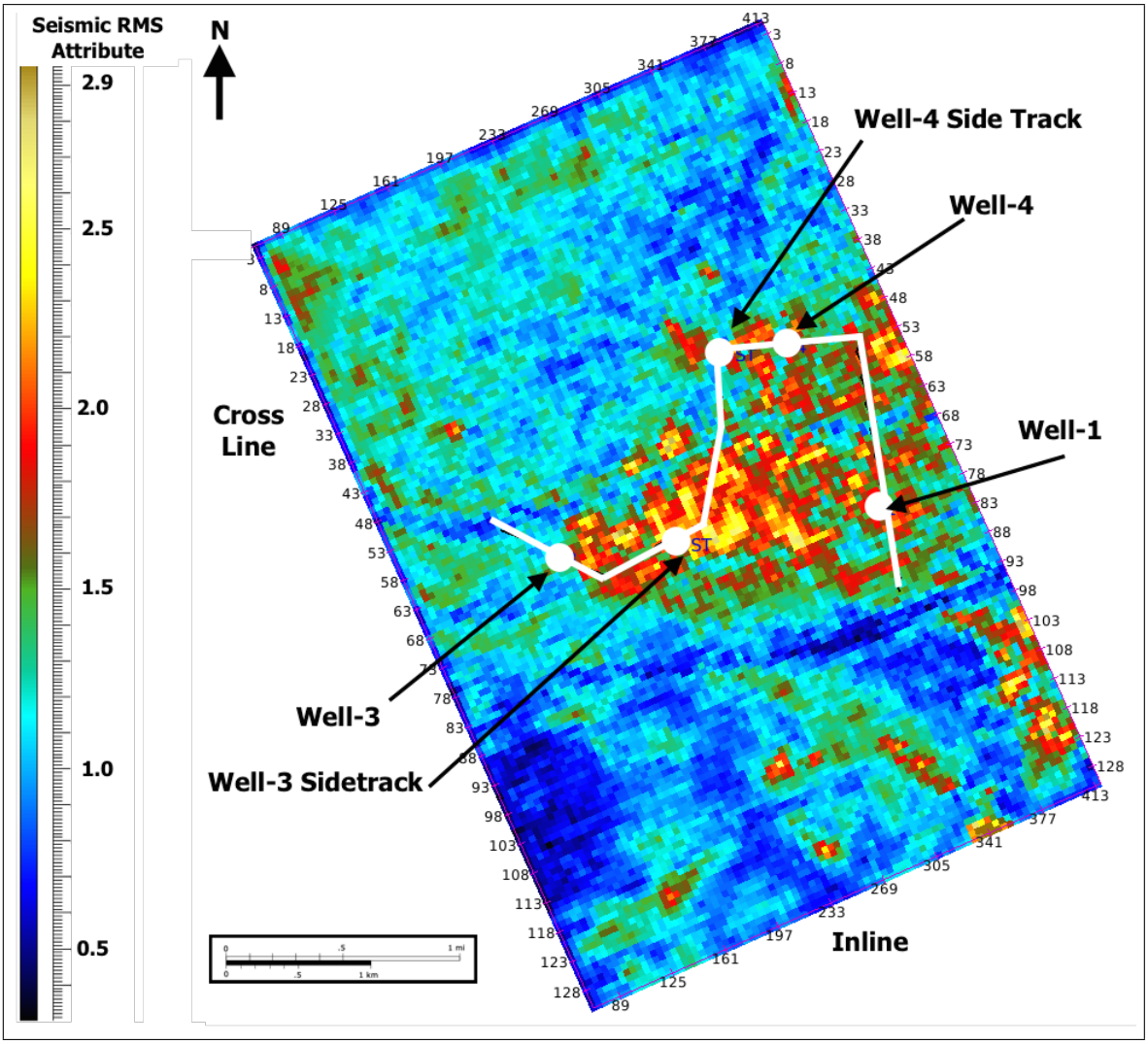

Figure 2.5: Seismic amplitude root mean square attribute for the defined 150 ms interval. The wells appeare to target the high RMS amplitude, which could represent the porous hydrocarbon-filled sand reservoir. A zigzag line was generated between the wells to illustrate results.

3. RESEARCH METHODS

We investigated utilizing borehole acoustic logs to predict pore pressure at the borehole. First, we used common approaches to predict pore pressure at the borehole using acoustic logs. Two specific equations relating velocity to effective pressure were used: Eaton's equation (Eaton, 1969) and Bowers's equation (Bowers, 1995). We interpreted the NCT and investigated how it could help identify overpressure zones using Eaton's equation. Moreover, we used Bowers's empirical equation and compared its output with Eaton's, to reduce uncertainty. Finally, we extrapolated the borehole-based calculations beyond the borehole, using deterministic and stochastic seismic inversion. (Figure 3.1) illustrates our research methodology.

In our research methodology, we shed the light on the utilization of post-stack seismic inversion to constrain pore pressure prediction, as such techniques provide a higher resolution due to broader frequency contribution (compared to seismic interval velocity). In the absence of acoustic impedance to effective pressure reliable relation, we simplified the problem by assuming a negligible density effect. This assumption is valid in the GOM and similar areas where shale is homogeneous laterally, due to its geological settings (Smith, 2002).

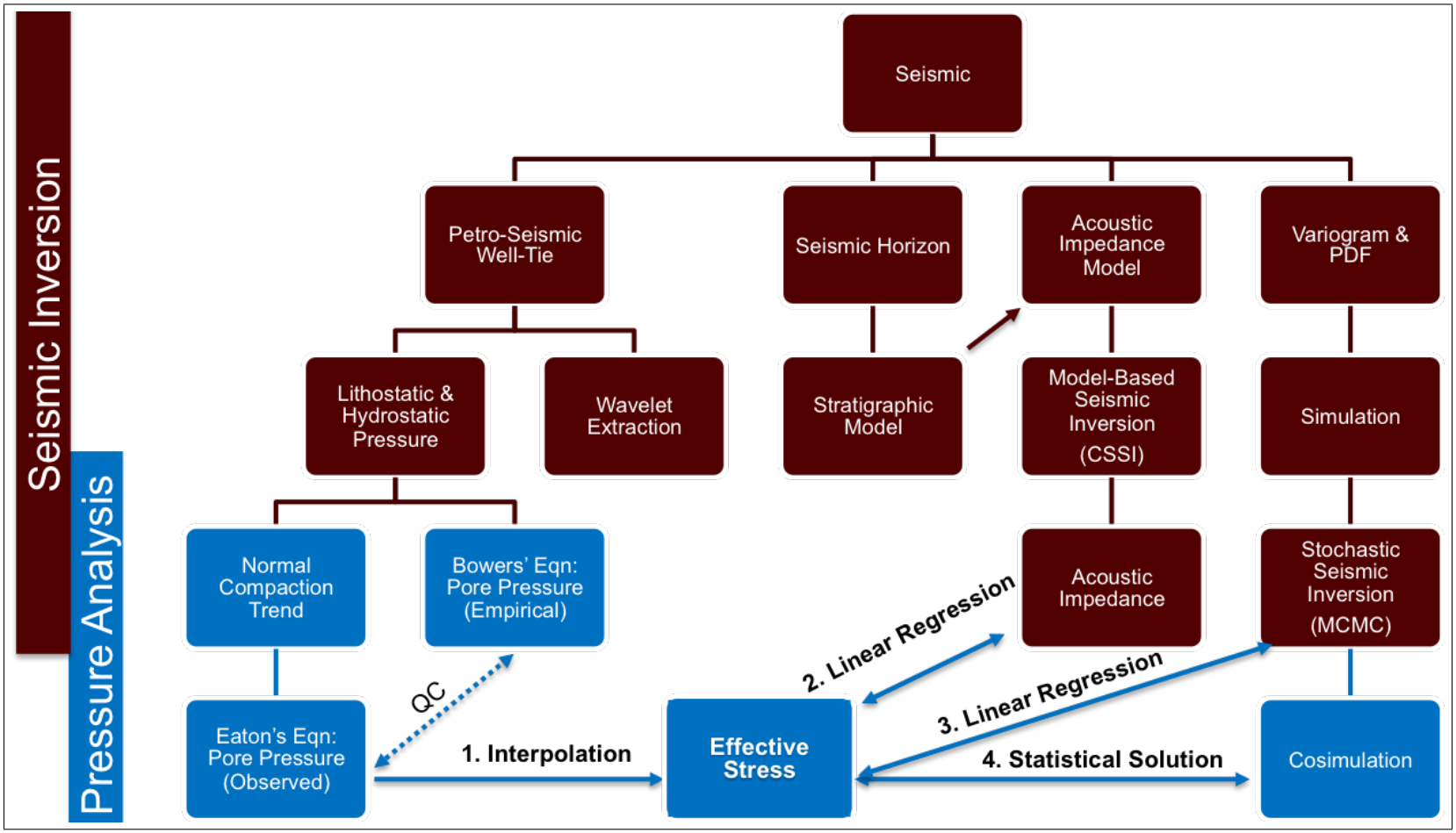

Figure 3.1: Research methodology consists of two stages. The first is the inversion stage which has two workflows which produce deterministic inversion based on CSSI and a stochastic inversion based on MCMC. Then, a second stage is implemented where we apply pressure analysis at the borehole first using Eaton's Equation and Bowers's equation. Those analyses were extrapolated beyond the borehole using two methods: the linear regression method and the statistical cosimulation method which were both transform acoustic impedance into effective pressure.

3.1 Borehole Pressure Analysis

3.1.1 Terzaghi's Principle

We used Terzaghi's principle to predict pore pressure (Terzaghi et al., 1996). Hubbert and Rubey (1959) employed Terzaghi's principle in subsurface pressure analysis. They showed that the total pressure exerted on a rock being supported by the rock matrix and the pore fluid can be expressed as:

$$\sigma_{ij} = \sigma'_{ij} + \alpha P_P \delta_{ij} \tag{3.1}$$

where: σ is total stress tensor, σ' is the effective stress tensor, δ_{ij} is the Kronecker delta, and P_P is fluid pore pressure. Since $\alpha = 1$ for soft sediments and $i = j$, then:

$$\sigma = \sigma' + P_P \tag{3.2}$$

While this equation has been historically used for soil mechanics, it also holds true within a geological framework. However, the vocabulary could be misleading as scientists have used different words for the same parameters. Here, the total pressure would be the overburden pressure (also known as lithostatic pressure and geostatic pressure) in geological terms. Overburden pressure is defined as the pressure applied by the overburden weight on a specific rock unit. Thus, it does include the rock matrix and the pore fluid and solely depends on the rock density (ρ) and the total depth (formation depth):

$$\sigma_{overburden} = \int_{surface}^{formation\ depth} \rho(z)\ g\ dz \tag{3.3}$$

Intuitively, this implies that overburden pressure is directly proportional to density. Since density increases with depth, so does overburden pressure. Overburden pressure estimation is not challenging, when compared to pore pressure, as it only requires depth and density. Figure 3.2 illustrates a simple representation of the three different pressure types described above. Ironically, literature interchangeably uses stress for pressure and vice versa, but the former is a tensor and the latter is isotropic in fluids. Mixing and switching terms is quite common in the literature (Bruce and Bowers, 2002).

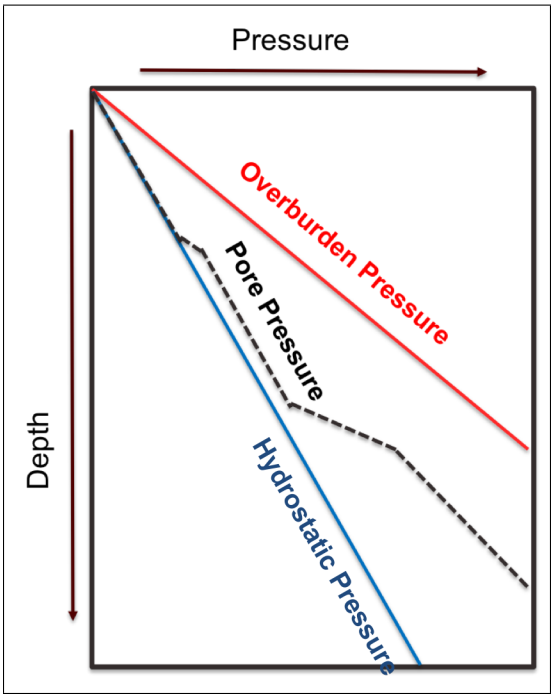

Figure 3.2: Pore pressure, hydrostatic pressure and lithostatic pressure versus depth.

On the other hand, effective pressure can not be measured directly as easily, as it represents the previous parameter within Equation 3.2. Effective pressure represents the pressure applied to the rock matrix. In theory, it can be calculated if we know

the exact porosity and fluid type and subtract that from the wet rock to estimate the dry rock effective pressure after applying an equivalent value of the overburden pressure on a core plug in the laboratory (Vanorio et al., 2010). Pore pressure, the third parameter in Equation 3.2, is defined as the pressure exerted by the pore fluid and it is also known as formation pressure and fluid pressure.

3.1.2 Direct Pressure Measurement Methods

Pressure can be directly measured by several engineering methods after drilling the formation. Methods like repeat formation test (RFT), modular formation test (MDT), formation multi-tester (FMT), formation integrity test (FIT) and drill stem test (DST) can provide lateral direct measurement of pore pressure at the wellbore, but they lack spatial resolution, especially in formations with low continuous pressure. This is not to mention their high cost and limitation of providing the measurement in the post-drilling stage only, which does not help in designing the drilling mud or the casing system.

This paper neither addresses history matching of pressure nor does it attempt to relate the direct pressure measurement to the predicted pressure measurement, due to the lack of data. Since the pressure values cannot be verified without direct pressure measurement, we verified our findings with a reconstructed pressure gradient curve based on Morris et al. (2015).

3.1.3 Indirect Pressure Prediction Methods

Indirect methods include seismic velocities, well-log analysis and drilling parameters. Seismic velocities have been considered a standard indirect method to predict pore pressure (Sayers et al., 2002b). Seismic velocities are initially generated to provide a maximum coherent stack by applying normal moveout correction in the pre-stack domain to flatten events so they stack up to increase the signal to noise

ratio (S/N). One can use Dix's equation to convert velocity (Dutta, 2002). However, Dix's equation lacks uniqueness as a slight change in the root-mean square velocity lead to infinite models of interval velocity. Moreover, seismic velocities are not rock velocities (Alchalabi, 1997). If we use such velocities, we could end with unacceptable perturbation in velocity-to-pressure transformation.

Most seismic based methods transform a seismic based velocity into porosity under several assumptions. Then, they try to relate porosity to effective pressure, as overpressure zones tend to have high porosity and hence lower seismic velocities. The effective pressure is dependent upon the grain contacts; hence, it affects the propagation path which leads to its effect on velocity (Domenico, 1984).

On the other hand, petrophysical techniques can be applied only after drilling the well, while seismic methods can be useful before and after the drilling stage; not to mention its sparse coverage compared to petrophysical methods.

Drilling parameters analysis can only be applied during or after drilling, as we acquire the rate of penetration, torque, equivalent mud weight, mud flow and temperature. However, current drilling methods are masking the effect of the rate of penetration (ROP) and may be misleading. Mud temperature may help in determining the temperature of the formation which correlates to pressure in some basins. However, such a method lacks uniqueness and, similar to log-based ones, it is still restricted to the borehole (Stunes, 2012).

Unfortunately, the lack of direct pressure measurements within the dataset was another challenge in this paper, which simulates exploration scenarios. Notwithstanding, we addressed this problem by comparing our findings for the pressure against the published results of Morris et al. (2015), who focused on the northern section of the GOM, which includes our area of interest (AOI). Morris et al. (2015) published a geostatistical estimation for pore pressure in the GOM where they ex-

amined 12976 initial hydrocarbon reservoir pressure gradient values and 43,279 mud weight values. They mapped pressure gradient every $1,000$ ft from $2,500$ ft to $17,500$ ft.

Seismic data has a well established relationship between seismic properties and fluid properties (Batzle and Wang, 1992). Seismic data is also superior in spatial coverage and acquisition speed, all of which motivated me to to pursue this subject.

3.1.4 Normal Compaction Trend Analysis

There are several reasons behind abnormal pressure; this paper intends to focus on undercompaction. Undercompaction occurs when the rates of deposition and burial are higher compared to relative vertical permeability of the sediments. This causes fluids to be trapped within pores. The inability of fluids to escape (which would maintain the hydrostatic pressure) causes an increase in pore pressure (Bruce and Bowers, 2002). Compaction disequilibrium is considered to be the major reason behind overpressure build-up in the GOM (Dickinson, 1953), (Hubbert and Rubey, 1959). Pressure is a fluid property caused by specific geological conditions. Therefore, we must honor the geological settings in our analysis. A geological understanding of the depositional history could clearly define to the depositional trend. NCT analysis has been proven capable of identifying undercompaction in the GOM (Magara, 1978).

We classified undercompaction zones by identifying them through the departure from the NCT. Separate sets of NCT analysis would be carried out based on borehole compressional velocity at each well (Figure 3.3). Eaton's method allowed us to translate NCTs to effective pressures. Then, using Terzaghi's principle, Equation 3.2, we derived pore pressure from NCT-based effective pressure and from the calculated overburden pressure as in Equation 3.3.

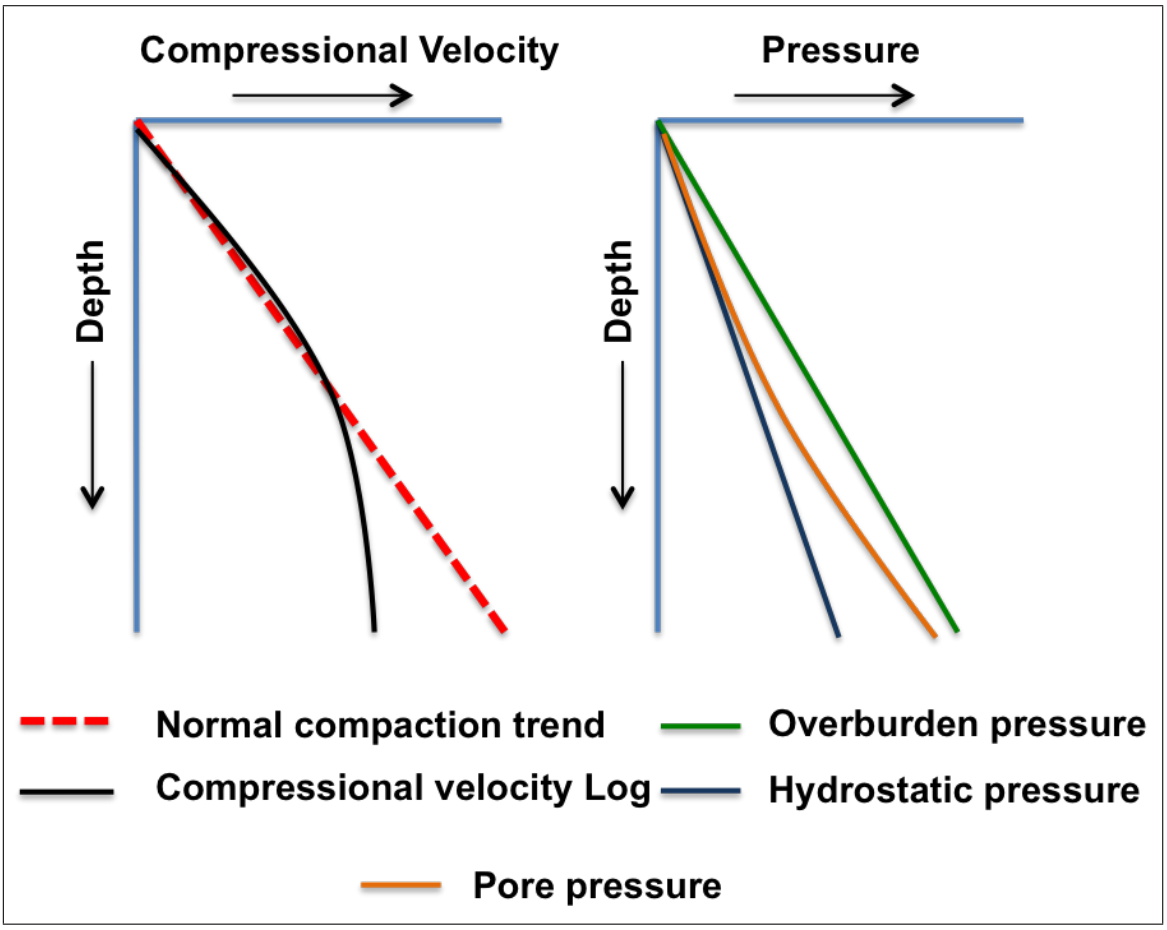

Figure 3.3: Schematic diagram showing the normal compaction trend analysis on compressional velocity borehole log and its relation to pore pressure.

3.1.5 Bowers's Equation

Bowers's equation is a empirical attempt to present effective pressure as function of compressional velocity (Bowers, 1995). Bowers's equation is based on statistical analysis of the GOM only but it was applied in different basins. Bowers's equation states that:

$$P_{LS} - P_P = \left(\frac{V_p - 5000}{a}\right)^{\frac{1}{b}} \tag{3.4}$$

where (P_{LS}) is the lithostatic pressure, (P_P) is the pore pressure, (V_P) is the compressional velocity, and ($a = 9.18448$) and ($b = 0.764984$) are calibration coefficients for the GOM only (Bowers, 1995). Niranjan et al. (2014) reported a modified Bowers's relation. Their modified equation involves multiplying both sides of Bowers's equation by density as below:

$$(P_{LS} - P_P) \times \rho = \left(\frac{V_p \times \rho^b - 5000 * \rho^b}{a * \rho^b}\right)^{\frac{1}{b}} \tag{3.5}$$

However, lithostatic pressure must also be also redefined to include formation density. Hence, the lithostatic acoustic impedance will become:

$$AI_{LS} = \sigma_{overburden} = g \int_{surface}^{formation\ \ depth} \rho(z) \times V_p(z) \times Depth \tag{3.6}$$

3.1.6 Eaton's Equation

Eaton (1969) introduced an an empirical equation based on the Gulf of Mexico basin. He formulated four equations to prediction pressure using resistivity, sonic logs and drilling exponent (a mud logging equation that accounts several drilling parameters such as mud weight, weight on bit, etc.). Eaton's equation accounts only for undercompaction as the main reason for overpressure layers, and NCT analy-

sis has been proven capable of identifying undercompaction (Magara, 1978). The departure from of the normal compaction trend infers undercompaction; hence, an overpressure. The pressure could be quantified as below:

$$P_{LS} - P_P = (P_{LS} - P_{HS}) \times \left(\frac{V_p}{V_{NCT}}\right)^3 \tag{3.7}$$

where (P_{LS}) is the lithostatic pressure, (P_P) is the pore pressure,(P_{HS}) is the hydrostatic pressure, (V_P) is the compressional velocity and (V_{NCT}) is the normal compaction trend velocity. Equations (3.4 and 3.7) present the effective pressure as a function of acoustic impedance indirectly.

3.2 Seismic Inversion

Our research methodology integrates and utilizes various methods to tackle the pore pressure estimation at the borehole. Our flow combines the seismic amplitude, post-stack deterministic and stochastic inversion, open-hole petrophysical logs, interpreted horizons, and well tops to establish correlation/transformation between acoustic impedance and pore pressure. Then, pressure is extrapolated spatially using seismic inversion. We are planning to apply an integrative solution because most pressure equations such as Eaton's (Eaton, 1969) or Bowers's (Bowers, 1995) are based on empirical and/or statistical relations, with no rock physics to support the findings (Dutta and Khazanehdari, 2006).

Moreover, locally defined velocity-pressure equations are not unique as such transformations are heavily dependent on several factors such as rock matrix, porosity, pore distribution, fluid type and burial rate. Hence, to reduce uncertainty, we calibrated Eaton's and Bowers's equations against each other to confirm pressure results at each well (see appendix A for more details). Such calibration is also considered acceptable as we seek to establish a qualitative pressure attribute and a pressure

gradient, which mainly what hydrocarbon geoscientists and drilling engineers are concerned about.

The final pressure solutions from each inversion method could be visually and quantitatively correlated to better constrain the pressure predictions. An advantage of combining deterministic inversion and geostatistical inversion is that the solution space is constrained as we use the former solution as an input to the latter. For the deterministic approach, we used the accepted Constrain Sparse Spike seismic inversion (CSSI). For the latter we used the Markov chain Monte Carlo (MCMC) inversion as our statistical inversion method. This study does not intend to compare pros and cons of using either method; rather, we are using both tools to narrowing the solution space (feasible sets) for the pore pressure models when we compare final pressure results against each other quantitatively. CSSI results and findings were used to establish and parameterize the initial geostatistical model which reduced feasible sets.

Both methods were implemented using the CGG/Fugro-Jason software package. The goal is to run both algorithms on the same dataset to achieve a good acoustic impedance inversion that could be used for pressure modeling. Overall, CSSI results are faster to generate and require less processing power and less human hours (around 4 times) compared to MCMC. However, the results of MCMC are usually superior to CSSI when it comes down to the vertical resolution as MCMC shows thin layers that are not detectable by CSSI (Doyen, 1988). On the other hand, CSSI provides one single solution (deterministic), while MCMC could, theoretically, provide an infinite number of realizations that all could be possibly true (Dubrule et al., 1998). CSSI output is usually the inverted acoustic impedance with trend-merged frequencies.

In our MCMC inversion, we employed cosimulation (Francis, 2006) to transform acoustic impedance into further engineer properties such as effective pressure (Soares,

2001). MCMC is a quite sensitive method, especially compared to the initial geostatistical models, as it does not require any prior model. In contrast, CSSI is mainly based on matching a prior model with the seismic data (Haas and Dubrule, 1994). Consequently, the posterior residual of each inversion method was different.

Quality-Control of the inversion process uses: (1) correlation at the well location between the seismically inverted acoustic impedance and the wellbore measured acoustic impedance, (2) extraction of seismic attributes (RMS, mean, maximum, minimum) from the mismatch weighting factor and (3) decomposing the inverted results through frequency spectral decomposition to ensure that the results are physically meaningful. Within geostatistical methods, those are more sensitive to noise compared to CSSI (Bosch et al., 2010). On the other hand, CSSI suffers when using inaccurate well tie and/or inaccurate wavelet data. Uncertainty could be addressed when by using geostatistical inversion through cumulative distribution function which ranks realization based on a user specified criterion while CSSI uncertainty can only be treated only with residual analysis which could be misleading if inversion parameters are not designed carefully (Bosch et al., 2010).

Stack data is the most common form of seismic data. Since we inverted the provided stacked seismic data, our output will be exclusively acoustic impedance. In fact, post stack inversion techniques are still the most common applied inversion algorithms in major companies due to data availability and processing time. Pre-stack data require careful processing and angle-transformation, which should all be parameterized based on previous work and/or rock physics modeling. Inversion algorithms should be applied within a stratigraphic mesh based the geological settings. The mesh boundaries honor the geological deposition settings (truncated, proportional, onlap and download) (Figure 3.4). The mesh could also serve to build a proper low frequency model.

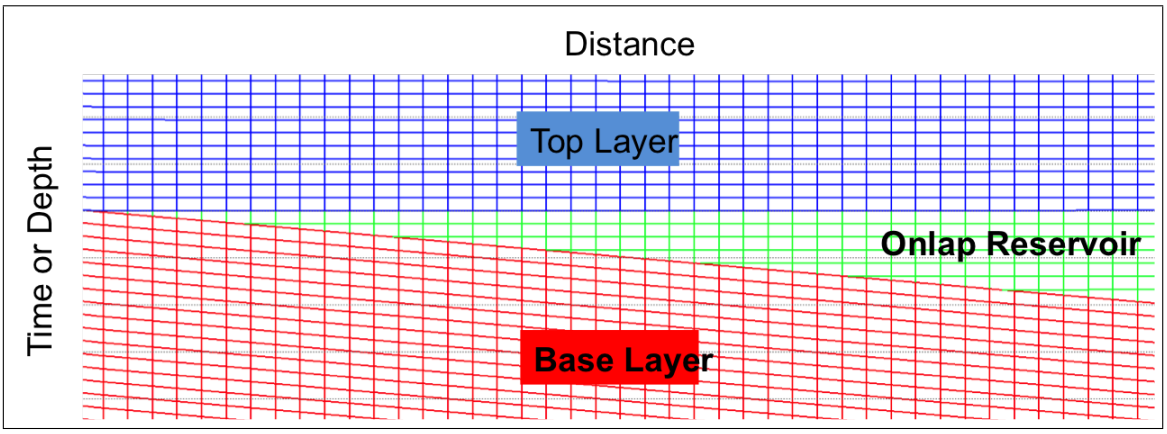

Figure 3.4: A schematic three layers mesh model based on strata interpretation on the wedge model. Those layers are interpolated based on the mechanism of the deposition. Hence, each individual cell would be filled with the inversion process while taking into account the geological observations of the subsurface. This example illustrates a reservoir that onlap on the base layer.

4. RESULTS

We interpreted three key horizons above and below our reservoir and generated a time grid for them. Then, we constructed a mesh grid based on our interpretation of the geological setting, which showed a parallel pattern that truncated against the faults (Figure 4.1). The mesh boundaries honored the geological deposition settings (truncated, proportional, onlap and download). The mesh serves as the container where the low frequency was populated using a high-cut frequency filter based on an aerial interpolation of the acoustic impedance log (Figure 4.2). Before proceeding with inversion, we tied our wells (depth to time) and extracted wavelets for all the wells.

Most inversion algorithms lack the low frequencies (Bosch et al., 2010). Therefore, we compensated for low frequencies with a user-interpreted mesh grid (Samson et al., 1996). The mesh grid served as framework to populate our low frequency model via a low-pass frequency filter based on well log data. The mesh boundaries were defined based on a key horizon in the study area and the mesh and its interpolation process was defined based on the geological interpretation of the area (Figure 4.1). Each grid geometrical shape was setup to represent geological patterns in deposition as (1) proportional, (2) eroded, (3) onlap, (4) downlap or (5) truncated layers. Employing this approach, we built a low frequency model using a combination of well log data input and seismic interpretation guidance to generate a more accurate, low-frequency trend within the model (Figure 4.2).

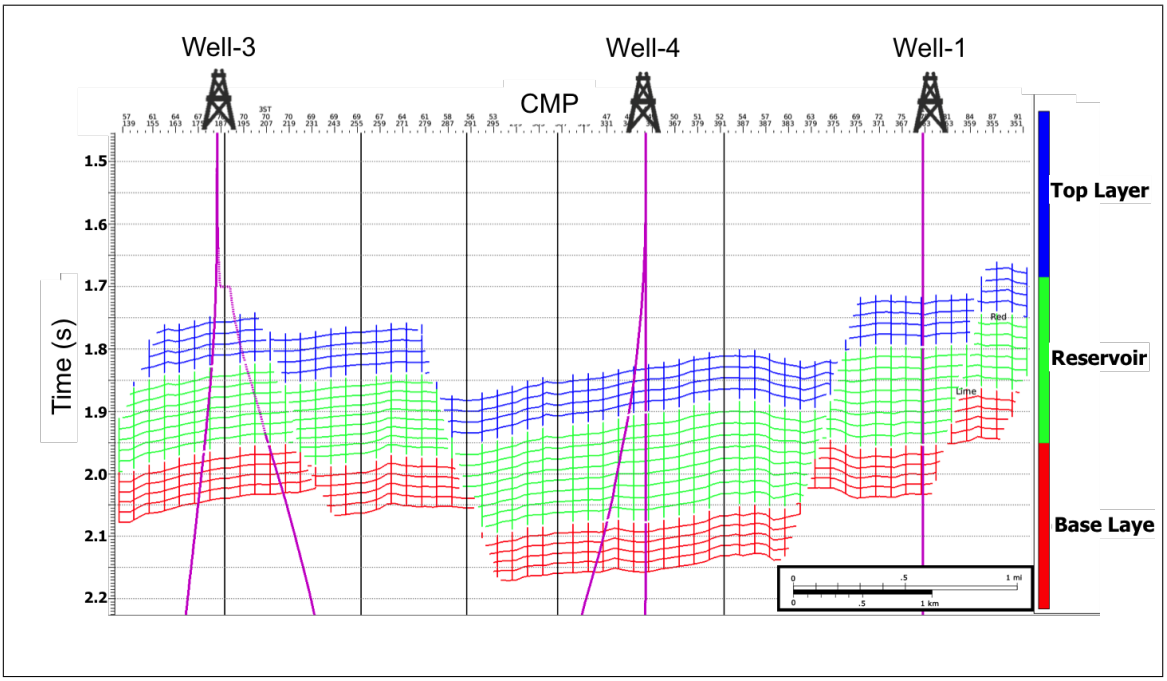

Figure 4.1: Three Layers Mesh model based on seismic strata interpretation. Those layers are interpolated based on the mechanism of the deposition. Hence, each individual cell would be filled with the inversion process while taking into account the geological observations of the subsurface.

4.1 Acoustic Impedance Inversion on the field data

4.1.1 Post-Stack Deterministic Inversion

We used a model-based constrained sparse spike algorithm (CSSI) for the deterministic solution. Inversion is simply the transformation of seismic reflection data to an earth model at each common mid-points (CMP). Common inversion algorithms would be iterating to minimize an objective function in time domain to provide a consistent model with the observed surface seismic data. When trend merging different data, the inversion process input has a broader frequency contribution. Therefore, the output of the inversion process must have a higher resolution in time domain compared to the input seismic data (Figure 4.3). Hence, utilizing inversion results

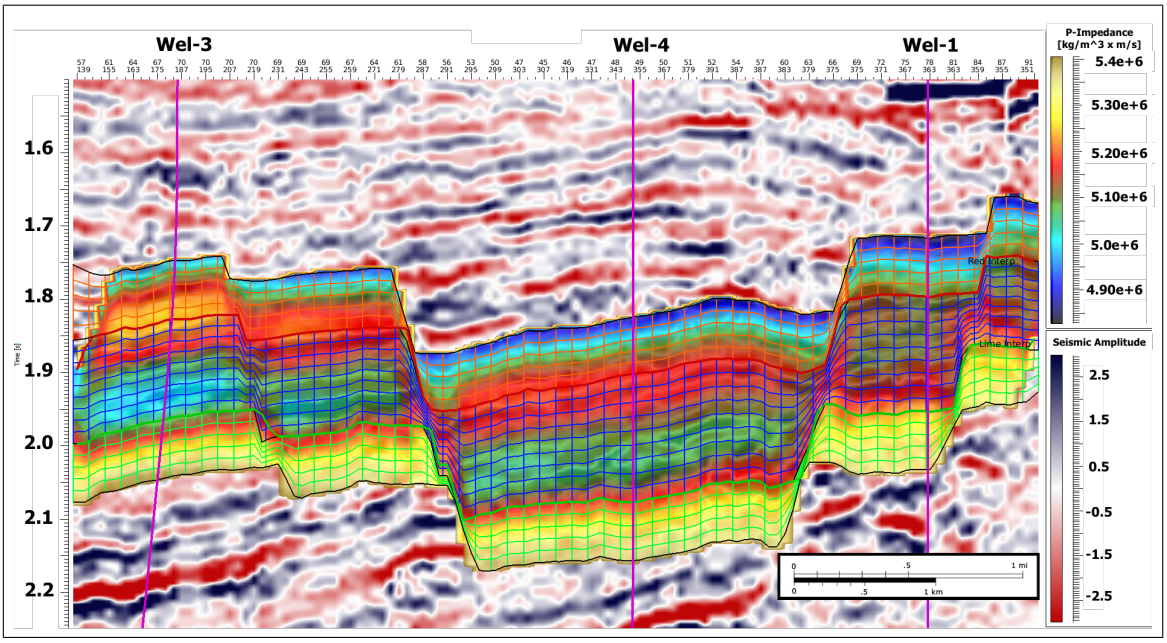

Figure 4.2: Low frequency model overlaid on top of the previously defined mesh model. The low frequency is derived from the control points (vertical wells) in this case. The mesh boundary and cell shape define the extent of the filling of each cell. Hence, honor the geological observation of the subsurface

in pressure analysis should yield a higher resolution pressure model.

CSSI is a trace-based algorithm that can incorporates time-dependent bound constraints. Those constraints are done on acoustic impedance based on the compaction trend from the wellbore data. Users can define a range to allow the algorithm to perturb from that compaction trend to define the bound/constrain window to define the acoustic impedance low frequency model (0-5 Hz) (Torres-Verdin et al., 1999). Hence, the low frequency model represents the acoustic impedance compaction trend. In our research methodology, we simply generated the low frequency model from an aerial weighted interpolated model based on log-based acoustic impedance in a stratigraphic mesh domain in the first iteration of CSSI (see appendix A for more details). Then, we applied a high frequency cut on the first attempted inverted acoustic inver-

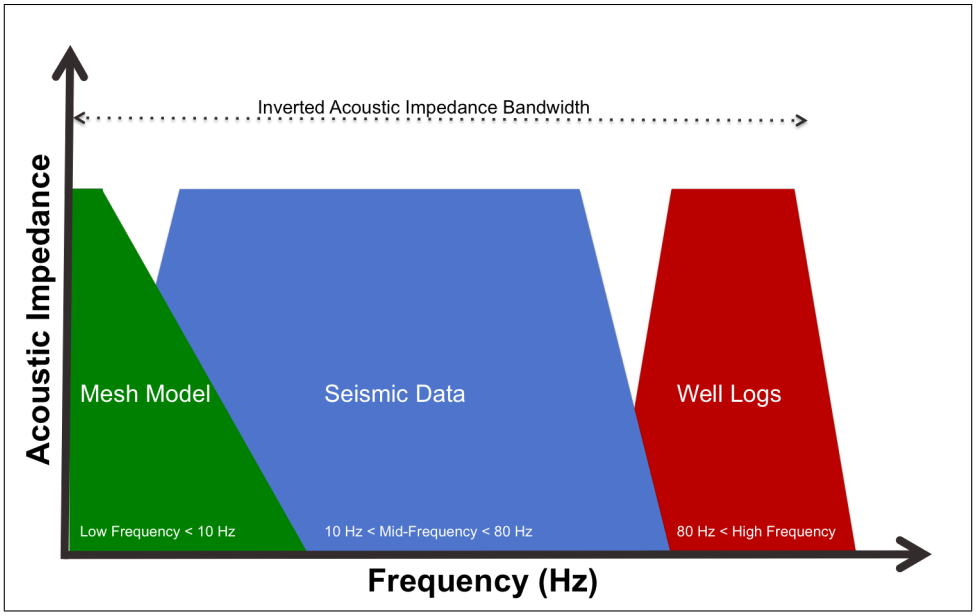

Figure 4.3: Deterministic inversion in frequency domain. Merging the three different data yield a wider frequency contribution in frequency domain which would translate into a shaper wiggles in time domain, which increases the resolution of the trend merged inverted result.

sion to refine the low frequency model for the second inversion iteration to fine-tune our final inverted acoustic impedance.

The deterministic inversion process relies heavily on an initial model; to build the initial model we have to address the low frequency contribution as it is below the seismic bandwidth. Low frequency (0 - 10 Hz) defines the general trend. We solely used a trend model based on the wellbore log data; hence, the low frequency model is constrained only by our wellbore data. Therefore, a prober calibration between seismic and wellbore data is crucial.

First of all, wells have to be tied to the seismic data. Wells are sampled in depth while seismic is sampled in time with different frequencies. We established a well-tie using the provided acoustic logs. Then, we extracted a hybrid wavelet which is favorable for quantitative seismic analysis (Alfaraj et al., 2010). Since we

are planning to apply a rock physics model, we will be able to systematically vary the initial model before running the inversion which will constrain the final model. This was achieved through running two inversion iteration where the first attempt at inverted acoustic impedance fed into the final low frequency model.

The CSSI algorithm works by iterating to find the minimum solution through constraining it via a user defined objective function as follows:

$$F_{obj} = \Sigma(R_i)^p + \lambda^q \Sigma(D_i - S_i)^q \tag{4.1}$$

where (R_i) is the reflection coefficient, (d_i) is the recorded seismic acoustic trace, (S_i) is the already derived synthetic trace, p and q are empirically determined exponents and (λ) is the mismatch weighting factor which depends on the data quality.

While CSSI could have other outputs, we focused our study on the main two outputs: the trend merged acoustic impedance volume and the inversion residual. The trend merged acoustic impedance is the final product of the inversion after trend merging the results with the low frequency model and the high frequency model from the wellbore log data. The residual is the unmatched seismic signal after the inversion process which could be attributed to many factors such as noise, inaccurate model, acquisition footprint or processing artifact. Hence, the higher the residual, the higher the mismatch, and vice versa. Nevertheless, due to the non-uniqueness of the seismic response, low residual does not indicate success in recovering the true acoustic impedance.

Post-stack inversion results are expected to increase the resolution of the resolvable layer. It also reduced the tuning effect and allowed us to interpret facies based on geological background where we attenuated the wavelet effect. We broadened the frequency contribution using the low frequency trend and the high frequency wellbore

logs, which increased the resolution of our inverted acoustic impedance. Our results were quality controlled using correlation at the well location and residual attribute analysis; we achieved 80% correlation at the wells at the reservoir interval.

The first attempt at inversion was generated without forcing the algorithm to honor the well location (see Appendix A for more details). Therefore, we can use the wells as control points to quantify accuracy of the deterministic inversion (Figure 4.4). This was achieved via cross-plotting the actual acoustic impedance vs. the inverted results (see Appendix A for more details). We also extracted the RMS attribute from the residual of the inversion process to assure that we did not leave any amplitude that could be inherited from the geological features.

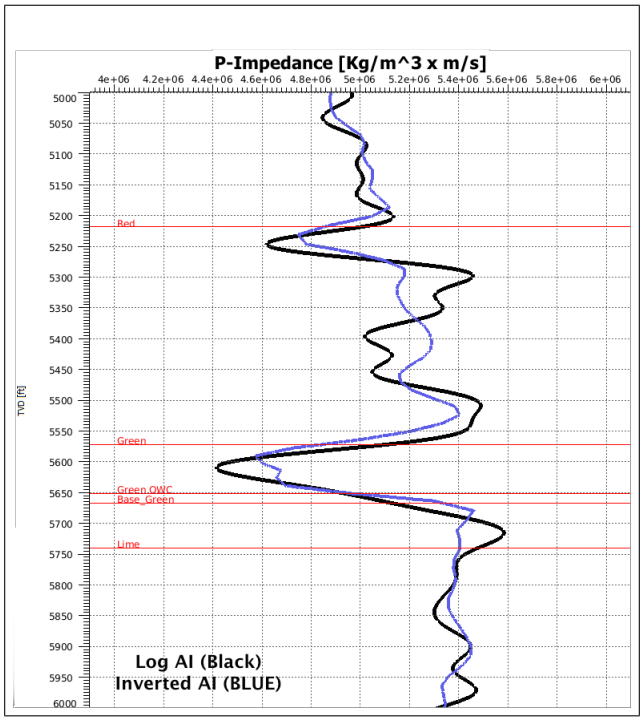

Figure 4.4: Deterministic result at Well-1: Wellbore log measured acoustic impedance in black and inverted impedance using CSSI in blue.

4.1.2 Post-Stack Geostatistical Inversion

Geostatistical methods, in general, aim to estimate a geophysical property such as acoustic impedance at 2D/3D grid points where the property is unknown. Geostatistics takes into account known input data using statistical methods to quantify reservoir spatial variability (Pyrcz and Deutsch, 2014). Integrating seismic data with the geostatistical approaches would merge the advantage of using the sparse coverage of the seismic with its limited frequency bandwidth and the advantage of well log data and their high frequency (Figure 4.5). Hence, there are more constraints on the geostatistical process which yields a higher frequency and also produces a higher resolution inversion temporally compared to the input seismic data (Haas and Dubrule, 1994).

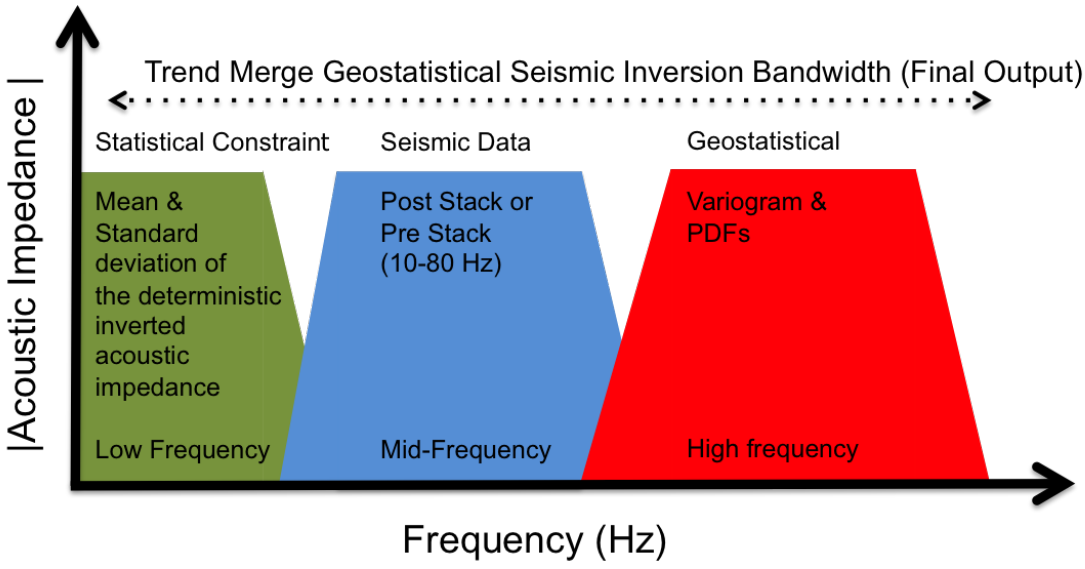

Figure 4.5: Geostatistical inversion in frequency domain. Merging the three different data yield a wider frequency contribution in frequency domain which would translate into a shaper wiggles in time domain. This increases the resolution of the output results compared to the initial input (Modified from Dubrule, 2003).

For our stochastic approach, we employed a flow that implements a Bayesian statistical search criteria using Markov chain Monte Carlo (MCMC). The inversion starts with selecting an empty grid point and then generates a random walk within an a priori defined probability density function (PDF). Then, we simulate our model using Sequential Gaussian Simulation (SGS) which uses the priori model. The prior model rely on statistical parameters including borehole acoustic impedance variogram vertically, final deterministic inverted acoustic impedance variogram laterally and stratigraphic mesh spatially (Figure 4.1) in addition to the previously extracted wavelets (Pendrel et al., 2004). The objective of the simulation is to find an estimate of the geostatistical parameters that produce results with sizes and shapes similar to what is expected and is seen in the CSSI results (Mao and Journel, 1999).

Unlike the deterministic methods, geostatistical methods do not provide a single discrete solution to the inversion problem. Instead, they provide sets of realizations which are all considered to be true based on the prior statistical model. Hence, it requires further analysis to rank the probability of occurrence of those realizations. However, in this paper, we have not chosen any criteria to rank all the realizations. We presented our results by taking the mean of 10 realizations. In addition, traditional geostatistical inversion does not honor seismic data, while the implemented algorithm attempts to match each randomly generated acoustic impedance trace to its seismic counterpart, hence, narrowing the solution space (Dubrule et al., 1998).

Geostatistical inversion, in the Jason software package, uses Bayesian inference by updating the probability to give the user posterior PDFs. Then, it generates realizations that match the known data. Each simulated acoustic impedance realization is convolved with the extracted wavelet to produce an inverted time amplitude trace. If the inverted trace matches the original seismic trace, then, the algorithm accepts that simulated acoustic impedance solution as a probable solution.

The variogram defines the level of spatially dependence in statistics as we try to match the model variogram to the experimental one. In addition, variograms are intended as a quality control to check that the property model matchs the probable geological spatial pattern. For simplicity, we can assume that our area of study consists of a specific number of layers (Gringarten and Deutsch, 2001).In this study we considered a seal, a reservoir and a base layer, which are all segregated based on depth picks and horizons interpretation. Therefore, we modeled six variograms, as each layer should have both vertical and horizontal variograms. Moreover, we generated PDFs between log-based acoustic impedance and the calculated effective pressure at the borehole for each layer separately.

Prior to modeling pore pressure stochastically, one needs to understand the nature of the pore pressure regimes and geological origin behind them. Different geological interpretation of the subsurface leads to different geostatistical modeling parameters. All geological properties show some degree of spatial continuity. In modeling, we attempt to quantify the spatial continuity of the property from the measured data; hence, the same spatial continuity is passed along so as to be generated later in the simulation process. There are many variogram models. Among the most commonly used models in geostatistics are the exponential, the Gaussian or the spherical models (Figure 4.6). The shape of the model before reaching sill directly affects the output shape of the simulation results (Gringarten et al., 1999; Kupfersberger and Deutsch, 1999).

Exponential variogram models are usually used with a rapidly changing variable where correlation decreases quickly. Therefore, the exponential variogram tends to measure a wider spectrum of that modeling part. This provides a higher resolution simulated statistical model, as the simulated results fluctuate rapidly. On the other hand, Gaussians are usually preferred in more continuous variables where the

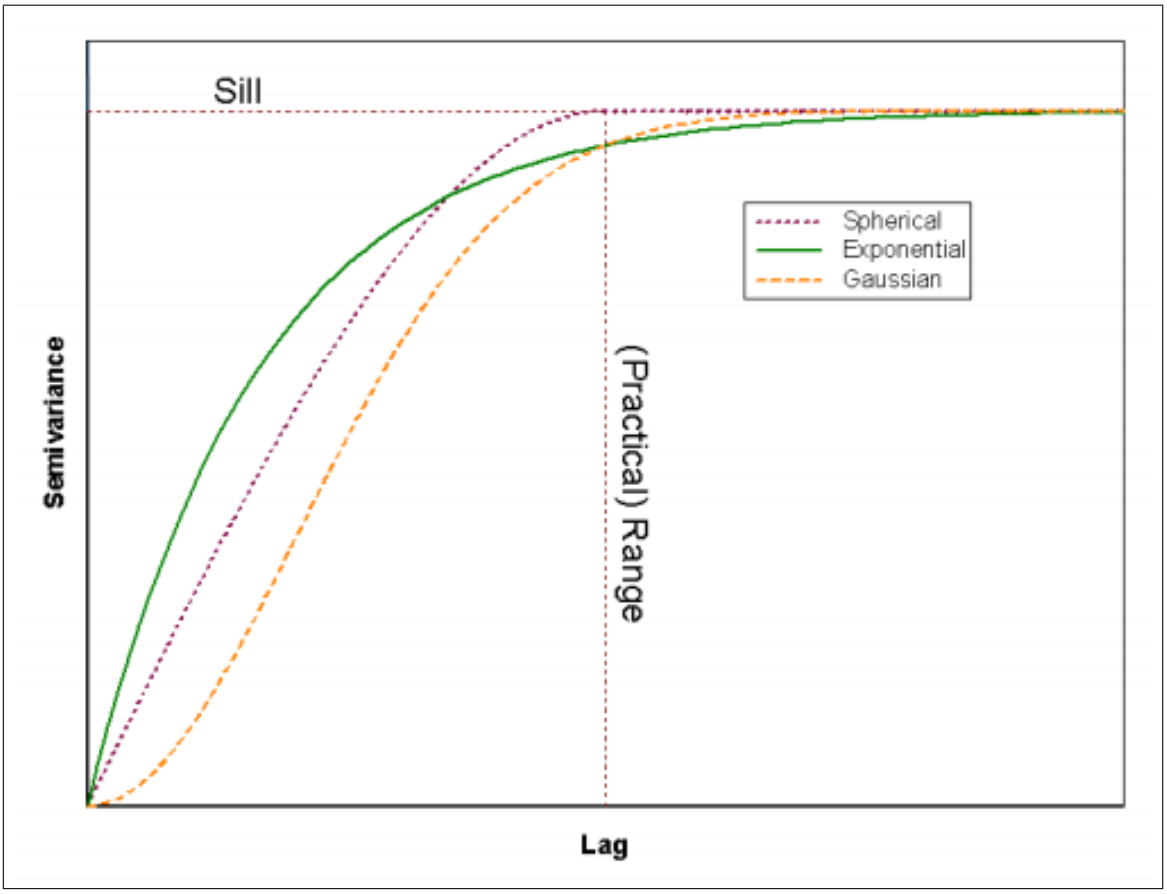

Figure 4.6: Different variogram models. Reprinted from (Bohling, 2005).

correlation decreases slowly (Bohling, 2005). Therefore, the result of its simulation should be smooth. We are modeling the variogram, not a fitting a curve. Therefore, the modeling parameters must mimic a geological interpretation in order properly present the statistical spatial distribution of the subsurface properties. Since, in the case of compaction disequilibrium, pore pressure is not expected to change laterally in a rapid manner, we used a Gaussian function (Figure 4.7).

Initially, we ran the simulation (Sequential Gaussian Simulation) without forcing a fit at the well location which allowed us to test our a priori statistical parameters to see if we could reproduce the measured acoustic impedance at the well location

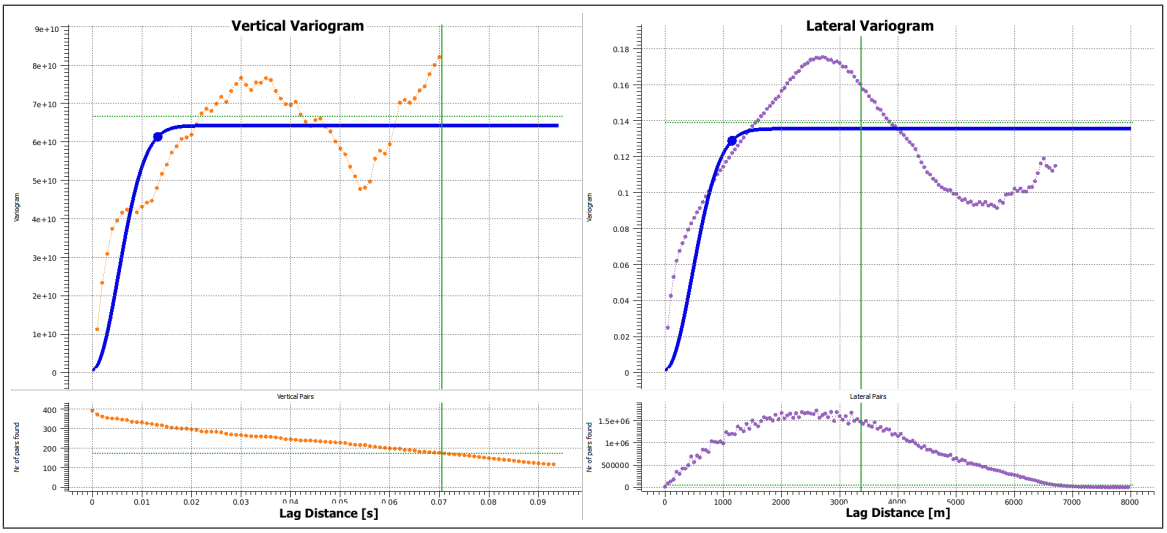

Figure 4.7: Acoustic impedance vertical and horizontal variogram.

using the simulation (Figure 4.8). At the simulation stage, we only used a priori PDFs, vertical variogram and horizontal veriogram without any constraints from the input seismic data as simulations are picked randomly based on the PDFs.

We quality controlled the simulation results by checking the results at the well location to see their degree of correlation. The PDFs of a property give a statistical model of the uncertainty about the unknown true value, whereas numerical reservoir models generated by the simulation are just realizations of the geostatistical model. Hence, our final simulation results should be consistent with the input statistics (spatiality), the wells (laterally) and CSSI results as well.

Furthermore, we extracted horizon attributes within the reservoir level. We extracted the mean of the simulated continuous property (mean of 10 simulated acoustic impedance). The mean attribute should indicate the mean of plausible geological features. This conditional simulation aims to provide the inversion algorithm with a heterogeneity model (Figure 4.8). The algorithm implementation should not be forced to honor the well location itself but to reproduce its main features at the well

location. Hence, we are not supposed to know where the wells after applying a proper conditional simulation (Dubrule, 2003). Due to limited computation power, we kept the number of realizations to 10. The more realization means the more control from seismic because more realization translate into a higher probability of matching the seismic later during inversion. Hence, less realization means more control from the wells (Dubrule, 2003).

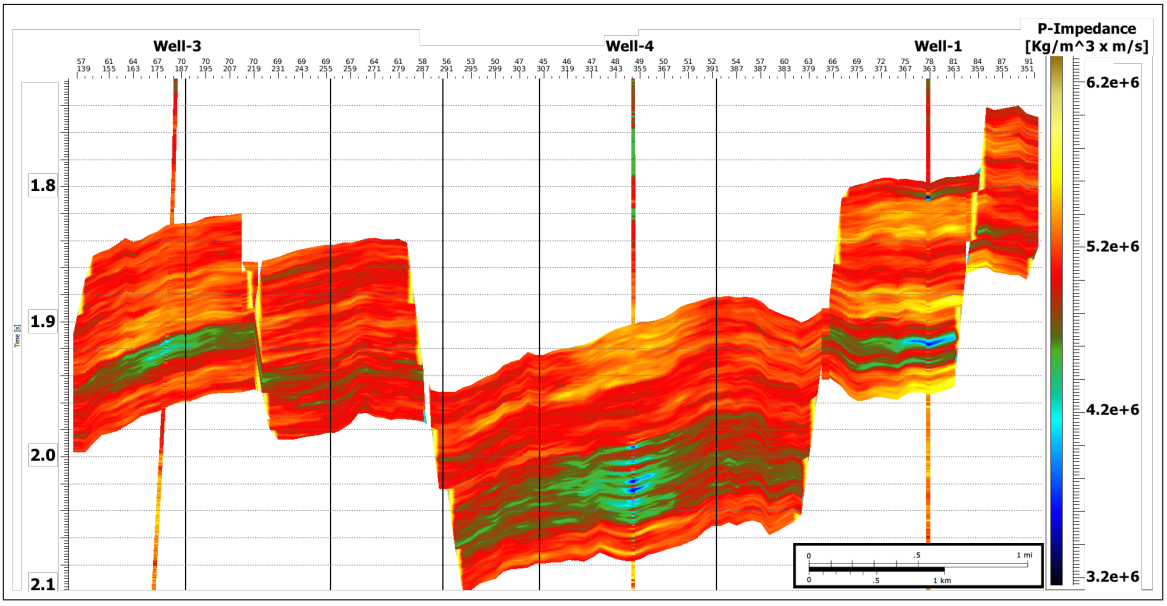

Figure 4.8: Mean of 10 simulated realizations. Simulation uses well data only and produce a geostatistical representation of the possible outcomes of the statistical heterogeneity.

The stochastic inversion yield a higher resolution image compared to the deterministic inversion. (Figure 4.9) illustrates frequency analysis on both inversion results. In short, the stochastic algohrtim has a wider frequency contribution in frequency domain when compared to the deterministic inversion which explains the higher resolution in time domain. This could be attributed to several reasons. First,

the stochastic inversion took the result of the deterministic inversion into account when building the statistical constrains of the low frequency model as well as building modeling the lateral variogram. Second, sequential gaussian simulation generated 10 realizations based on the well resolution and the inversion process attempted to match those realization to the seismic data which could provide unstable results if we increase the expected S/N.

MCMC provided more than one solution to the inversion problem. However, all inversion realizations honor seismic and well data but uncertainty comes from our injected low and high frequencies which are not controlled by seismic which can vary significantly (see Appendix A for more details). Using the simulated acoustic impedance from our conditional simulation step, MCMC uses that local realization to find the best match compared to the original seismic trace via convolution. Hence, it produces a global realization. This algorithm will not iterate until it converges, as it has an input of noise level that it assumes to help accept the solution. Noise constrains how tightly the models are constrained by the seismic. Hence, noise can be regarded as a tolerance level.

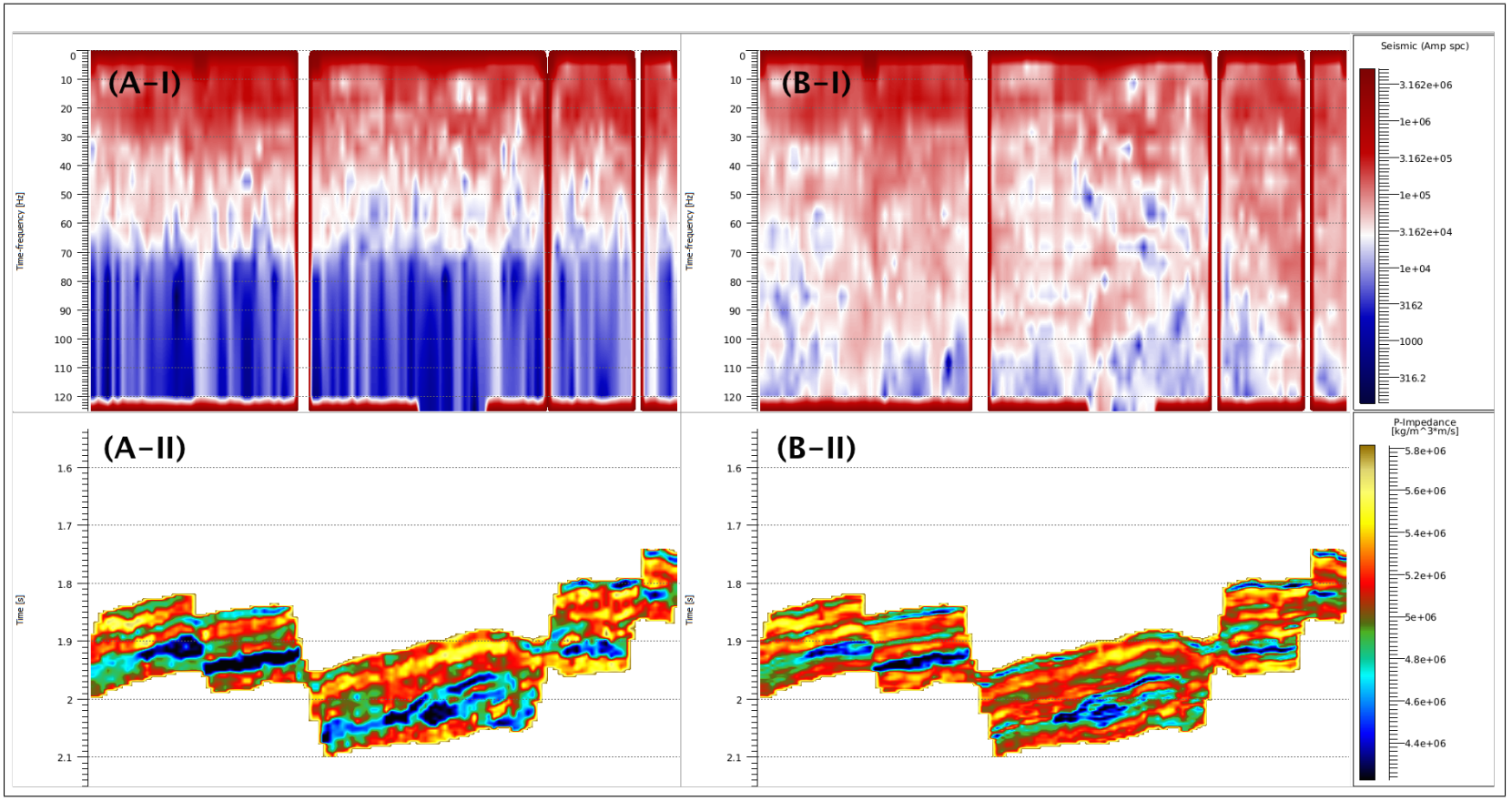

Figure 4.9: Frequency analysis for the inverted impedance. (A-I): frequency vs. offset plot for the deterministic inversion solution, (A-II): deterministic inversion, (B-I): frequency vs. offset plot for the stochastic inversion solution and (B-II): stochastic inversion.

4.2 Wellbore Pressure Predicition

We calculated Eaton's and Bower's pressures without any modification (Equations 3.4 and 3.7) (Figure 4.11). We assumed a negligible density effect and such assumption was valid within our area of study (Figure 4.10). NCT was carried out on compressional slowness in logarithmic scale (Figure 3.3). Then, we calculated the Eaton's pore pressure associated with that value of NCT. Overburden pressure calculation is solely done using depth, density log and gravitational constant. On the other hand, hydrostatic pressure was set to 0.41 psi/ft based on the GOM acceptable values (Dutta, 2005). (Appendix B.0.1) shows the MATLAB script that we implemented in our calculation.

The modified Bowers's approach requires recalculation of the hydrostatic acoustic impedance later which consists of a hydrostatic density. The hydrostatic density is rarely addressed in literature. Therefore, we dropped the density parameter with a constant density assumption in order to justify using the classical Bowers's equation. Transformation from acoustic impedance into effective pressure cannot be utilized in our study without assuming a negligible density effect which was observed in our dataset (Figures 4.10, 2.3). This assumption is not always valid, but within our area of interest and geological settings, density showed a linear relationship in borehole compressional velocity logs.

We constrained and compared our calculated pressure using Bowers's equation and Eaton's equation under minimum density effect assumption (Figures 2.3, 4.10). Both equations were verified against each other via correlation to reduce uncertainty, as we cross-plotted their results to verify the qualitative pressure values. The estimate of the Bowers pressure is larger than the Eaton pressure estimate for values less than 6000 psi, and slightly underestimated for pressure values greater than 8000 psi. Based

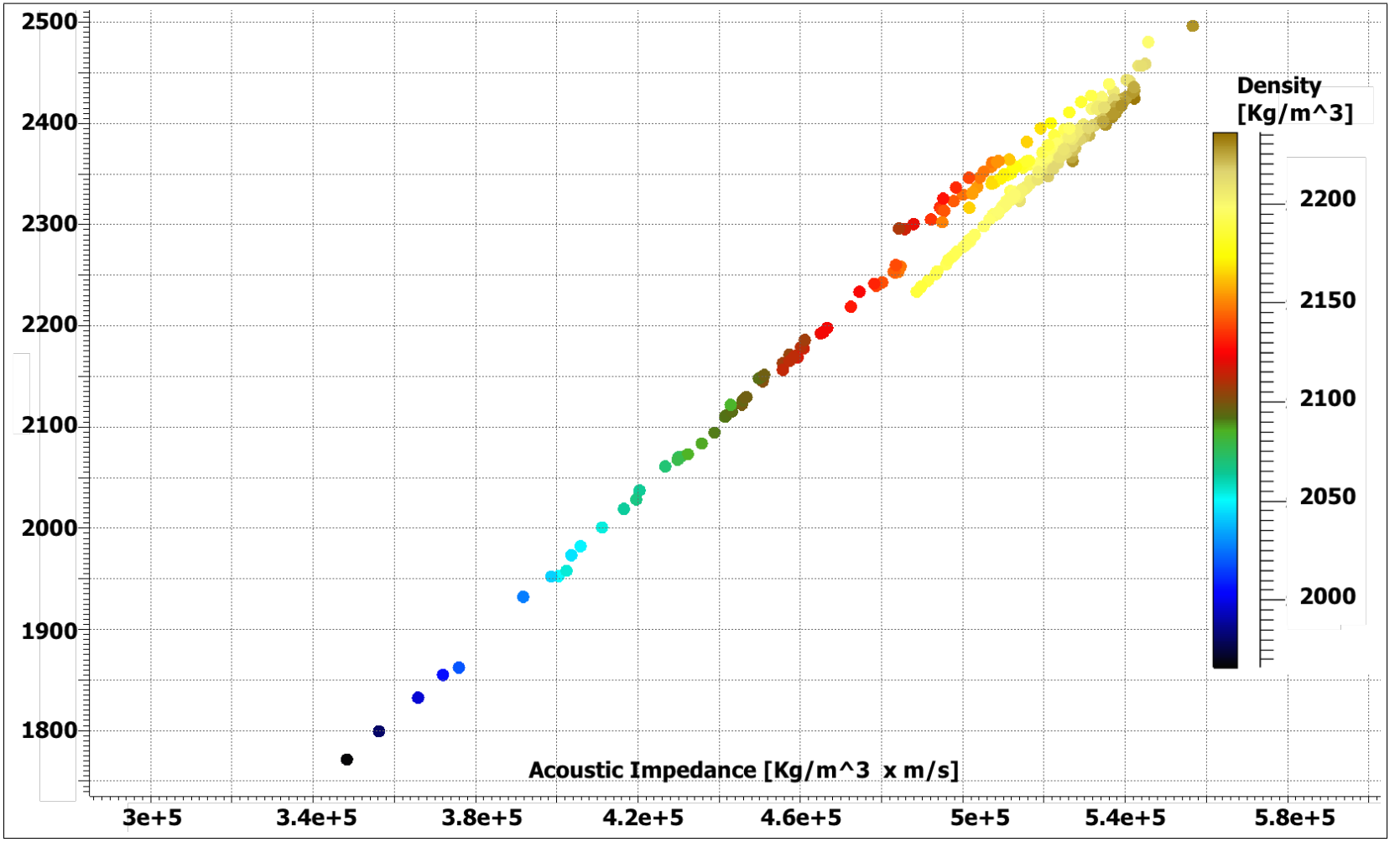

Figure 4.10: Cross plot showing acoustic impedance versus compressional velocity colored by density. Density color bar shows a linear density trend. We can also segregate three layers here: low density (potentially due to hydrocarbon) medium density and highly dense material (low porosity shaley sand).

on linear regression, the two methods have 86% correlation (Figure 4.12). Results were not equivalents in a quantitative sense, but showed a degree of correlation and overall matching in the effective pressure gradient (see Appendix A for more details).

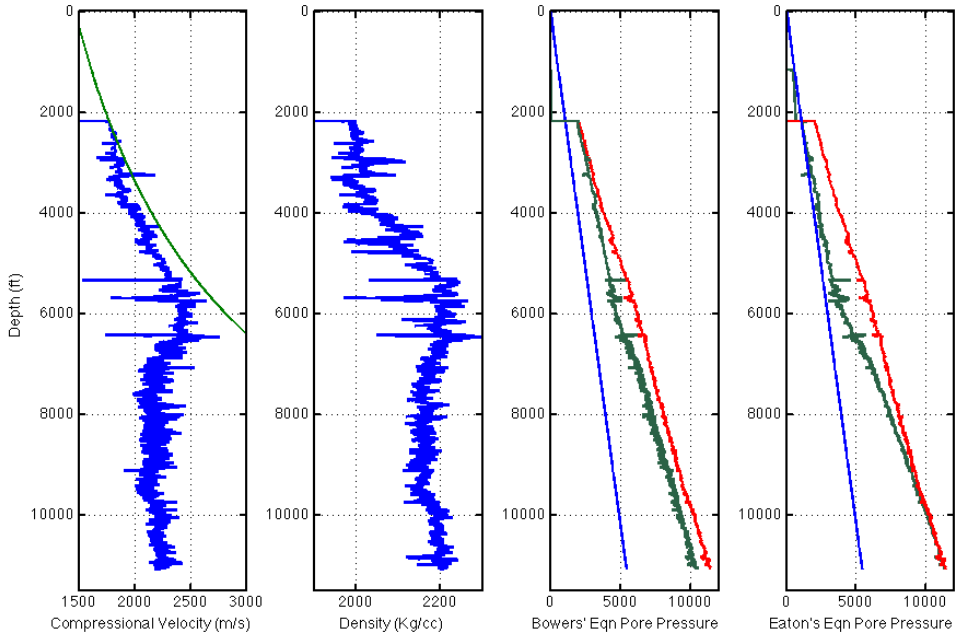

Figure 4.11: Petrophysical curves plotted against depth. From left to right: (1) Compressional velocity and normal compaction trend, (2) Density, (3) Bowers's equation pore pressure (red) bounded by overburden (green) and hydrostatic pressure (blue), and (3) Eaton's equation pore pressure (blue) bounded by overburden (green) and hydrostatic pressure (red). The plot also shows results of correlation between velocity and pressure as higher velocities correlated with higher pore pressure based on the color coded points.

4.3 Spatial Pressure Prediction

Within our frequency range, we attempted to establish a relationship between effective pressure and acoustic impedance. This paper addresses generating a quali-

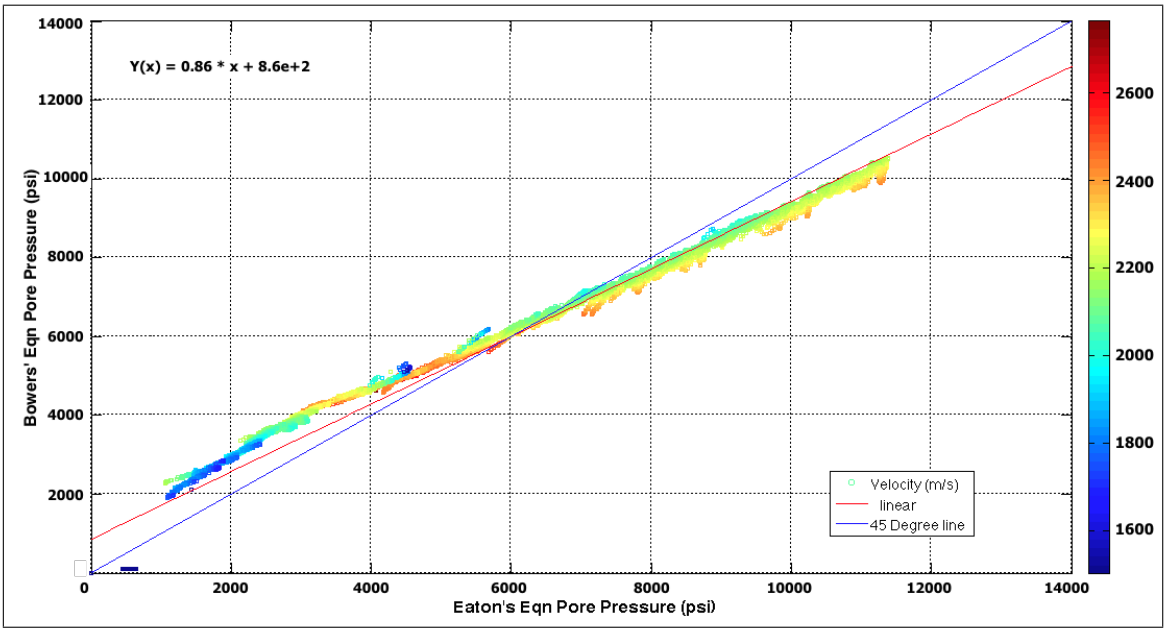

Figure 4.12: Cross plot of Eaton's equation pore pressure result vs. Bowers's equation pore pressure results color coded by compressional velocity. To visualize the similarity between the two methods, we plotted the 45-degree line to help interpret results. The estimate of the Bowers pressure is larger than the Eaton pressure estimate for values less than 6000 psi, and slightly underestimated for pressure values greater than 8000 psi.

tative pressure model. A model cannot include all parameters, especially in pressure prediction. Pressure is a function of compaction, tectonics, lithology, burial history, thermal profile and geochemistry and varies from one basin to another.

This paper addresses the effect of compaction only within a specific area where we observed a small variance in measured density spatially based on measured wellbore data (Figure 4.13). In order to shed the light on how to utilize the commonly available post-stack inversion products in pore pressure prediction, we followed two different methods. The first is based on a linear regression, while the second benefits from multi-dimensional statistical correlation.

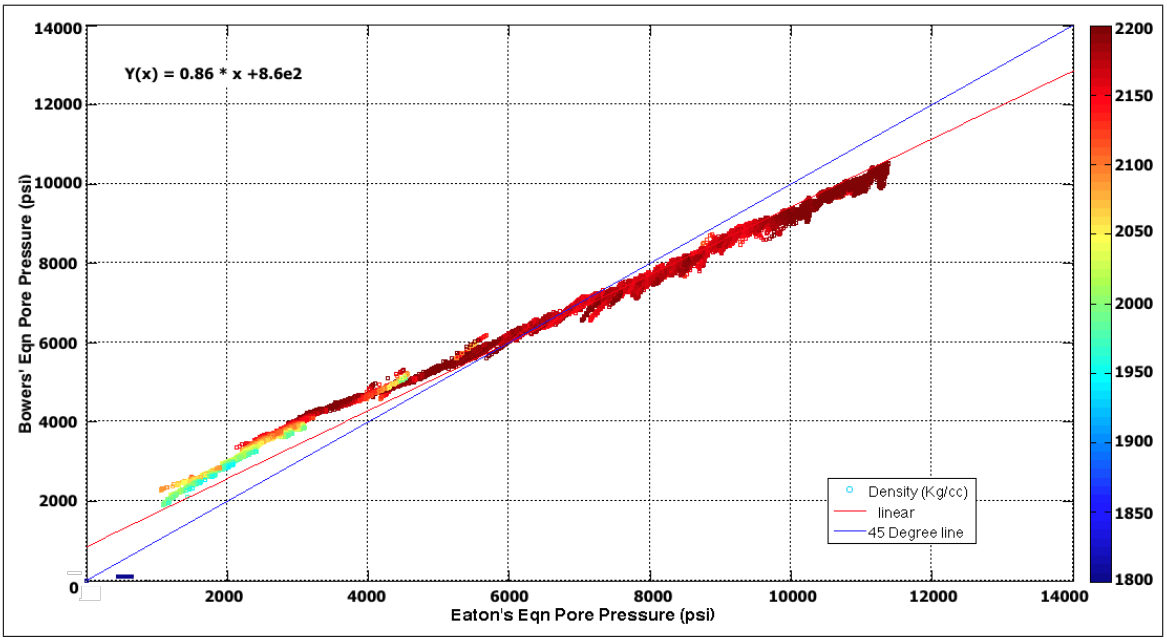

Figure 4.13: Cross plot between Bowers's predicted pore pressure and Eaton's predicted pore pressure at the borehole colored by the measured density at the borehole. Density color bar shows a linear density trend and negligible variance between 4000-6000 psi.

4.3.1 Linear Regression Method

In this approach, we attempted to develop a linear regression between the borehole calculated effective pressure based on Eaton's equation and the inverted acoustic impedance from the seismic post-stack deterministic inversion and stochastic inversion (Figure 4.14). Linear regression could be presented mathematically as:

$$EP_i = m \times AI_i + b + \varepsilon \tag{4.2}$$

where (EP) is the borehole calculated effective pressure, (AI) is borehole measured acoustic impedance acoustic impedance, (m) is the slope of the line, (b) is the effective pressure intercept which is equal to effective pressure at the surface and (ε) is a

random error term.

The Linear regression of effective pressure (psi) as a function of acoustic impedance ($kg/m^3 \times m/s$) color showed a 67% correlation between the two properties at the vertical wells within our defined interval. Effective pressure could be expressed as a function of acoustic impedance as below:

$$EP(AI) = 0.00106607 \times AI - 2671 \tag{4.3}$$

Within the area of interest and within our reservoir, we observed a negligible density effect (Figure 4.13). Density does not fluctuate significantly or shows a compaction trend; this fits our geological understanding of this area. Hence, most fluctuations within acoustic impedance occur due to variation in compressional velocity (see Appendix A for more details).

Moreover, we observed semi-linearity between effective pressure and impedance in Wells-1, 3 and 4 within our defined reservoir layer. Hence, we assumed that we could approximate the effective pressure away from the borehole using this linearity. The linear provided a fitted linear equation representing effective pressure as a function of acoustic impedance. We applied the regression equation on both the deterministic inverted volume and the mean of the 10 stochastic realizations.

Using a linear regression between effective pressure and acoustic impedance, we transformed the deterministic inverted acoustic impedance volume into an effective pressure volume (Figure 4.15). Results showed lower effective pressure at shale and slit strata compared to the reservoir. This indicates a higher pore pressure at the shale when we subtract it later from our overburden pressure model.

We generated an aerial weighted version of the effective pressure between the wells guided by our mesh model (Figure 4.16). This interpolation takes wellbore

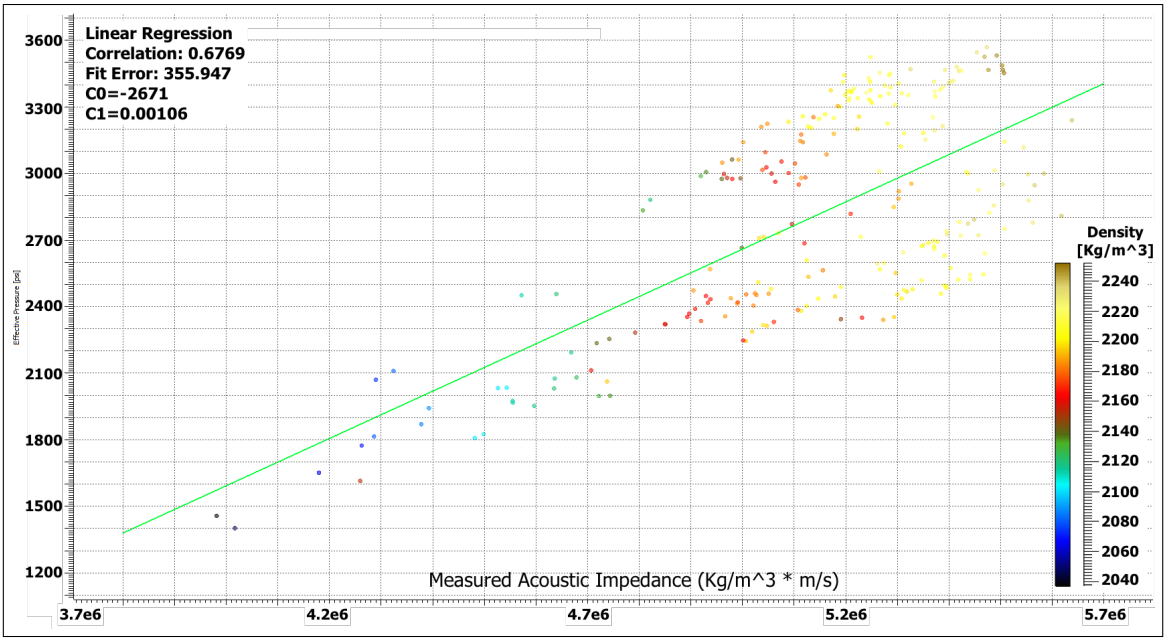

Figure 4.14: The linear regression of effective pressure (in units of psi) as a function of acoustic impedance ($kg/m^3 \times m/s$) color coded by density. Linear regression showed a 67% correlation between the two properties.

data only into account; hence, seismic data is not used at all. In fact, we applied the interpolation in the stratigraphic mesh domain without guidance from seismic data itself. This interpolation was generated in order to illustrate the difference in resolution and constrains that seismic inversion could provide to narrow the solution domain.

The linear regression approach applied on deterministic inversion showed an overall lower effective pressure at the reservoir layer (Figure 4.17). It also showed that the reservoir pressure terminates against the faults which could be interpreted as lack of pressure communication between different reservoir segments. Using these attributes, interpreters could pinpoint low effective pressure zones and target them due to their higher pore pressure which could be caused by hydrocarbon accumulation. In fact, the intersection of (in-line 70, crossline 215) shows a lower effective

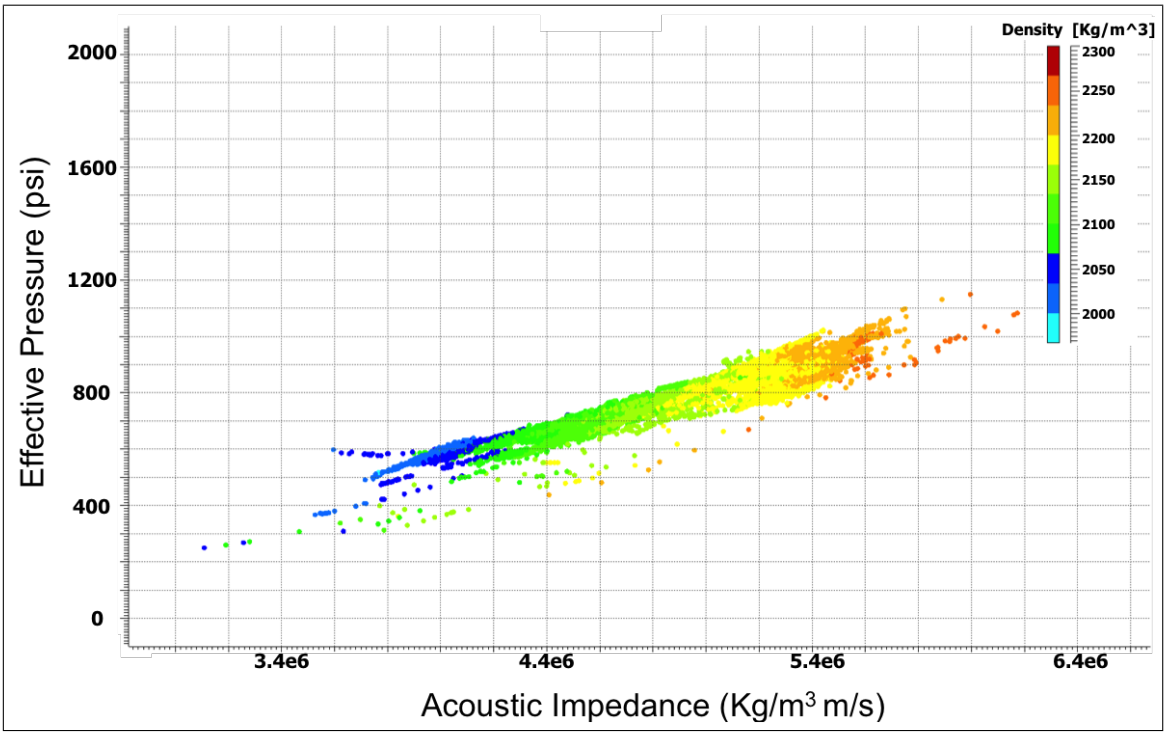

Figure 4.15: Effective pressure as a function of acoustic impedance, colored by density

pressure, which could be a good area to consider drilling. Furthermore, drillers can expect the change in the pressure gradient vertically within the seismic resolution limit that we found earlier between 35 to 50 m. We can observe that pressure is not rapidly varying laterally within shale and tight sand above and below the reservoir. Hence, linear regression provided a laterally smooth result that is consistent with our geological intuition as pressure does not change rapidly laterally without change in fluid or lithology. It also shows that some parts of the reservoir are pinching out against clinoforms spatially. However, the results do not perfectly match the well vertically, due to the limitations of the seismic and the inversion resolution.

Similarly, we also applied the same linear regression analysis to the stochastic inversion (Figure 4.18). We applied a linear regression transformation on the mean of 10 geostatistically inverted realizations to illustrate the mean effective pressure of

those 10 realizations. The input had a wider frequency bandwidth contribution, since the stochastic method provided a higher resolution inversion in comparison with the input of the deterministic inversion. Therefore, the linear regression appeared to have a higher resolution that resolved more features compared to the previous attempt (Figure 4.17). Overall, it shows consistent findings in comparison with the previous attempt with superior vertical resolution. For example, we can track a continuous, thin low effective pressure (in yellow) at the top of the reservoir between (in-line 70, crossline 220) all the way to (in-line 62, crossline 275) as observed in (Figure 4.18).This could be attributed to a continuous parallel deposition of shale that has a higher pore pressure compared to layers and formations around it. Hence, this could suggest one to increase mud weight prior to drilling this layer or cement casing shoe.

4.3.2 Cosimulation Method

Linear regression might not always hold true and might not represent the uniqueness of the datasets. It ignores perturbations in solution domain and provides the middle points in solution domain. For a small variance in acoustic impedance value, you could have a wide range of effective pressure. Therefore, we delineate our research into another statistical approach. In our research methodology, the stochastically inverted acoustic impedance was transformed into pressure using co-simulation. Cosimulation is a multi-dimensional statistical correlation that transforms acoustic impedance into the effective pressure based on statistical findings using a PDF of effective pressure as a function of acoustic impedance (Contreras et al., 2005). By definition, cosimulation provided us with the most probable value based on the defined histogram/PDF which is constrained by the variogram for effective pressure at the borehole (Ravalec-Dupin et al., 2011).

The assumption here that effective pressure could be presented as a function of

acoustic impedance is the centerpiece of modeling that is applied in this approach. In a cross plot between measured acoustic impedance and calculated effective pressure, for any given acoustic impedance point, we could encounter a wide range of pressure values. This range of possible pressure solutions can be illustrated as a histogram of that specific impedance value. Using the cosimulation algorthim, we can take a value from somewhere in the distribution that is known to reflect the pressure ranges for a specific acoustic impedance value. The cosimulation algorithm selects the proper statistical corresponding pressure value based on variogram modeling and PDF (Figure 4.19). Hence, it controls the fluctuation in selecting the pressure value from the histogram objectively; therefore, we can produce consistent smooth values for neighboring traces. Similarly to geostatistical inversion and simulation, cosimulation provideds as many realizations/simulations as we need. We chose 10 realizations to be consistent with the previous number of realizations already defined.

The cosimulation method was applied to whole interval by formulating different PDFs for the two different lithologies in our interval (Figure 4.20). The segregation between sand and shale based on Acoustic impedance, density and velocity was initially established in earlier stages (Figures 4.10, 2.3). Cosimulation could be also constrain using lateral variogram which we based on the previous linear regression findings (see Appendix A for more details). The cosimulation method provided a statistical solution with 10 realization that are all equiprobable. Such approach could help benefit constraining reservoir models and simulators as engineers will rank those realizations based on a user defined specific criteria.

The cousimulated effective pressure appears to have a higher resolution compared both linear regression solutions (Figure 4.22). However, it provided a more continuous reservoir sand despite our previous knowledge of the existence of clinoform barriers. Cosimulation is also sensitive to the variogram model and results

could change depending on the variogram shape. Nevertheless, cousimulation provided similar gradient trend when compared with linear regression and an overall correlation between results (Figure 4.21).

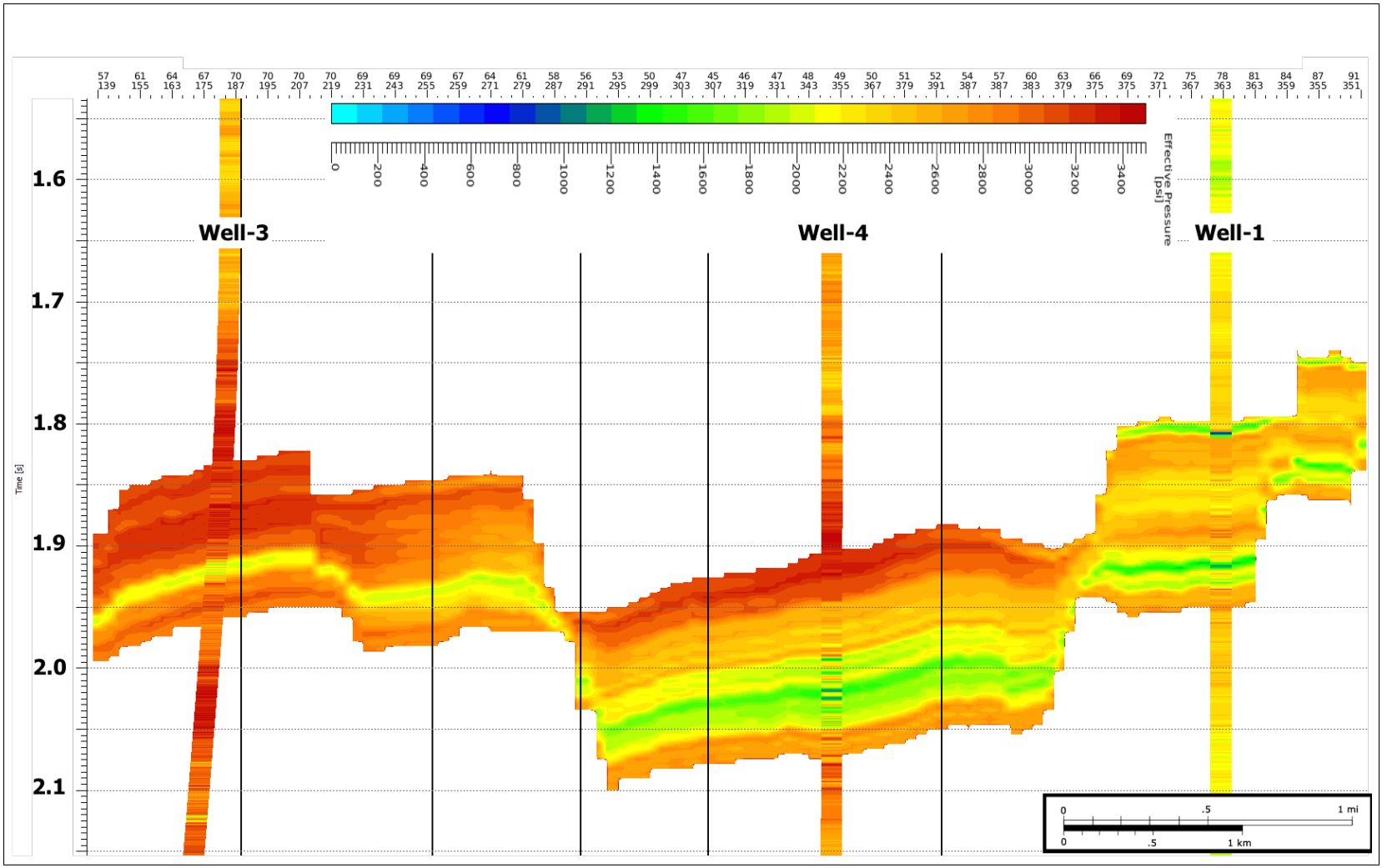

Figure 4.16: Aerial weighted interpolation of the calculated effective pressure using wellbore data. This interpolation uses the logs only and populate the result in the stratigraphic mesh. Hence, no seismic nor inversion is used here.

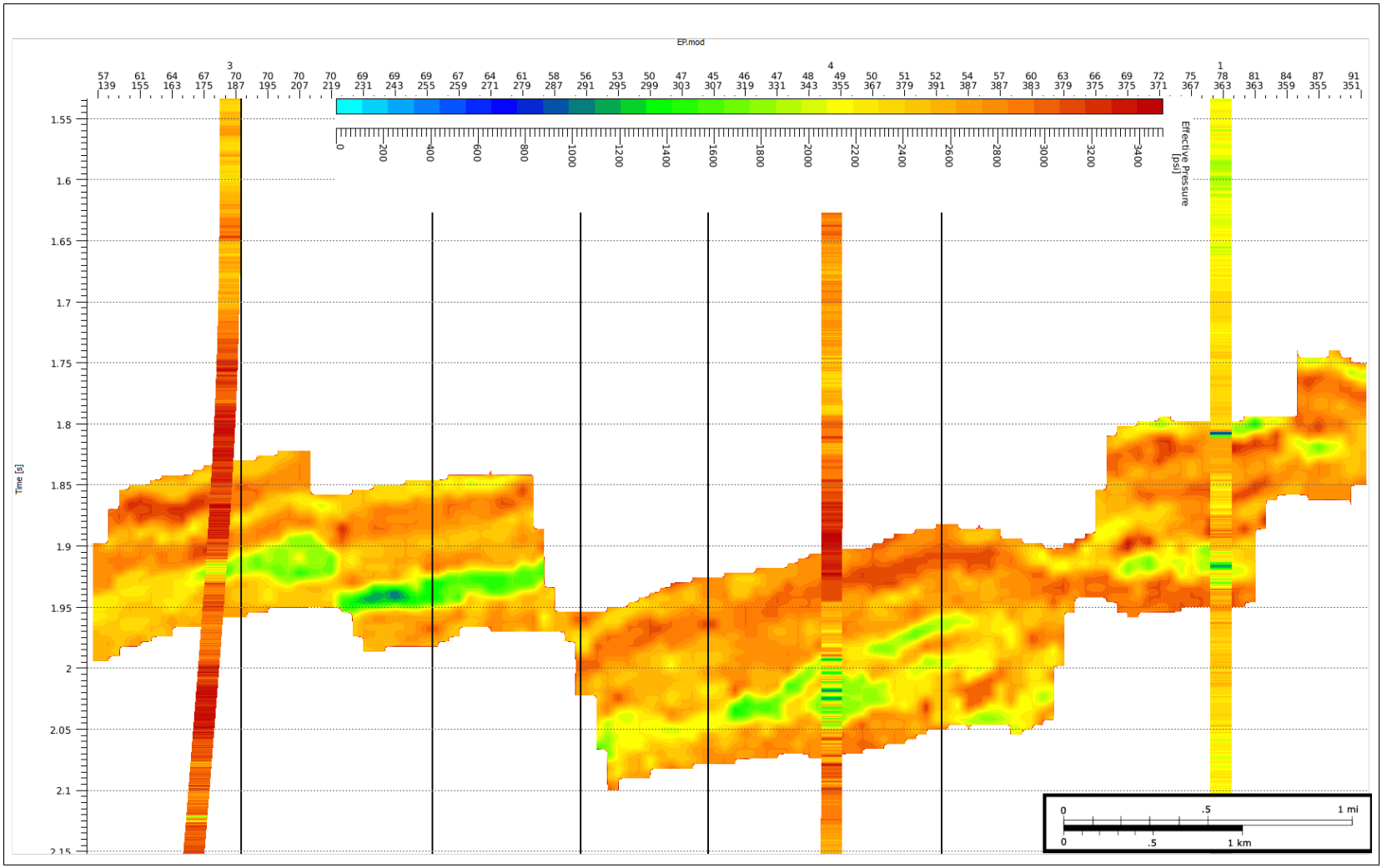

Figure 4.17: Effective pressure calculated using the linear regression approach based on the deterministic acoustic impedance inversion.

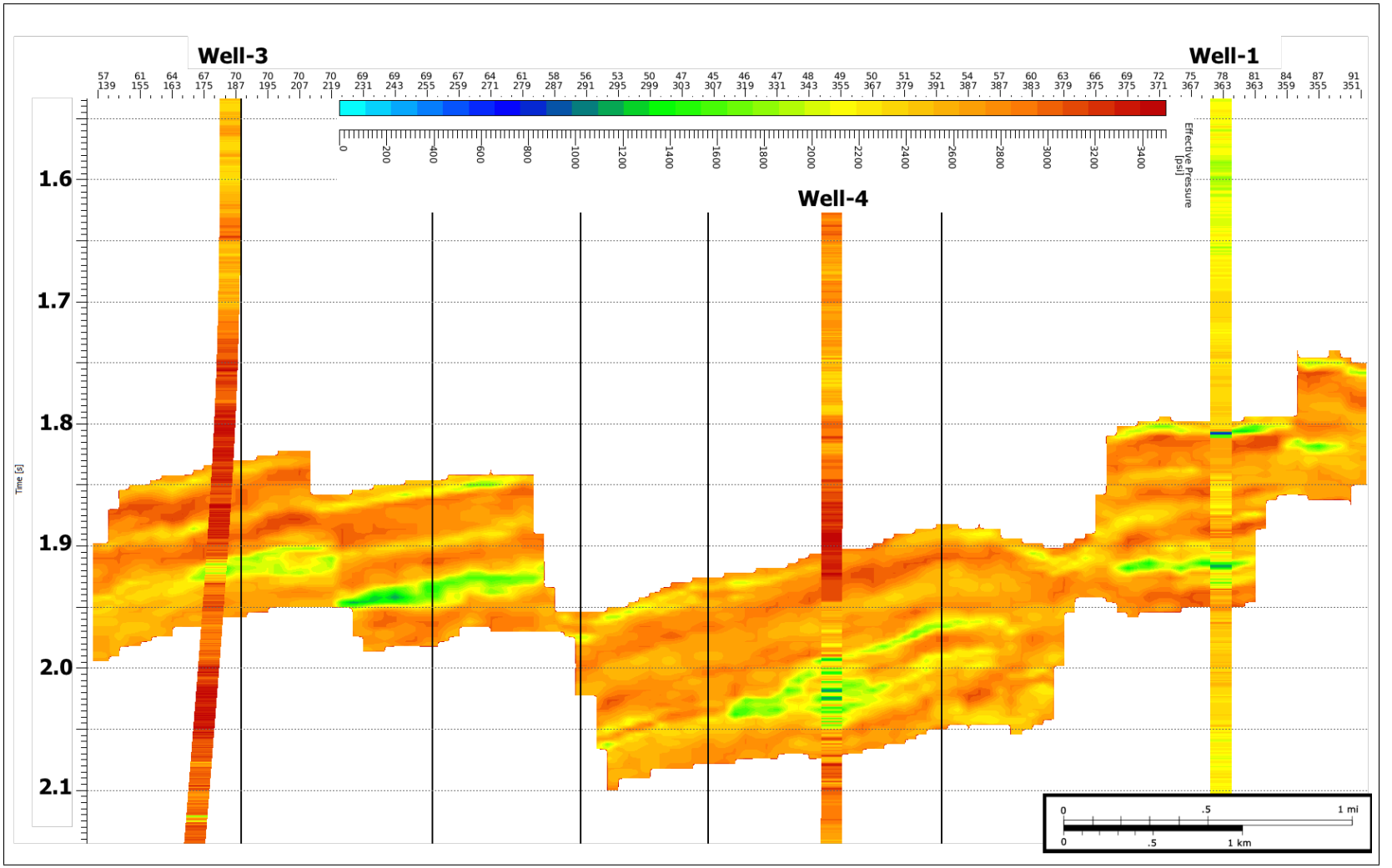

Figure 4.18: Effective pressure calculated using the linear regression approach based on the mean of the 10 realizations of the geostatistically inverted acoustic impedance volume.

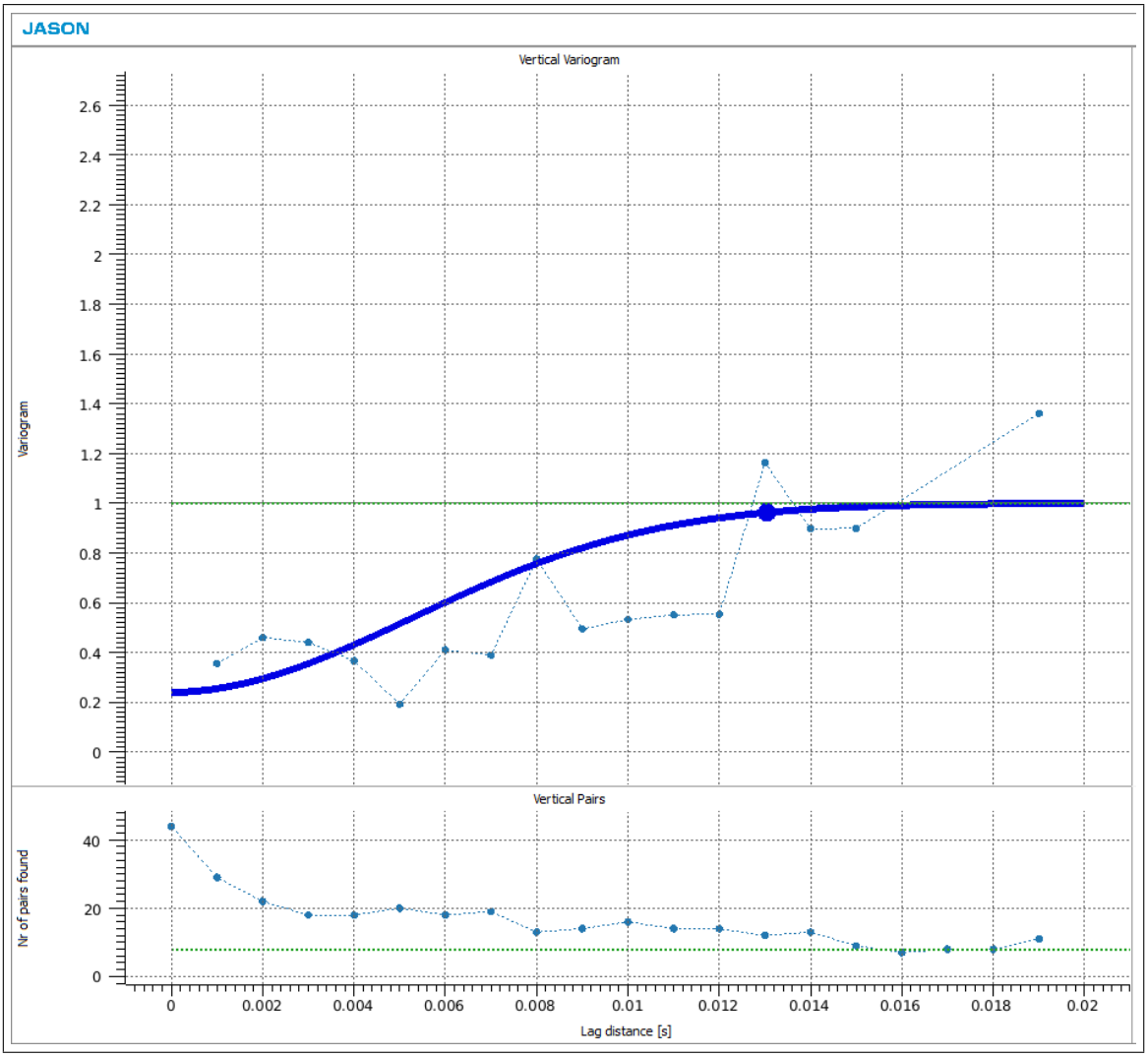

Figure 4.19: Experimental and modeled vertical variograms for effective pressure at the reservoir layer.

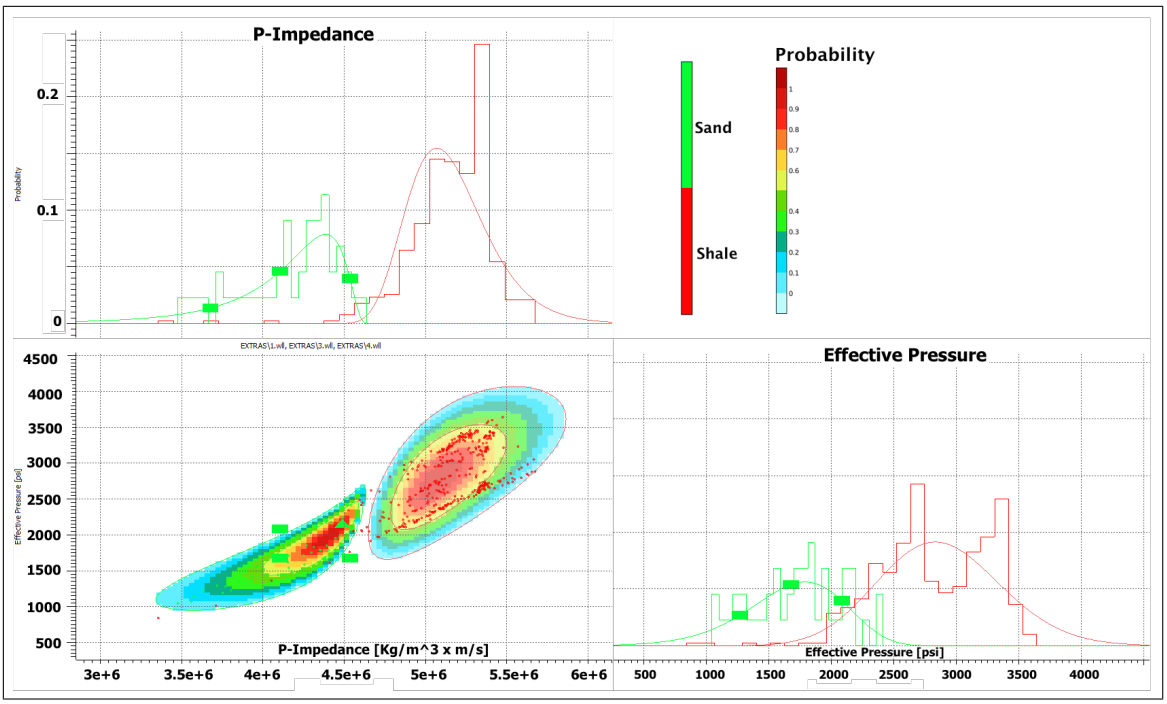

Figure 4.20: Cosimulation a priori statistical model, the probability density function at the well location based on the calculated effective pressure. PDFs are segregated based on a previously defined lithology.

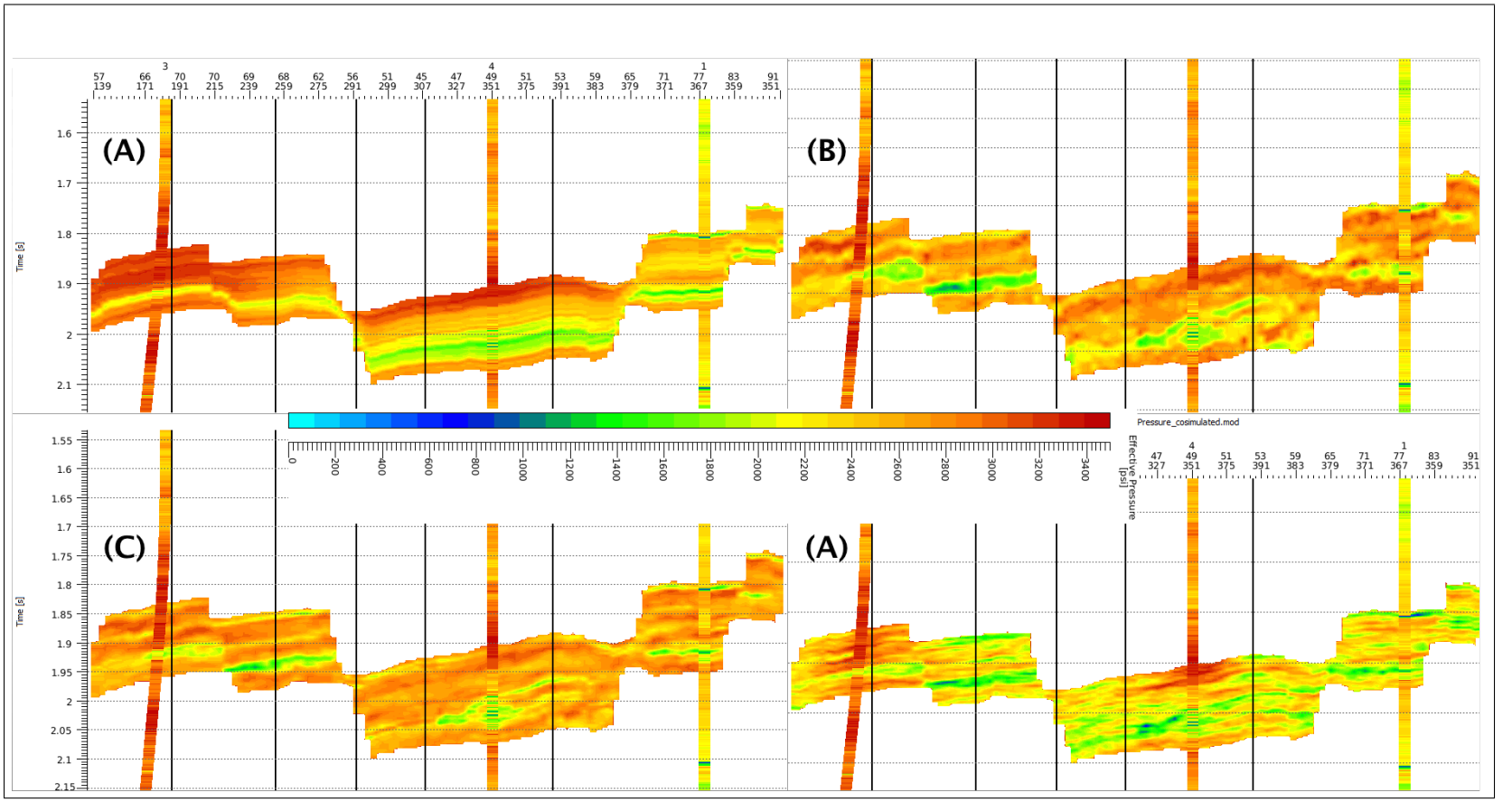

Figure 4.21: Effective pressure section view through Wells-1,3 and 4 using (A) log aerial weighted interpolation, (B) linear regression tranformation (deterministic inversion), (C) linear regression transformation (geostatistical inversion) and (D) cosimulated transformation (geostatistical inversion).

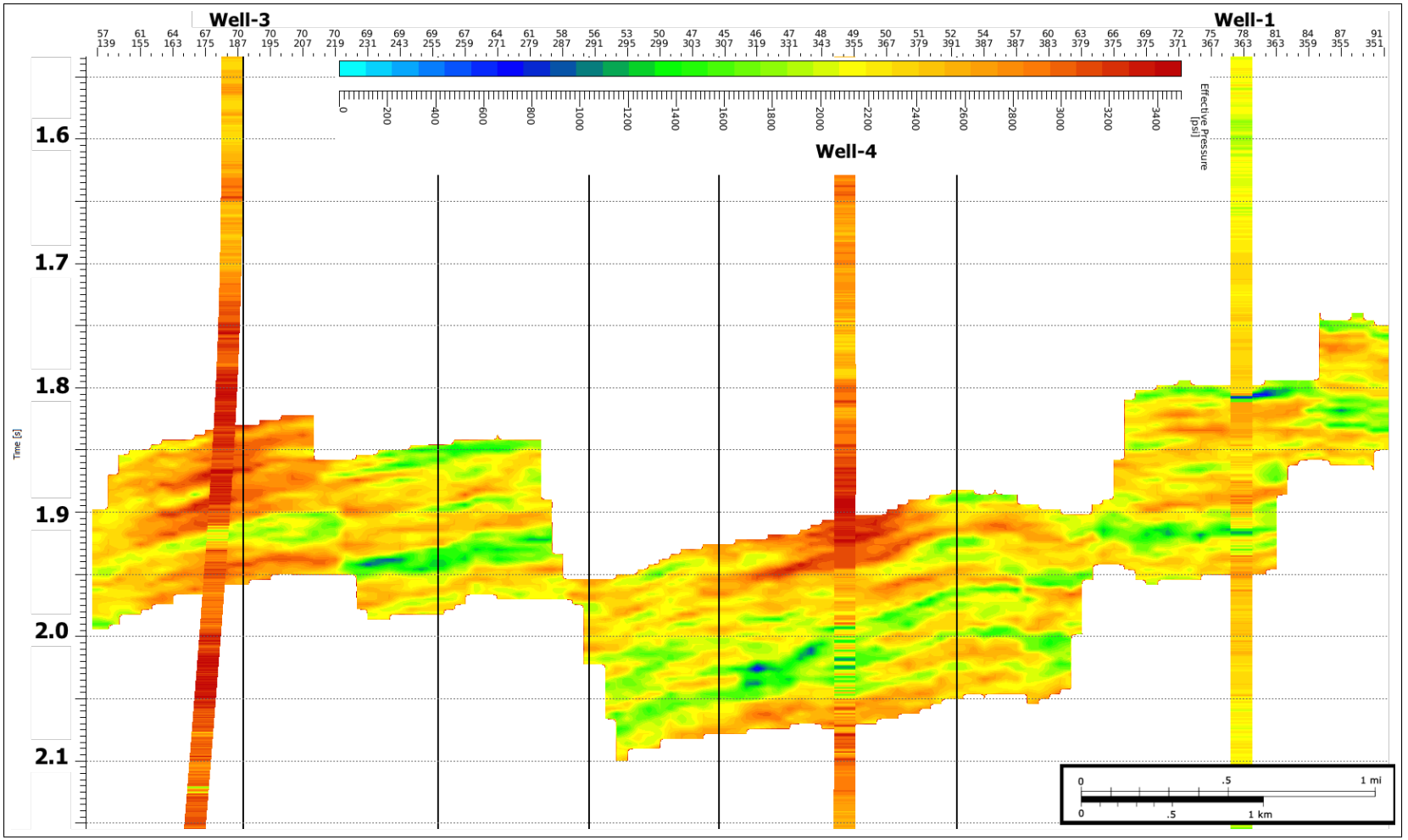

Figure 4.22: Effective pressure calculated using the cosimulation approach based on the mean of the 10 realization of the geostatistically inverted acoustic impedance volume.

5. CONCLUSION

We conducted our research flow (Figure 3.1) and generated a deterministic and a stochastic inversion using three wells from the GOM (Figures 5.1, 5.2). Then, we presented effective pressure as a function of acoustic impedance using two methods: (1) linear regression and (2) cosimulation (Figure 4.21). We compared the transformed effective pressure based on the deterministic and the stochastic inversion at the well location against our original log-based calculated effective pressure curve to quantify transformation error (see Appendix A for more details). Since the pressure values cannot be verified without direct pressure measurement, we reconstructed a pressure gradient curve based on geostatistical wellbore analysis from (Morris et al., 2015). We built a pressure gradient curve for our area using their mean values, standard deviation, and minimum and maximum pressure gradients. The reconstructed effective pressure curve was compared against our in situ calculated effective pressure to evaluate our final prediction (Figure 5.3).

Our research methodology showed a potential to be used for constraining a qualitative inference for pressure in absence of direct pressure measurements. The method did not determine a quantitative solution, as that would require direct pressure measurements. Hence, this study provided insights about the effective pressure for evaluating hydrocarbon presence, shale pressure and seal integrity, but is not intended for reservoir simulation. We confirmed our initial hypothesis, as we observed that impedance generally decreased where pressure increased in the area of interest.

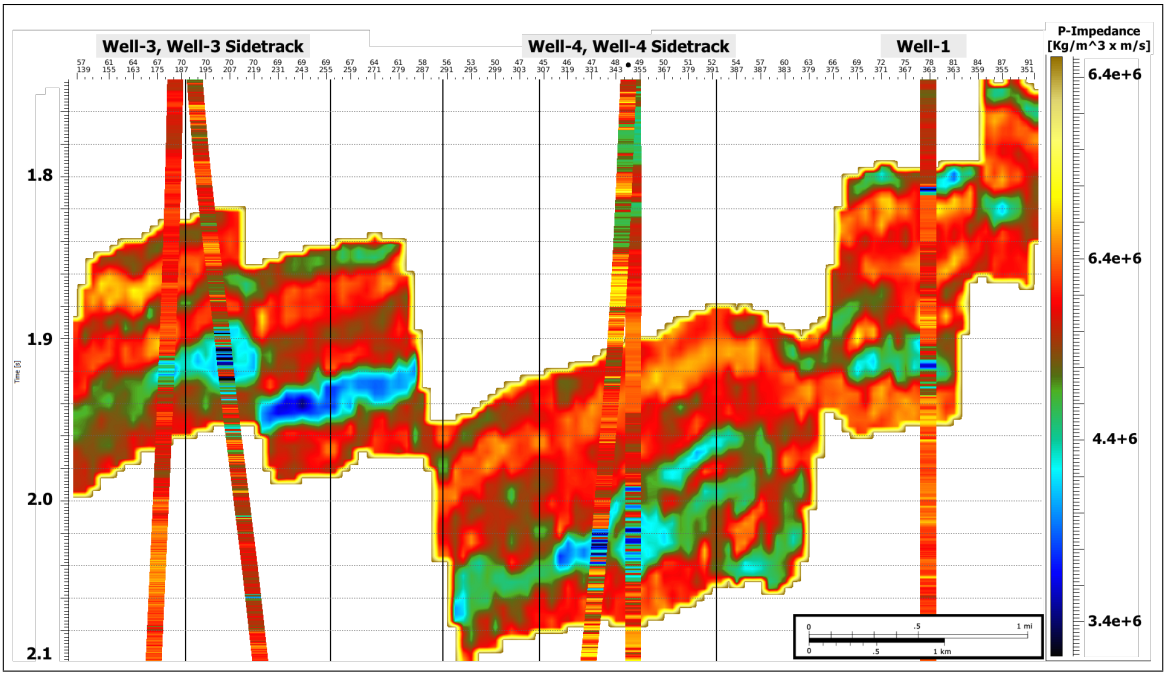

Figure 5.1: Deterministic inversion final results using CSSI.

Assuming correlation and causation, we can correlate impedance to pressure and present effective pressure as a function of acoustic impedance, only. Our approach utilized deterministic and stochastic seismic inversion in pore pressure prediction independently of direct pressure measurement and without using a seismic velocity model.

Within the dataset, our findings confirm the geological background of the area and visa versa, as we observed how different clinoforms could control pressure distribution. Results can help evaluate reservoir connectivity from a pressure communication perspective. However, the results are not meant to provide numerical solution for pressure. Results showed our research method is sensitive to the stratigraphic grid that controls modeling and attribute extraction, especially in geostatistical analysis. Different variogram models yielded different results; therefore, one needs a solid un-

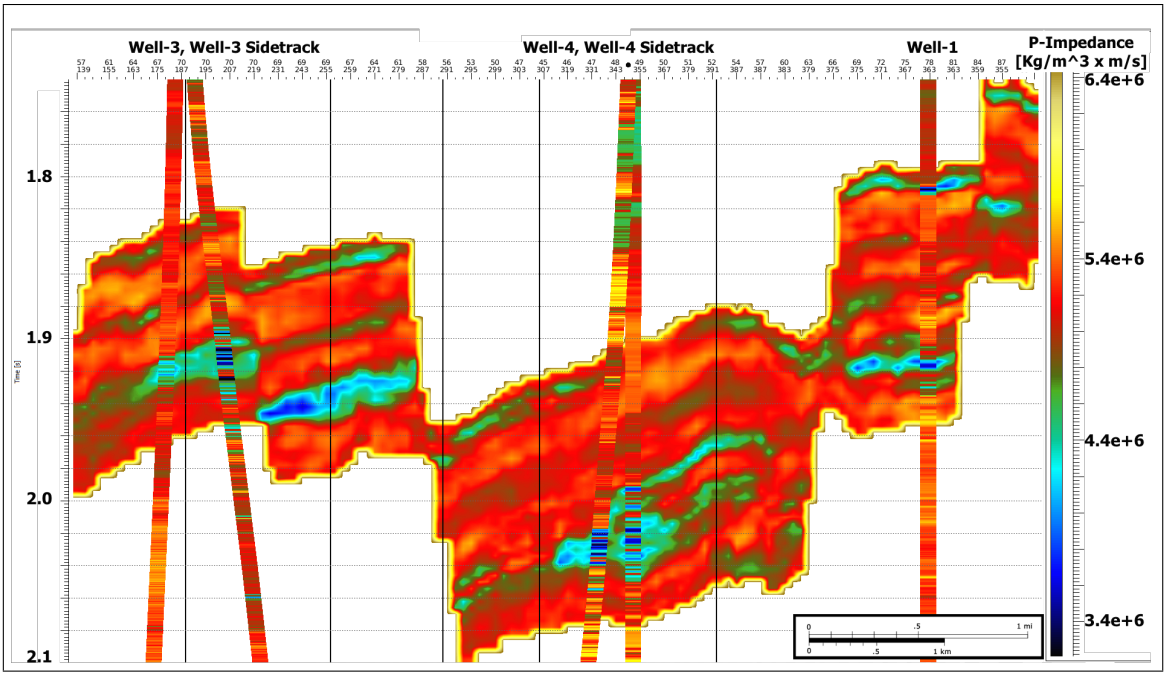

Figure 5.2: Stochastic inversion final results using MCMC.

derstanding of the modeled geological property in order to decide which variogram would serve better usage.

Eaton's equation, if properly calibrated, could be extrapolated away from the borehole using seismic inversion. In this paper, we only used a compressional based Eaton's equation. Eaton also provided an equation that adapts resistivity logs which could be also analyzed and tested. We quality-controlled our Eaton's method against Bowers's method; each provided different quantitive pressure values but agreed on the pressure gradients (see Appendix A for more details). In our inversion, the low frequency model was generated using a high-cut frequency filter on areal weight interpolation between the wells; however, if a seismic velocity model was presented, then it could serve building the low frequency model.

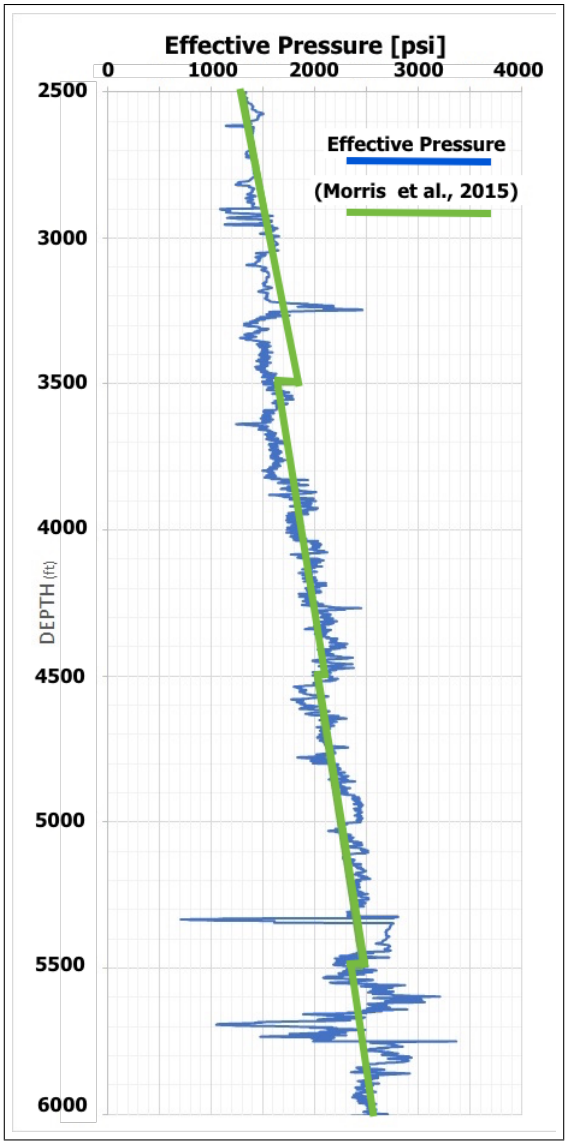

Figure 5.3: Effective pressure at Well-1: wellbore calculated effective pressure in blue versus Morris et. al (2015) reconstructed geostatistical pressure gradient curve in green.

Results within connected sand bodies showed relatively close numerical pressure values when compared to disconnected sand bodies. There will be at least two sources of non-uniqueness in results, but these are not likely to have a major impact on conclusions for the following reasons. First, the inversion non-uniqueness, which

we believe is reduced by combining vertical well data and spatial, horizontal sampling in seismic data. Second, non-uniqueness results from the acoustic impedance to pressure transformation, which was attributed to applying a the same linear regression to shale and sand interbedded layers. Those layers are below the seismic resolution, however; our transformation showed a better match at lower impedance values (shale) when compared to higher impedance values (sandstone). Hence, we had a relatively higher level of confidence in numerical values of pressure across shale layers. The predicted pressure gradient could be used to infer pressure across specific formations along a vertical wellbore trajectory as drilling engineering usually are more interested in setting their casing point before drilling into high pressure shale formations. On the other hand, we had less spatial confidence of our sandstone pressure prediction as acoustic impedance responses could be altered due to change in fluid and lithology. Within the geological observation of the area, it is unlikely there is any strong lithology change within the sandstone formation as those sand layers were spatially comfortably deposited with no stratigraphic constrains nor major change of sea level that would allow those layers to be altered into a different lithology. Moreover, three different transformation functions of two different acoustic impedance inversion methods still pinpointed to similar pressure regimes.

Our method differs from standard methods, as it did not employ seismic velocities. Instead, we used borehole compressional logs and/or borehole acoustic impedance logs. We approached the problem from a multi-disciplinary point of view using seismic data, geological interpretation, stratigraphy analysis, inversion, geostatistics, wellbore logs, wellbore empirical equations and published pressure figures based on mud weight and measured pressure. The research contributed to relating a log-based calculated effective pressure directly to the inverted acoustic impedance volumes using deterministic inversion. Furthermore, it contributed by utilizing stochastic

methods to address the non-uniqueness within our transformation process between the inverted acoustic impedance and calculated pressure using a statistical approach based on probability density function.

REFERENCES

Alchalabi, M. (1997). Parameter nonuniqueness in velocity versus depth functions. *Geophysics*, *62*(3), 970-979. Retrieved from http://dx.doi.org/10.1190/1.1444203 doi: 10.1190/1.1444203

Alfaraj, M., Hong, M.-R., Al-Dossary, S., Wang, J., and Rice, J. (2010). Wavelet extraction assessment for quantitative seismic interpretation. *First Break*, *28*(3).

Batzle, M., and Wang, Z. (1992). Seismic properties of pore fluids. *Geophysics*, *57*(11), 1396-1408. Retrieved from http://dx.doi.org/10.1190/1.1443207 doi: 10.1190/1.1443207

Bohling, G. (2005). Introduction to geostatistics and variogram analysis. *Kansas geological survey*, *2*.

Bosch, M., Mukerji, T., and Gonzalez, E. F. (2010). Seismic inversion for reservoir properties combining statistical rock physics and geostatistics: A review. *Geophysics*, *75*(5), 75A165–75A176.

Bowers, G. L. (1995). Pore pressure estimation from velocity data: Accounting for overpressure mechanisms besides undercompaction. *SPE Drilling*, *10*(02), 89-95.

Brown, R. J., and Korringa, J. (1975). On the dependence of the elastic properties of a porous rock on the compressibility of the pore fluid. *Geophysics*, *40*(4), 608–616.

Bruce, B., and Bowers, G. (2002). Pore pressure terminology. *The Leading Edge*, *21*(2), 170-173. Retrieved from http://dx.doi.org/10.1190/1.1452607

Christensen, N. I., and Wang, H. F. (1985). The influence of pore pressure and confining pressure on dynamic elastic properties of berea sandstone. *Geophysics*,

50(2), 207-213. doi: 10.1190/1.1441910

Contreras, A., Torres-Verdín, C., Chesters, W., Kvien, K., Fasnacht, T., et al. (2005). Joint stochastic inversion of 3d pre-stack seismic data and well logs for high-resolution reservoir characterization and petrophysical modeling: application to deepwater hydrocarbon reservoirs in the central gulf of mexico. In *Seg expanded abstracts* (Vol. 24, p. 1343).

Dickinson, G. (1953). Geological aspects of abnormal reservoir pressures in gulf coast louisiana. *AAPG Bulletin*, *37*(2), 410–432.

Dix, C. H. (1955). Seismic velocities from surface measurements. *Geophysics*, *20*(1), 68–86.

Domenico, S. N. (1984). Rock lithology and porosity determination from shear and compressional wave velocity. *Geophysics*, *49*(8), 1188–1195.

Doyen, P. M. (1988). Porosity from seismic data: A geostatistical approach. *Geophysics*, *53*(10), 1263–1275.

Dubrule, O., Thibaut, M., Lamy, P., and Haas, A. (1998). Geostatistical reservoir characterization constrained by 3d seismic data. *Petroleum Geoscience*, *4*(2), 121–128.

Dutta, N. C. (2002). Geopressure prediction using seismic data: Current status and the road ahead. *Geophysics*, *67*(6), 2012–2041.

Dutta, N. C. (2005). On the inversion of seismic amplitudes for lithology, fluid and pressure analysis. In *9th international congress of the brazilian geophysical society; expogef, salvador, bahia, brazil, 11-14 september 2005* (p. 1328-1330). Retrieved from `http://library.seg.org/doi/abs/10.1190/sbgf2005-263` doi: 10.1190/sbgf2005-263

Dutta, N. C., and Khazanehdari, J. (2006). Estimation of formation fluid pressure using high-resolution velocity from inversion of seismic data and a rock physics

model based on compaction and burial diagenesis of shales. *The Leading Edge*, *25*(12), 1528-1539. Retrieved from http://dx.doi.org/10.1190/1.2405339 doi: 10.1190/1.2405339

Dvorkin, J., Mavko, G., and Nur, A. (1999). Overpressure detection from compressional-and shear-wave data. *Geophysical Research Letters*, *26*(22), 3417–3420.

Eaton, B. A. (1969). Fracture gradient prediction and its application in oilfield operations. *Journal of Petroleum Technology*, *21*(10), 1–353.

Eberhart-Phillips, D., Han, D.-H., and Zoback, M. D. (1989). Empirical relationships among seismic velocity, effective pressure, porosity, and clay content in sandstone. *Geophysics*, *54*(1), 82-89. Retrieved from http://dx.doi.org/10.1190/1.1442580 doi: 10.1190/1.1442580

Francis, A. (2006). Understanding stochastic inversion: part 1. *First Break*, *24*(11).

Goodwin, R. H., and Prior, D. B. (1989). Geometry and depositional sequences of the mississippi canyon, gulf of mexico. *Journal of Sedimentary Research*, *59*(2).

Gringarten, E., Deutsch, C., et al. (1999). Methodology for variogram interpretation and modeling for improved reservoir characterization. In *Spe annual technical conference and exhibition.*

Gringarten, E., and Deutsch, C. V. (2001). Teacher's aide variogram interpretation and modeling. *Mathematical Geology*, *33*(4), 507–534.

Gutierrez, M. A., Braunsdor, N. R., and Couzens, B. A. (2006). Calibration and ranking of pore-pressure prediction models. *The Leading Edge*, *25*(12), 1516–1523.

Haas, A., and Dubrule, O. (1994). Geostatical inversion-a sequential method of stochastic reservoir modelling constrined by seismic data. *First break*, *12*(11),

561–569.

Hubbert, M. K., and Rubey, W. W. (1959). Role of fluid pressure in mechanics of overthrust faulting i. mechanics of fluid-filled porous solids and its application to overthrust faulting. *Geological Society of America Bulletin*, *70*(2), 115–166.

Kupfersberger, H., and Deutsch, C. (1999). Methodology for integrating analog geologic data in 3-d variogram modeling. *AAPG bulletin*, *83*(8), 1262–1278.

Landrø, M. (2001). Discrimination between pressure and fluid saturation changes from time-lapse seismic data. *Geophysics*, *66*(3), 836–844.

Latimer, R., Bahret, S., Sullivan, C., Horine, R., Mills, W., Sturrock, V., et al. (1999). Reservoir characterization using geostatistical inversion for the amberjack field, offshore gulf of mexico. In *Seg, annual meeting, technical program. houston.*

Magara, K. (1978). *Compaction and fluid migration* (First Edition ed.). Elsevier Scientific.

Mao, S., and Journel, A. G. (1999). Conditional 3d simulation of lithofacies with 2d seismic data. *Computers and Geosciences*, *25*(7), 845–862.

Mayall, M., Yeilding, C., Oldroyd, J., Pulham, A., and Sakurai, S. (1992). Facies in a shelf-edge delta–an example from the subsurface of the gulf of mexico, middle pliocene, mississippi canyon, block 109 (1). *AAPG Bulletin*, *76*(4), 435–448.

Morris, S., Vestal, B., O'Neill, K., Moretti, M., Franco, C., Hitchings, N., ... Grace, J. D. (2015). The pore pressure regime of the northern gulf of mexico: Geostatistical estimation and regional controls. *AAPG Bulletin*, *99*(1), 91–118.

Niranjan, B., Adam, K., Charles, W., Charles, I., Vinod, A., and Ivan, P. (2014). Predrill prediction of subsalt pore pressure from seismic impedance. *The Leading Edge*, *33*(4), 400-412. Retrieved from `http://dx.doi.org/10.1190/tle33040400.1` doi: 10.1190/tle33040400.1

Pendrel, J., Leggett, M., Mesdag, P., et al. (2004). Geostatistical simulation for

reservoir characterization. *CSEG Annual M fleeting Abstracts*.

Pennebaker, E. (1968). Seismic data indicate depth, magnitude of abnormal pressure. *World Oil*, *166*(7), 73–78.

Pilcher, R., Trude, J., Kilsdonk, B., Quinn, M., and Graham, R. (2009). Primary basin boundaries in the gulf of mexico: Three hydrocarbon trap types with distinct petroleum systems implications.

Pyrcz, M. J., and Deutsch, C. V. (2014). *Geostatistical reservoir modeling* (S. Edition, Ed.). Oxford university press.

Ravalec-Dupin, L., Tillier, E., Da Veiga, S., et al. (2011). Incorporating 3-d seismic, well and production data into reservoir models using co-simulation. In *Spe europec/eage annual conference and exhibition.*

Samson, P., Dubrule, O., Euler, N., et al. (1996). Quantifying the impact of structural uncertainties on gross-rock volume estimates. In *European 3-d reservoir modelling conference.*

Sayers, C. M., Johnson, G. M., Denyer, G., and Bartman, R. C. (2002b). Predrill porepressure prediction using seismic data. *Geophysics*, *67*(4), 1286-1292. doi: 10.1190/1.1500391

Sayers, C. M., Woodward, M. J., Bartman, R. C., and Sayers, C. M. (2002a). Seismic pore-pressure prediction using reflection tomography and 4-c seismic data. *The Leading Edge*, *21*(2), 188–192.

Shapiro, B., Pampell, E., et al. (1985). Seismic inversion of vertical seismic profile data for predicting abnormal pressure beyond td. In *Offshore technology conference.*

Smith, M. A. (2002). Geological controls and variability in pore pressure in the deep-water gulf of mexico. *Memoir-The American Association of Petroleum Geologists*, 107–114.

Soares, A. (2001). Direct sequential simulation and cosimulation. *Mathematical Geology*, *33*(8), 911–926.

Stone, D. G., et al. (1983). Predicting pore pressure and porosity from vsp data. In *1983 seg annual meeting.*

Stunes, S. (2012, June). *Methods of pore pressure detection from real-time drilling data* [Masther Thesis]. Department of Petroleum Engineering and Applied Geophysics, Norwegian University of Science and Technology.

Terzaghi, K., Peck, R. B., and Mesri, G. (1996). *Soil mechanics in engineering practice*. John Wiley and Sons.

Torres-Verdin, C., Victoria, M., Merletti, G., and Pendrel, J. (1999). Trace-based and geostatistical inversion of 3-d seismic data for thin-sand delineation: An application in san jorge basin, argentina. *The Leading Edge*, *18*(9), 1070–1077.

Vanorio, T., Mavko, G., Vialle, S., and Spratt, K. (2010). The rock physics basis for 4d seismic monitoring of co2 fate: Are we there yet? *The Leading Edge*, *29*(2), 156-162. Retrieved from `http://dx.doi.org/10.1190/1.3304818` doi: 10.1190/1.3304818

APPENDIX A

FIGURES

This appendix provides more details and figures about this paper. We implemented a detailed tests on all wells. Moreover, some key figures are replotted here with a higher resolution.

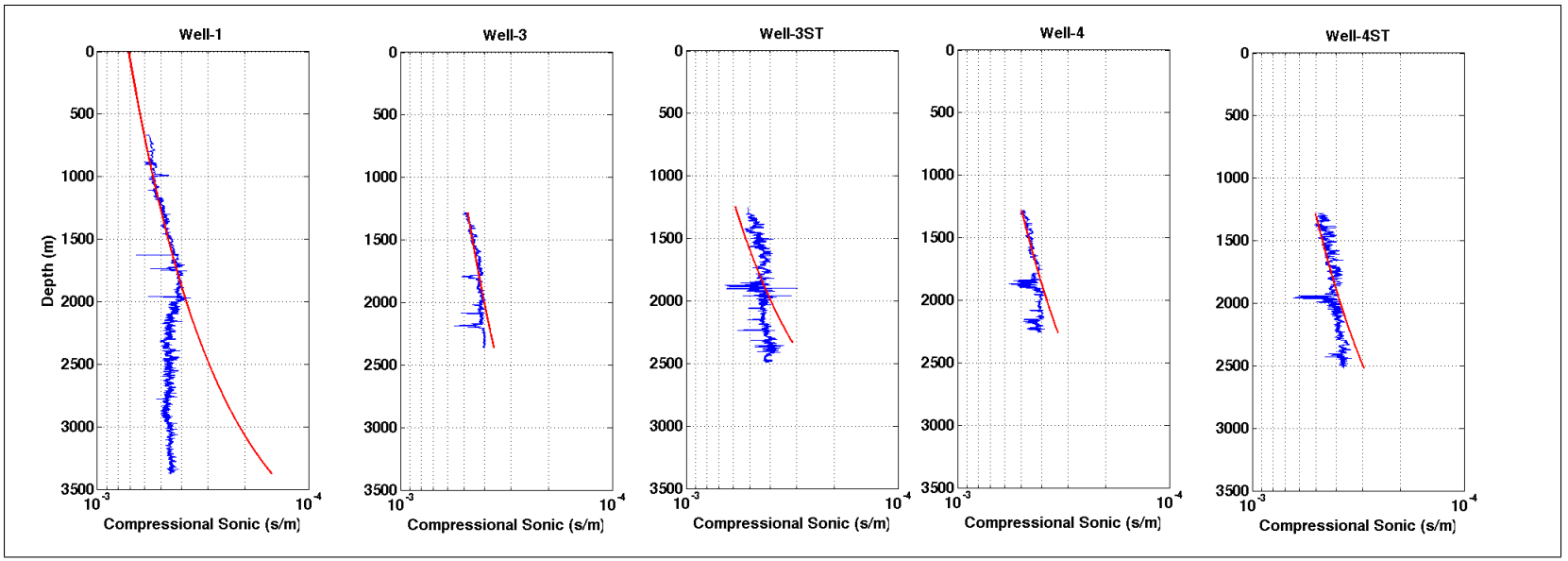

Figure A.1: Normal compaction trend analysis for the 5 wells. The three vertical wells show similar trend while the side track wells are off. A global NCT was derived based on the three vertical wells only. Note that only Well-1 has compressional sonic log to the surface.

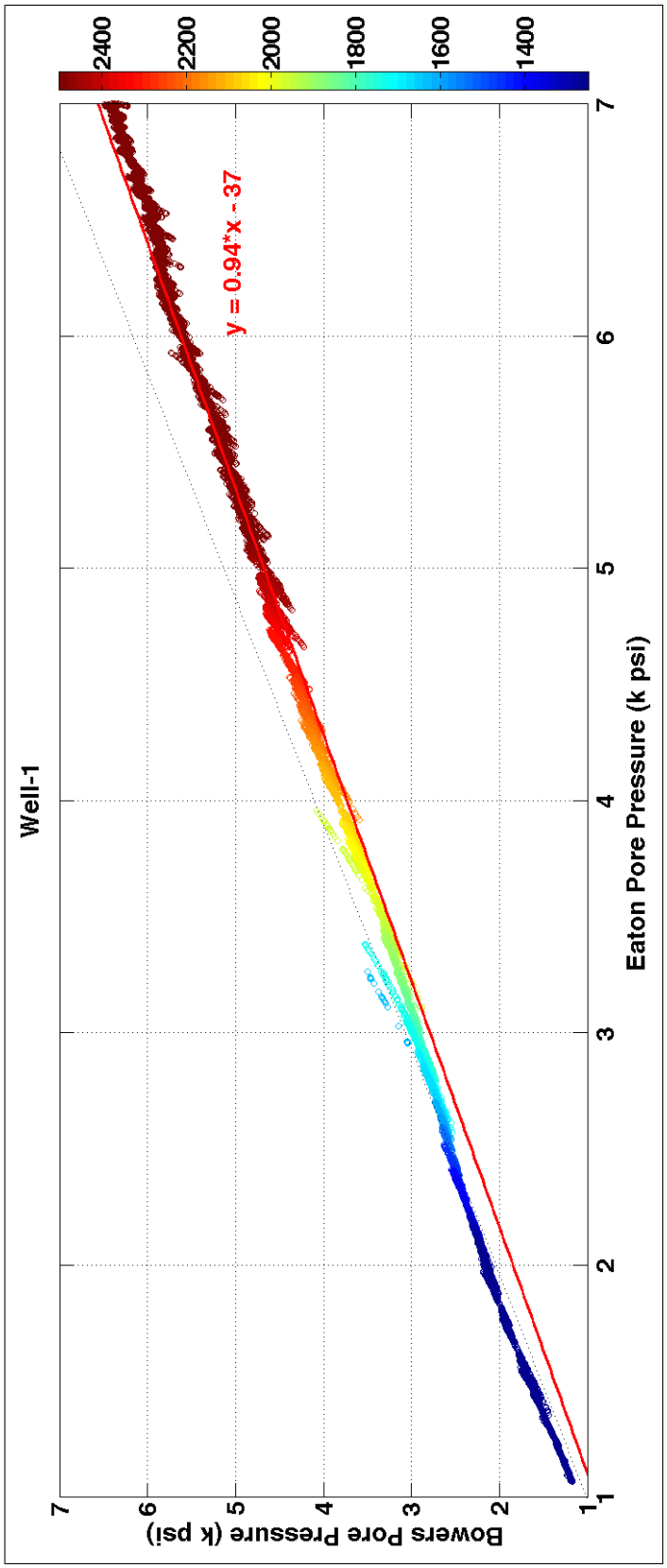

Figure A.2: Eaton's vs. Bowers's pore pressure prediction at borehole (Well-1).

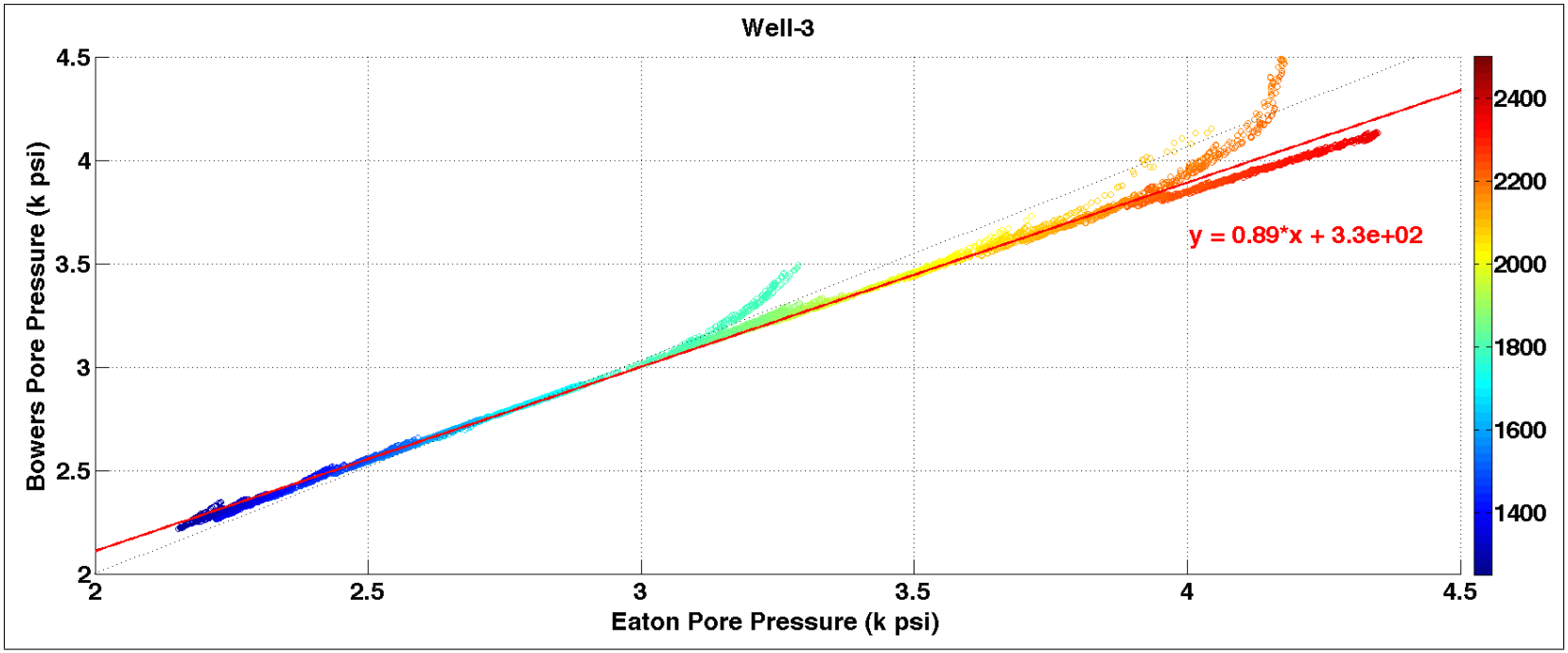

Figure A.3: Eaton's vs. Bowers's pore pressure prediction at borehole (Well-3).

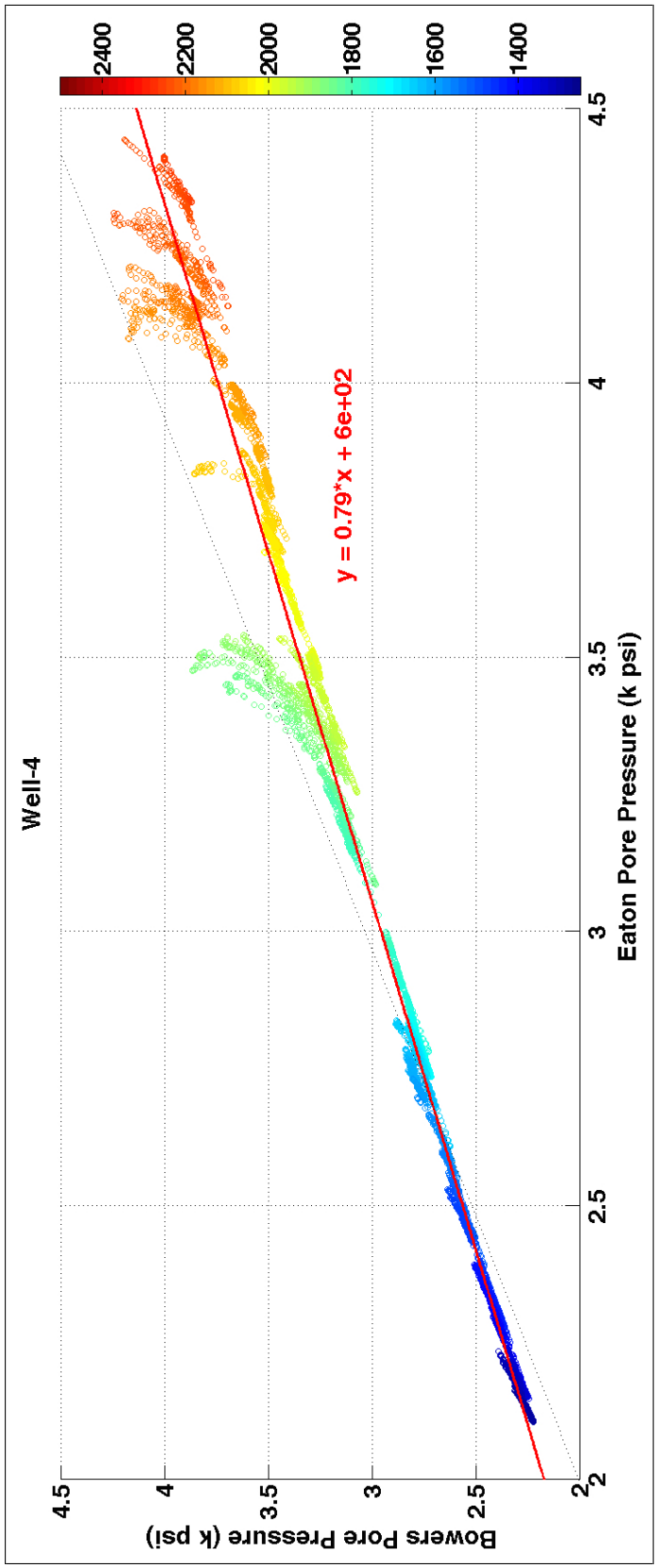

Figure A.4: Eaton's vs. Bowers's pore pressure prediction at borehole (Well-4).

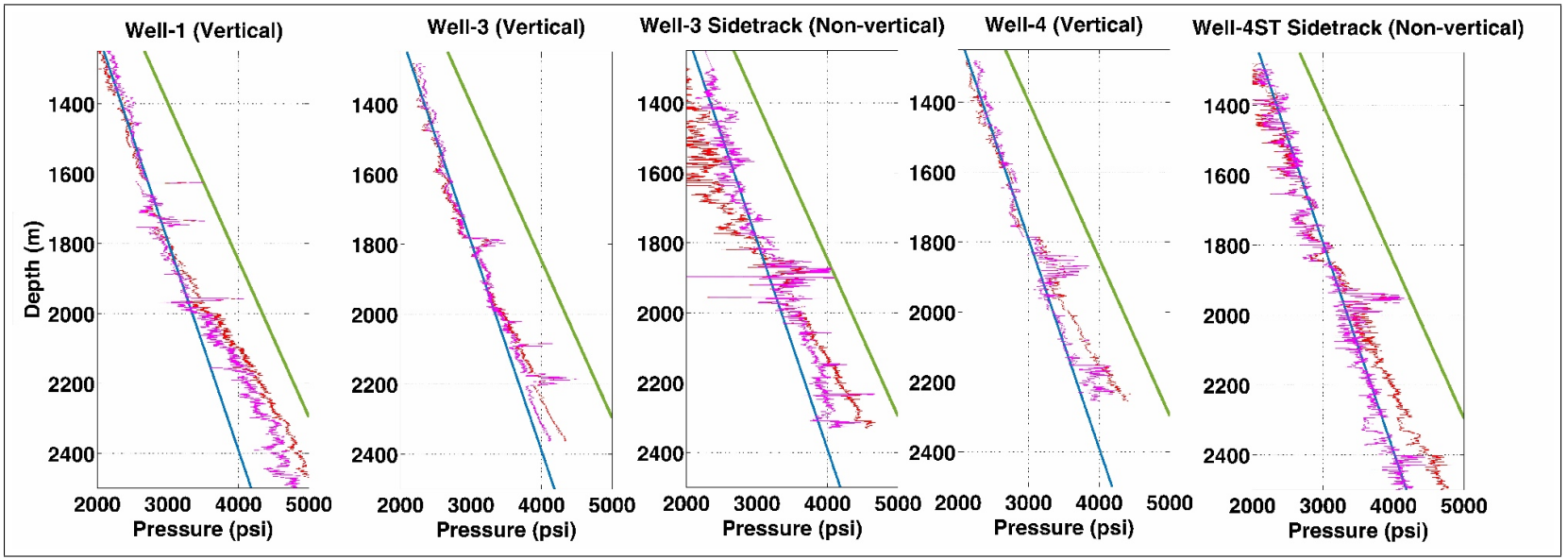

Figure A.5: Eaton's vs. Bowers's pore pressure prediction across Well-1, 3, 3ST, 4 and 4ST. Eaton's pore pressure in in red and Bowers's pore pressure is in magenta.

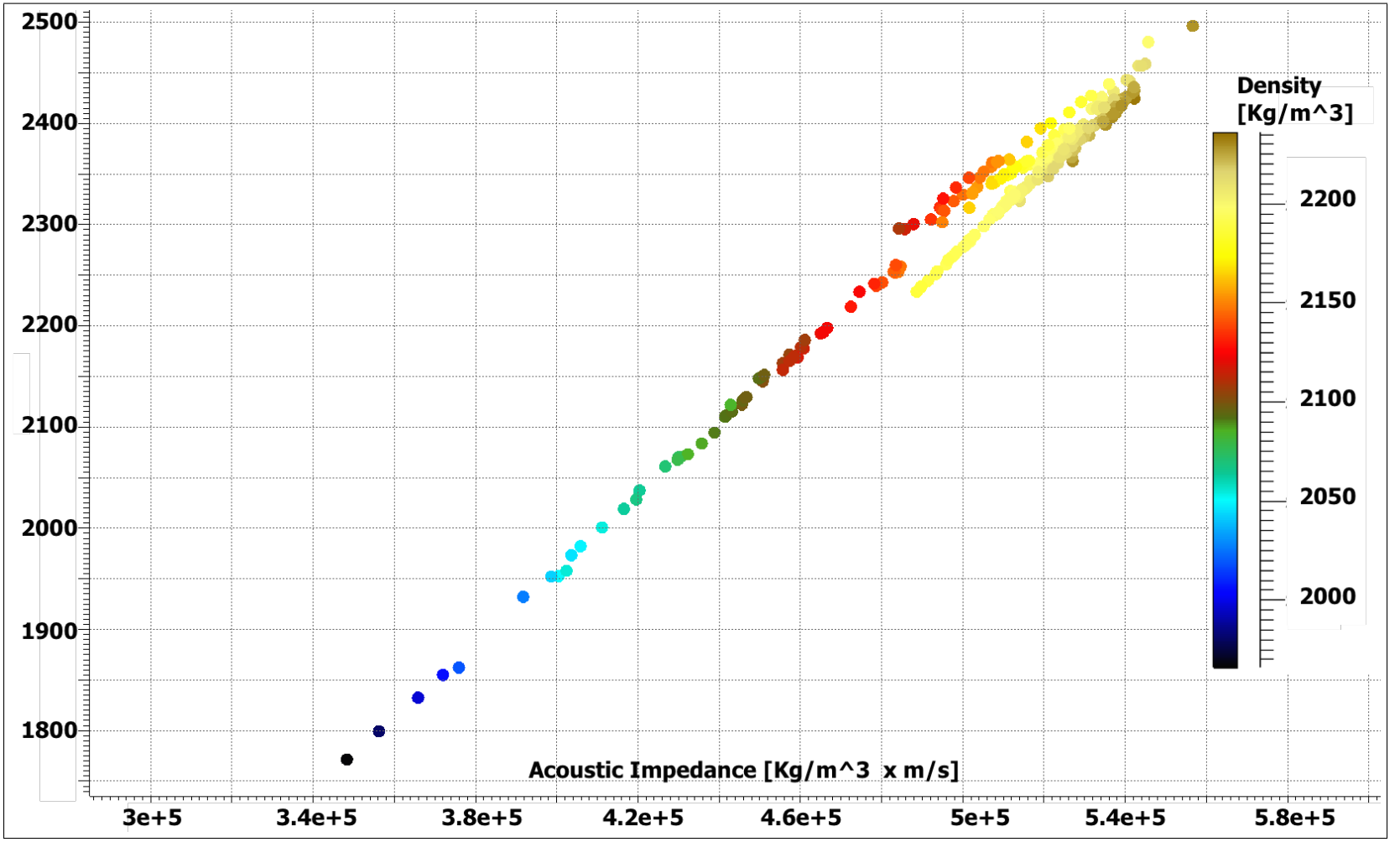

Figure A.6: Cross plot showing acoustic impedance versus compressional velocity colored by density. Density color bar shows a linear density trend. We can also segregate three layers here: low density (potentially due to hydrocarbon) medium density and highly dense material (low porosity shaley sand).

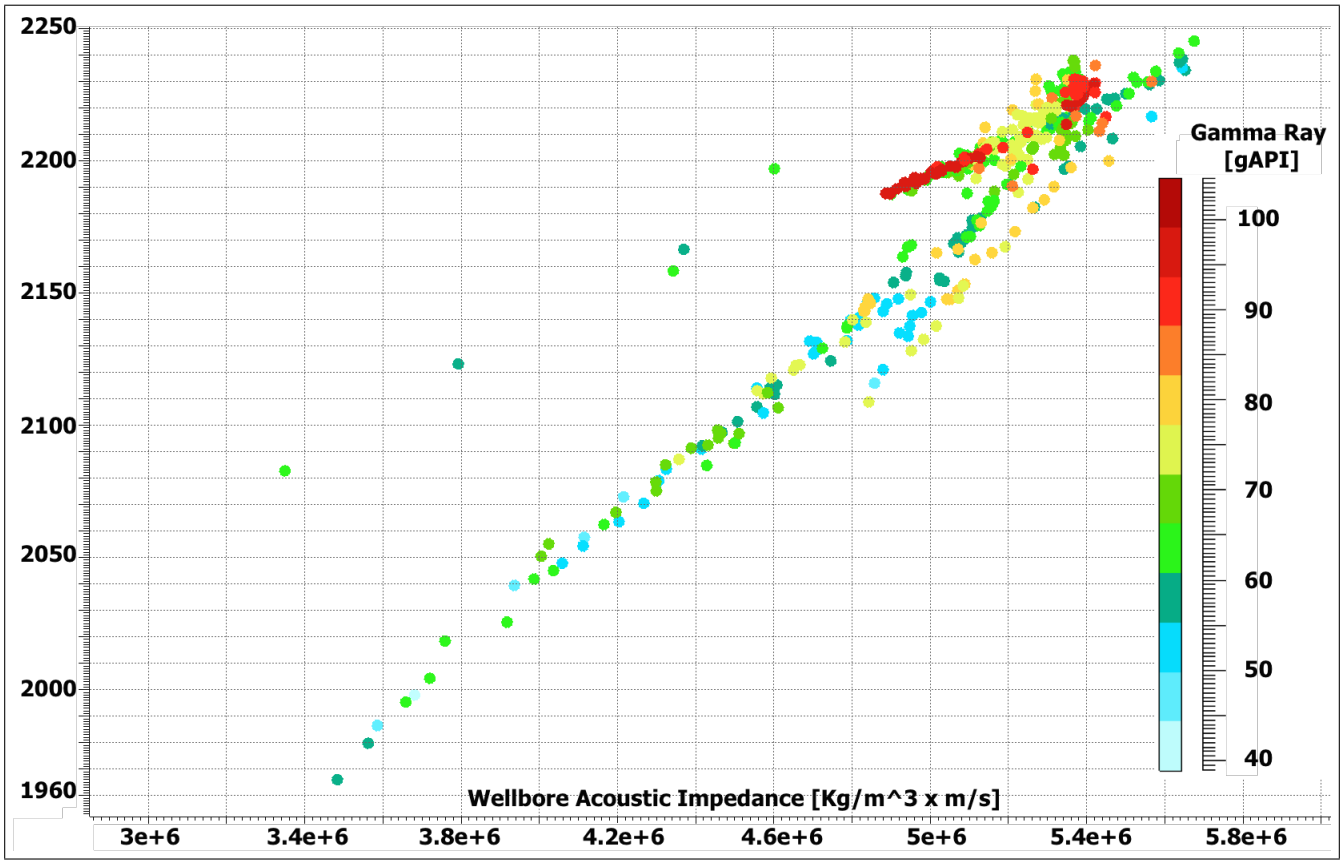

Figure A.7: Cross plot showing acoustic impedance versus density colored by gamma ray. Here, we can segregate the major three layers within our interval as the following: (1) low impedance, low gamma ray and slow velocity porous sand (reservoir), (2) medium impedance, moderate gamma ray and moderate to high velocity shaley sand, (3) high impedance, moderate to high gamma ray with high velocity shale cap

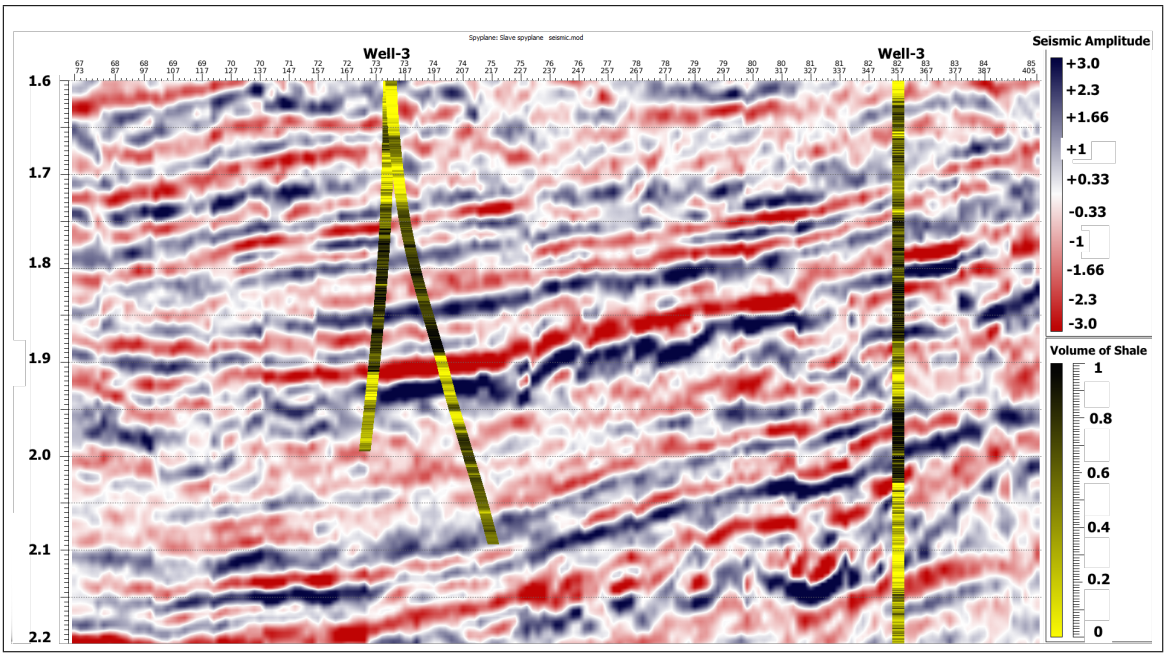

Figure A.8: 2D Seismic line. Nota bene that there is a 280 m offset between Well-1 and the seismic line and 180 m offset between the line and Well-3. GR logs are plotted with frequency cut at 80 Hz.

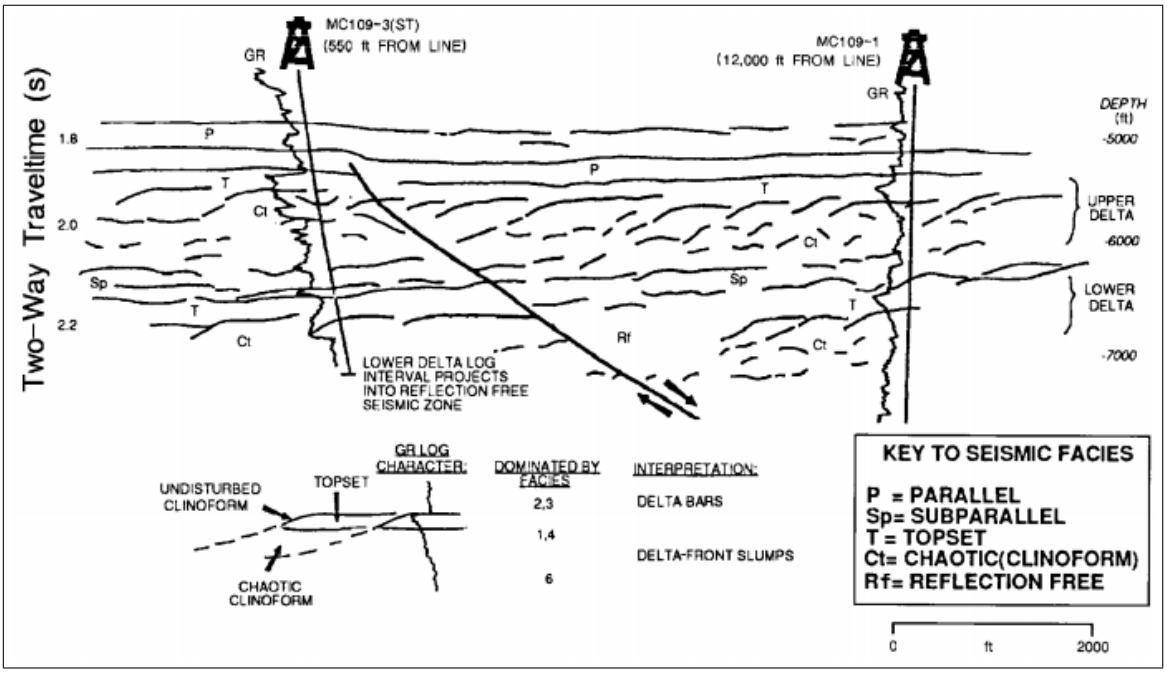

Figure A.9: Seismic facies interpretation (Mayall et al., 1992).

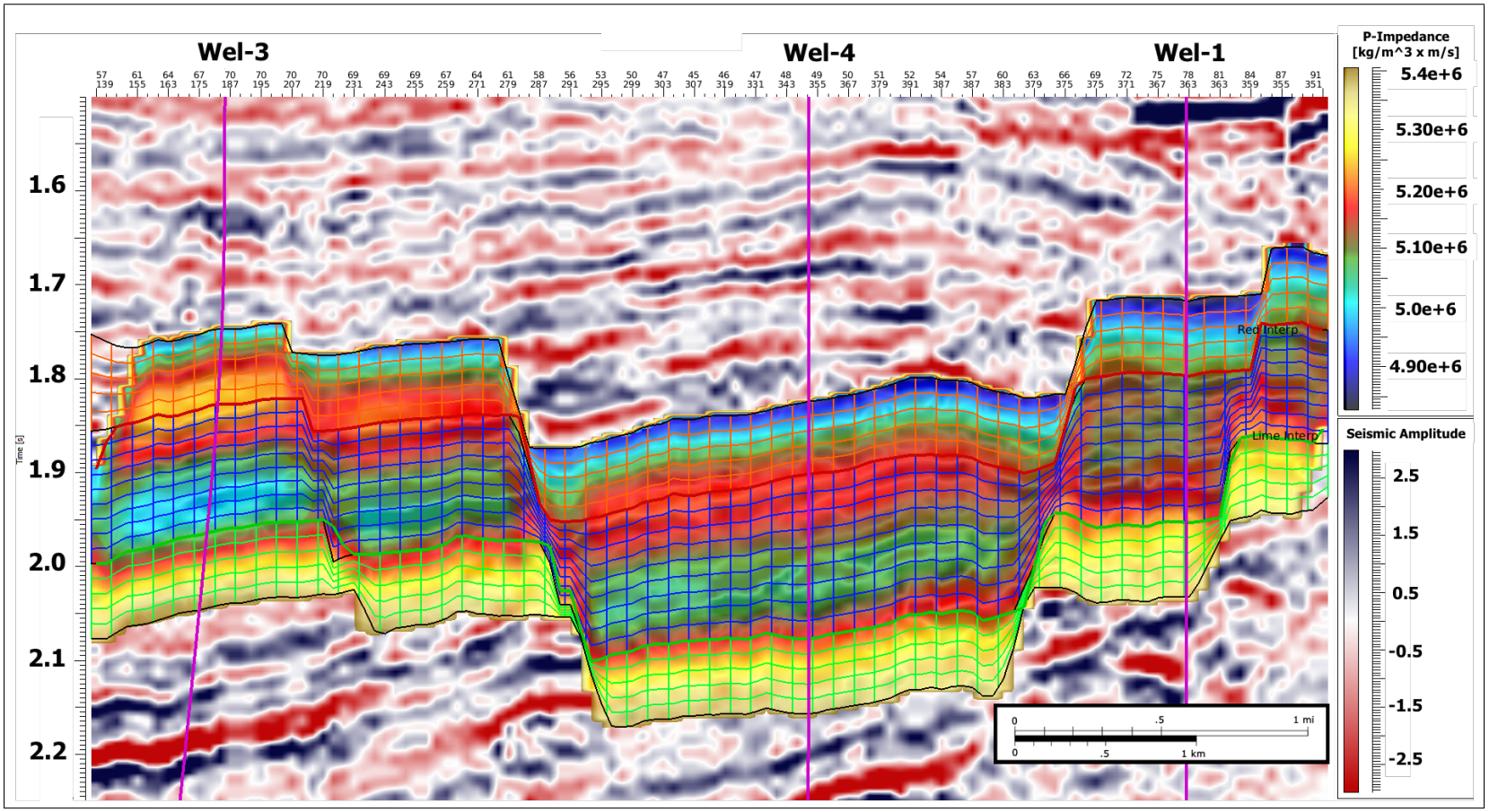

Figure A.10: Low frequency model overlaid on top of the previously defined mesh model. The low frequency is derived from the control points (vertical wells) in this case. The mesh boundary and cell shape define the extent of the filling of each cell. Hence, honor the geological observation of the subsurface

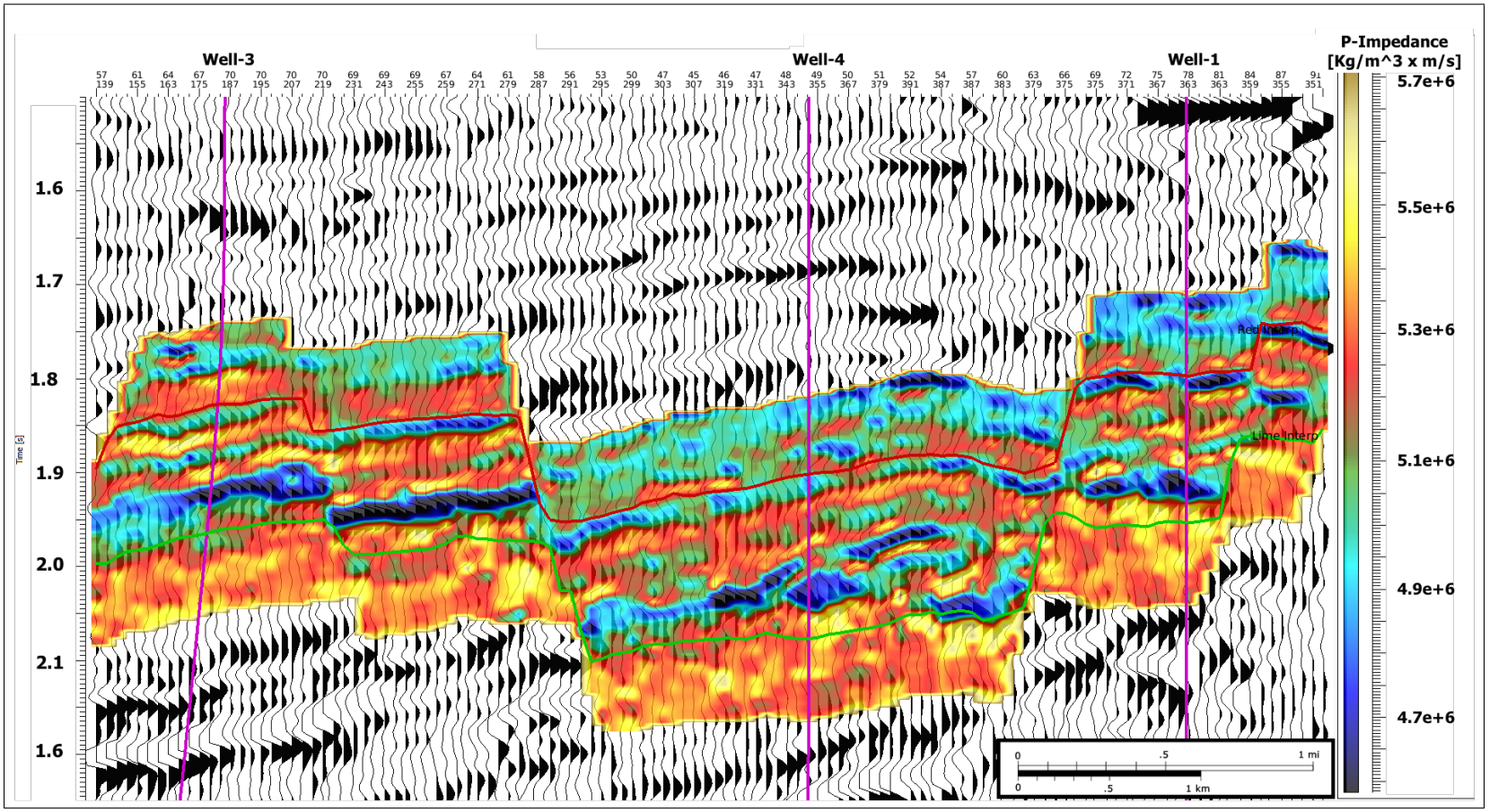

Figure A.11: Deterministic inversion results using CSSI algorithm: cross section view between Well-1, 3 and 4. Results are displayed in acoustic impedance colorbar and plotted on top of a wiggle raw seismic input to illustrate the amplitude vs. acoustic impedance correlation.

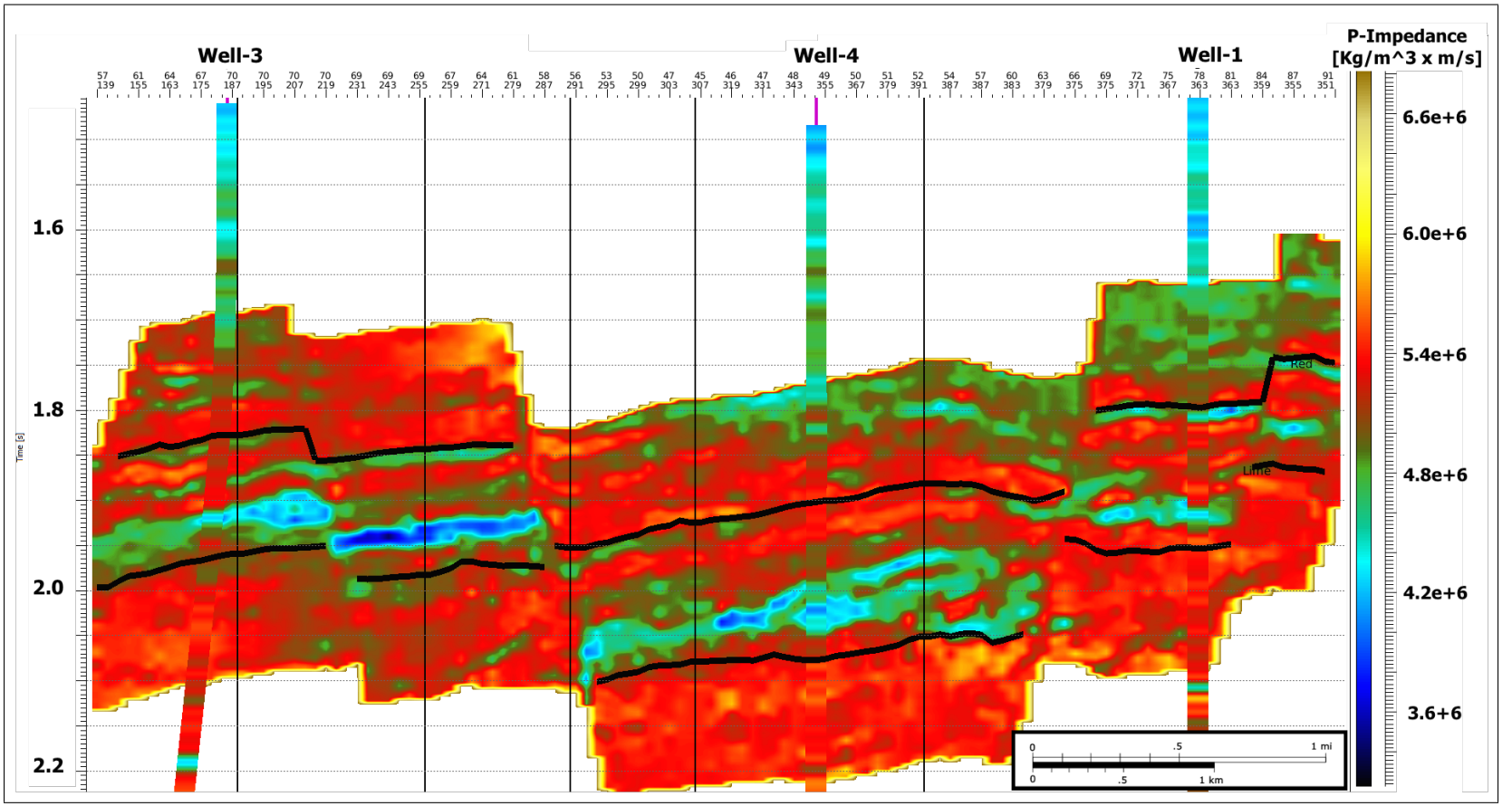

Figure A.12: Deterministic inversion results using CSSI algorithm: cross section view between Well-1, 3 and 4. Results are displayed in acoustic impedance colorbar. A 80 Hz high frequency cut filter was applied to the wellbore acoustic impedance in order to illustrate the match between the well data and the inverted acoustic impedance.

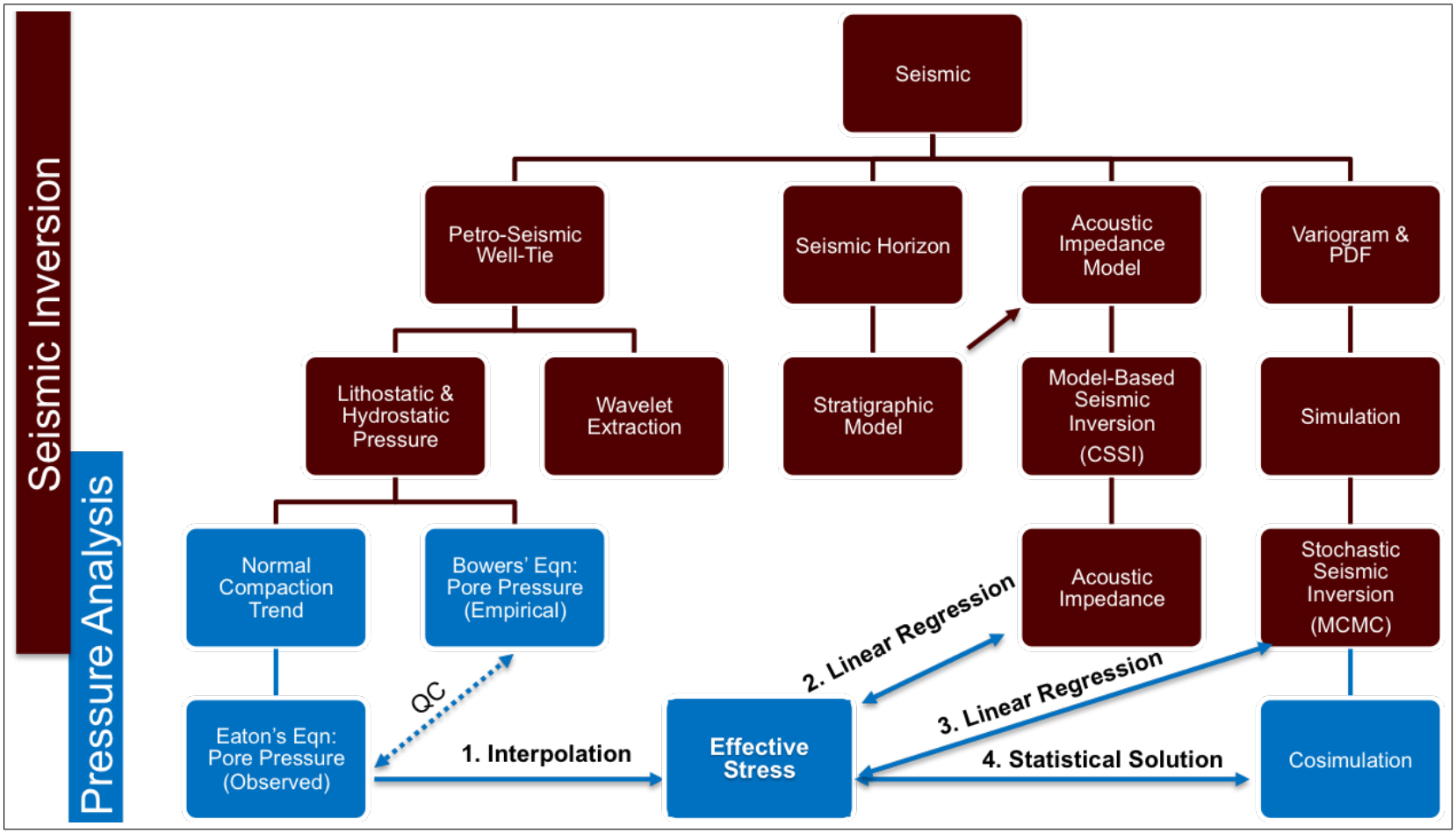

Figure A.13: Research methodology consists of two stages. First, the inversion stage which has two workflows which produce deterministic inversion based on CSSI and a stochastic inversion based on MCMC. Then, a second stage is implemented where we apply pressure analysis at the borehole using Eaton's Equation and Bowers's equation. Those analyses were extrapolated beyond the borehole using two methods: the linear regression method and the statistical cosimulation method which both transformed acoustic impedance into effective pressure.

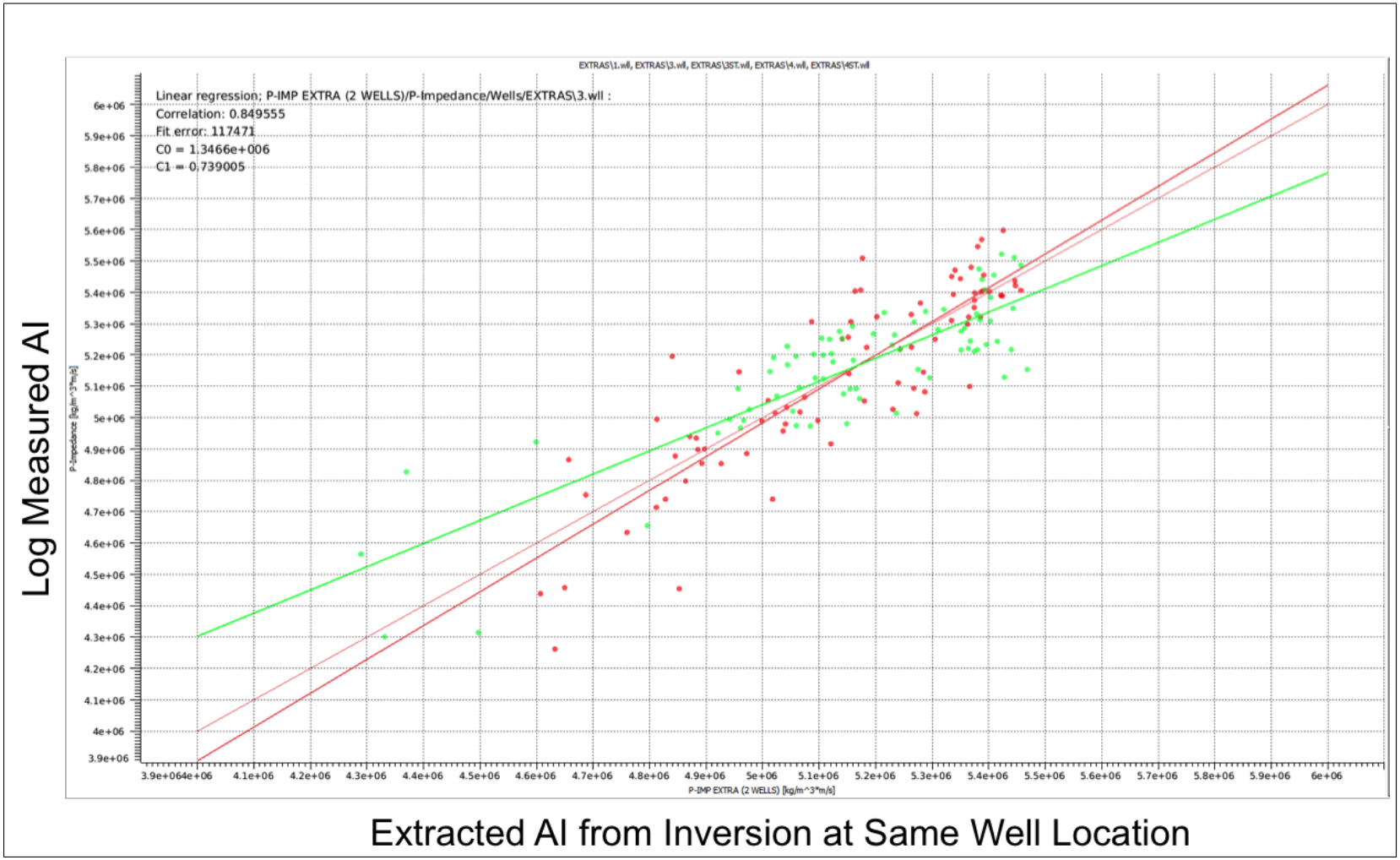

Figure A.14: Inversion quality control at well location.

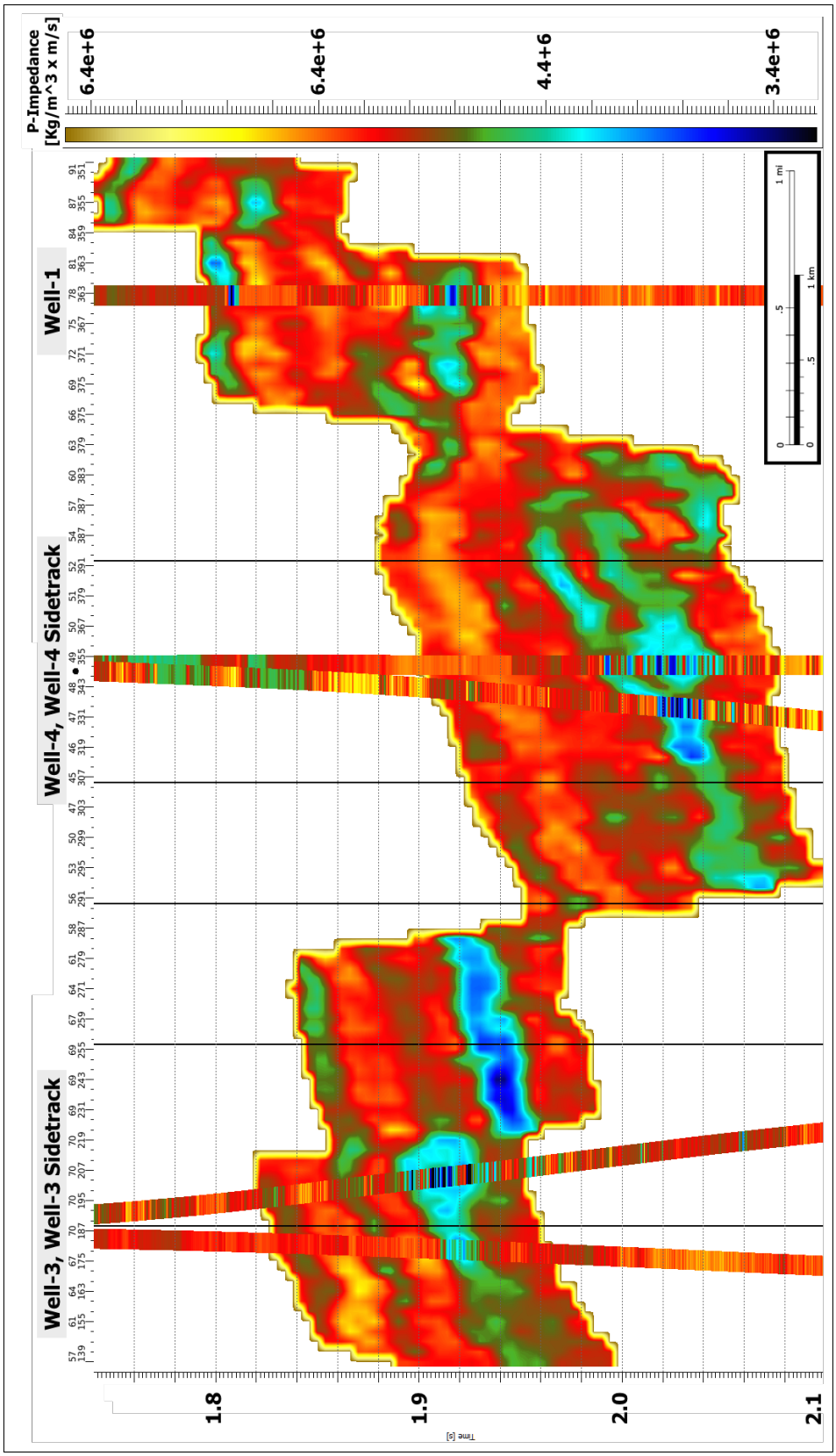

Figure A.15: Deterministic inversion final results using CSSI.

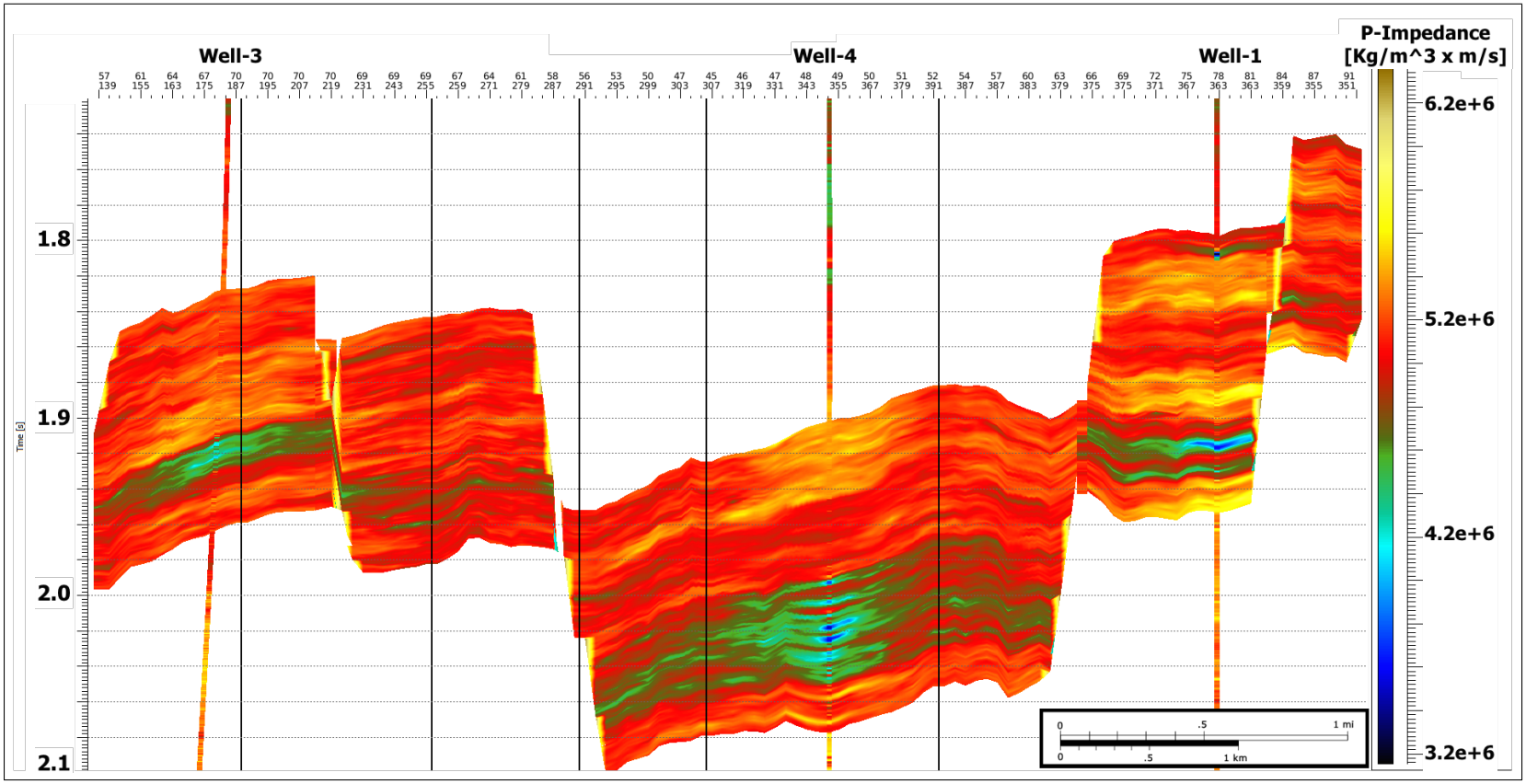

Figure A.16: Mean of 10 simulated realizations. Simulation uses well data only.

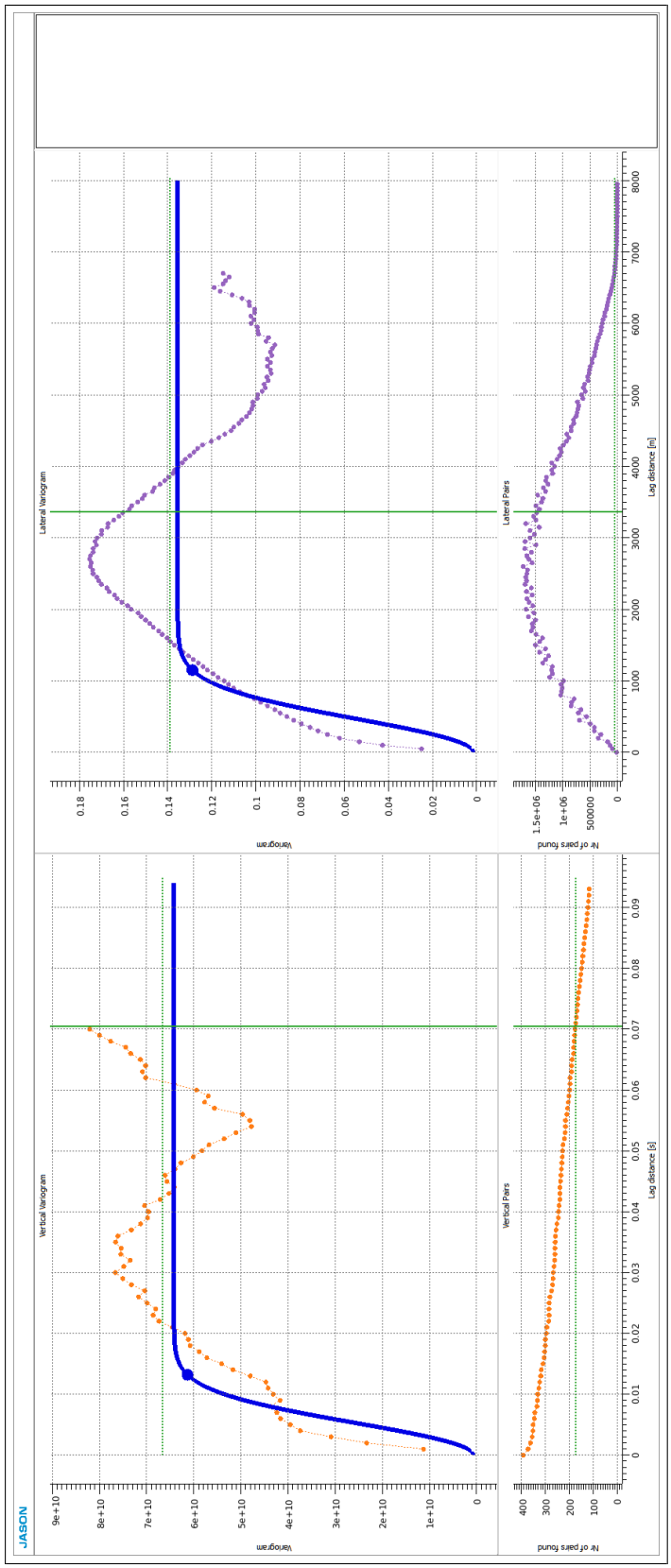

Figure A.17: A priori variogram for acoustic impedance.

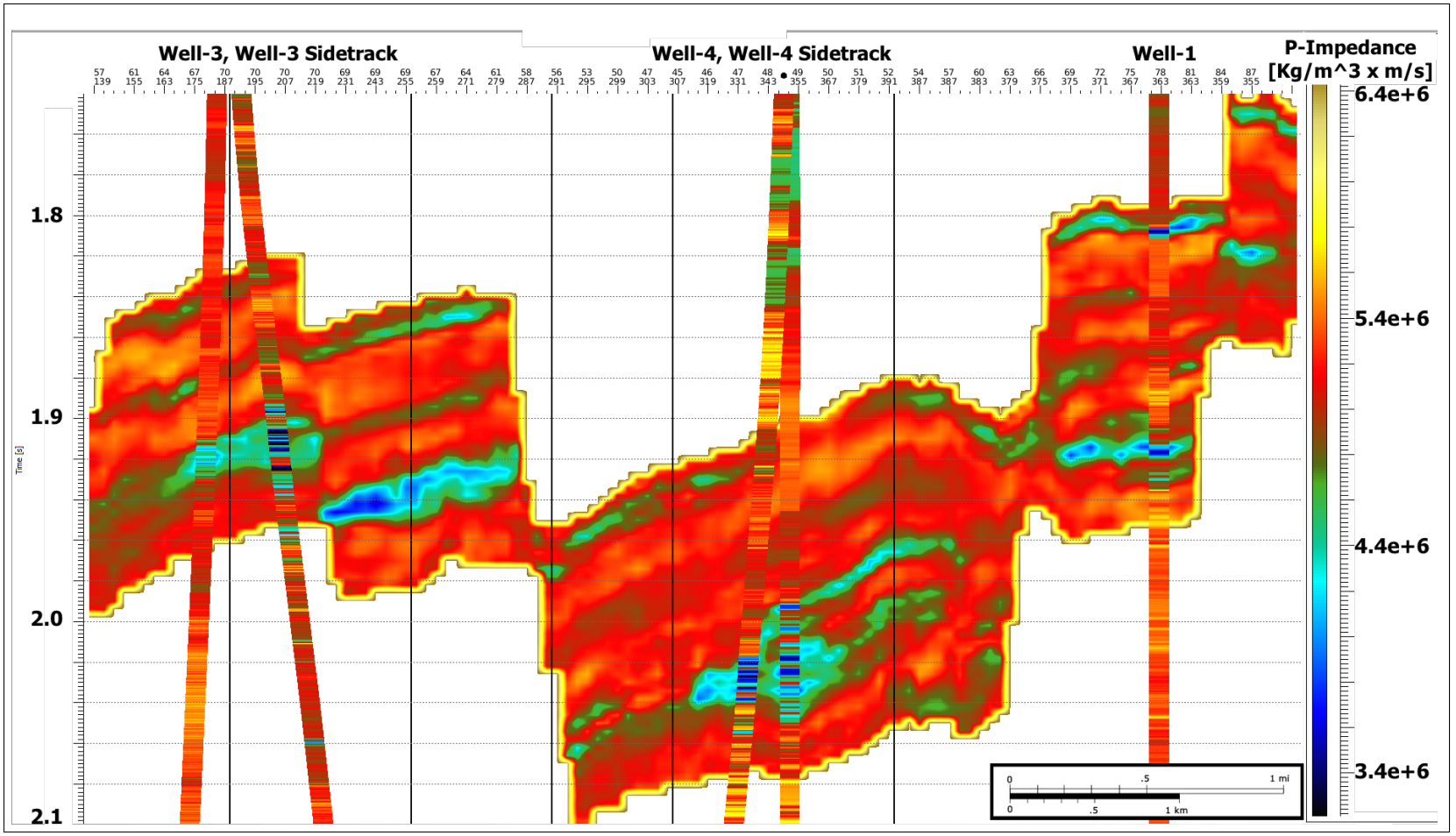

Figure A.18: Stochastic inversion final results using MCMC.

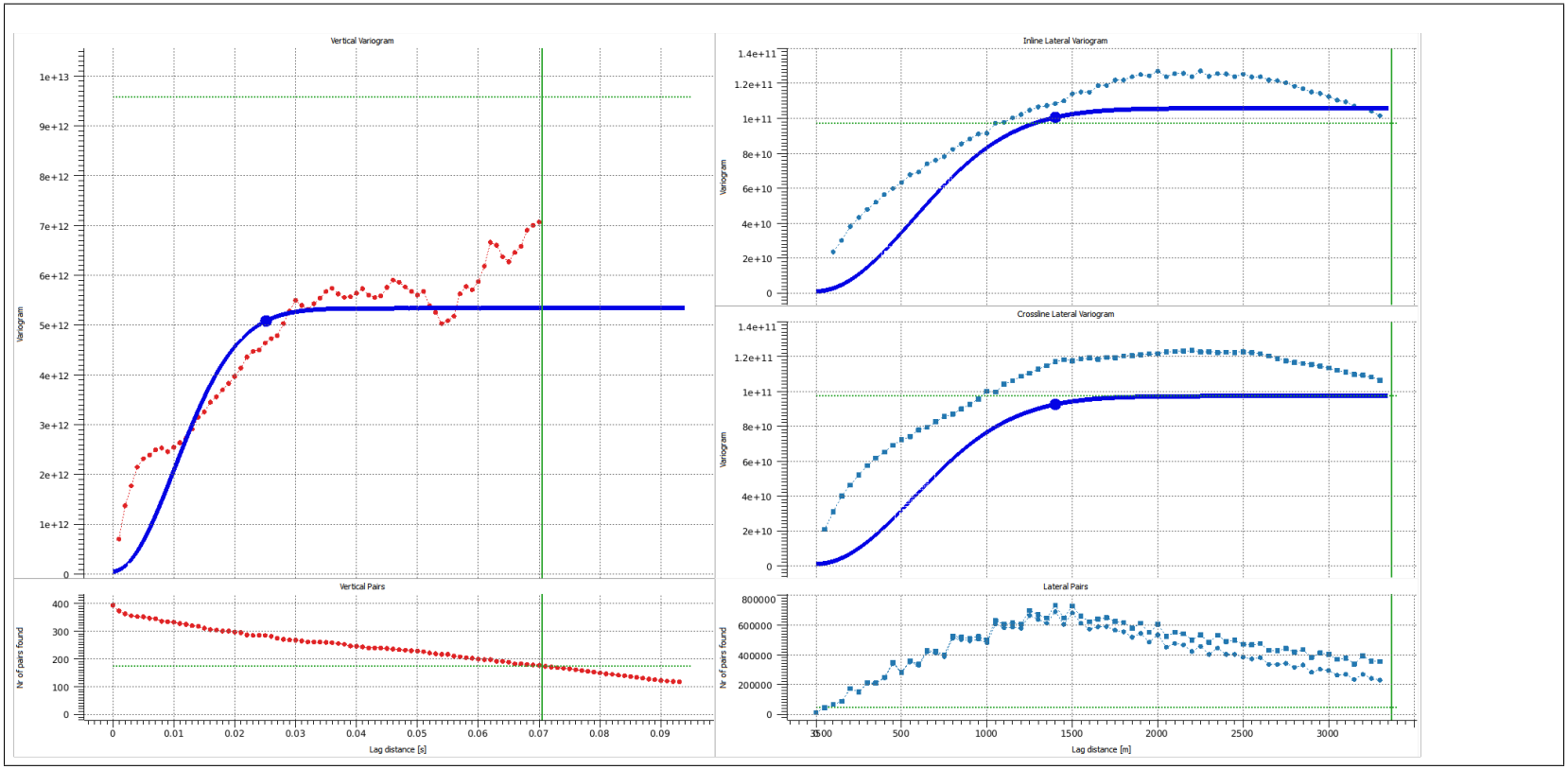

Figure A.19: Cosimulation a priori statistical model: Vertical variogram based on calculated effective pressure at the wells, inline horizontal variogram based on the previously defined effective pressure from the linear regression and cross line horizontal variogram based based on the previously defined effective pressure from the linear regression.

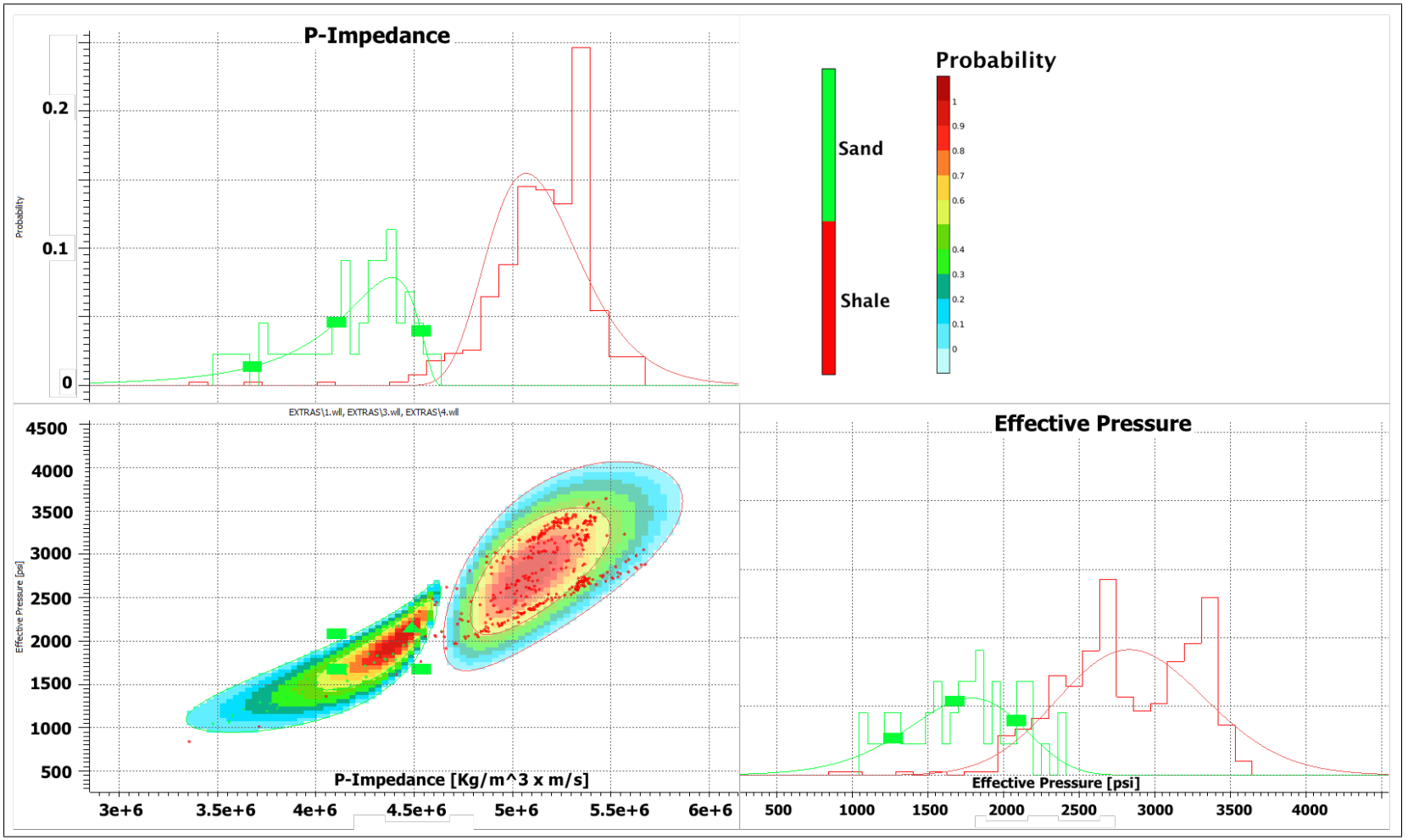

Figure A.20: Cosimulation a priori statistical model: Probability density function at the well location based on the calculated effective pressure. PDFs are segregated based on a previously defined lithology.

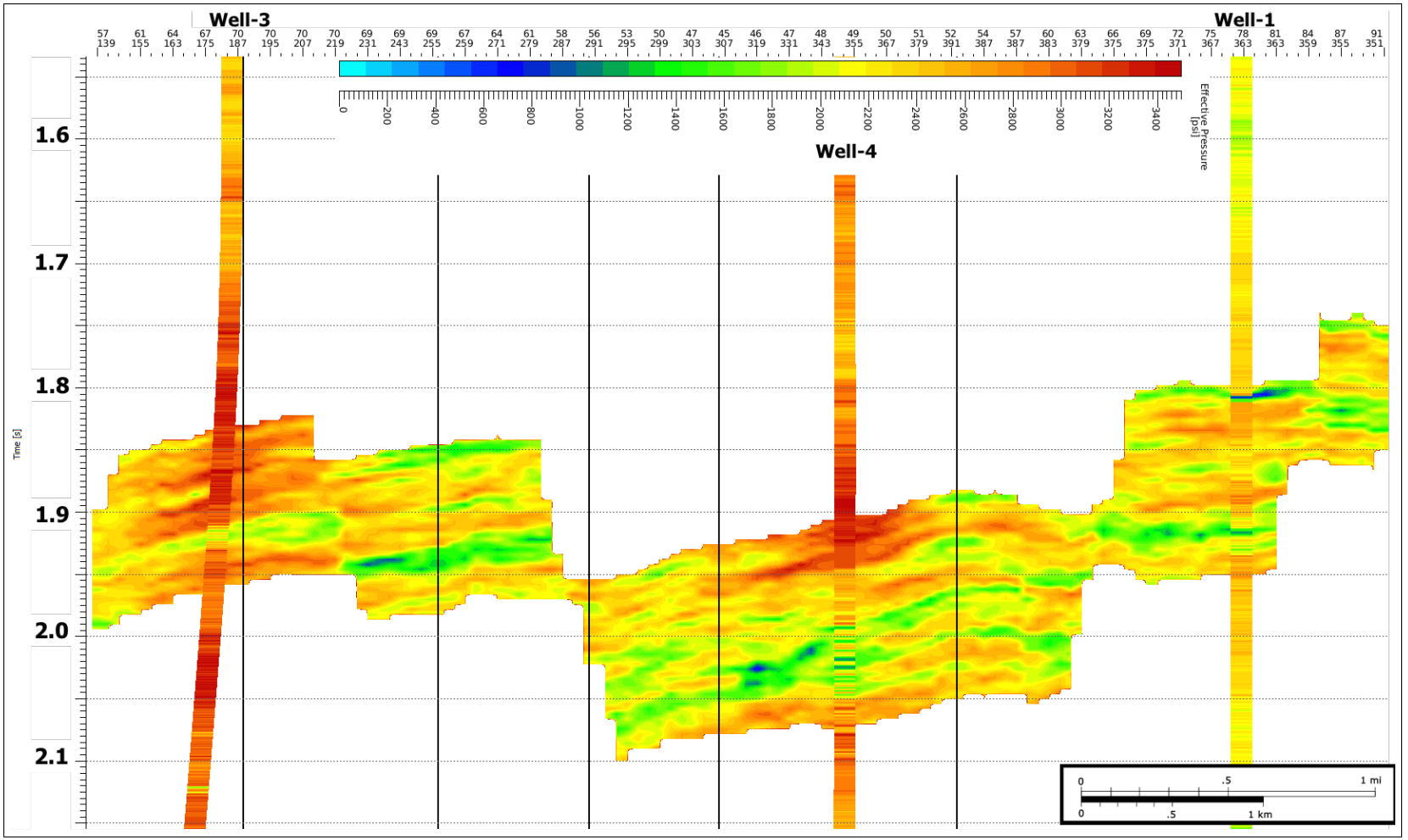

Figure A.21: Effective pressure calculated using the cosimulation approach based on the mean of the 10 realization of the geostatistically inverted acoustic impedance volume.

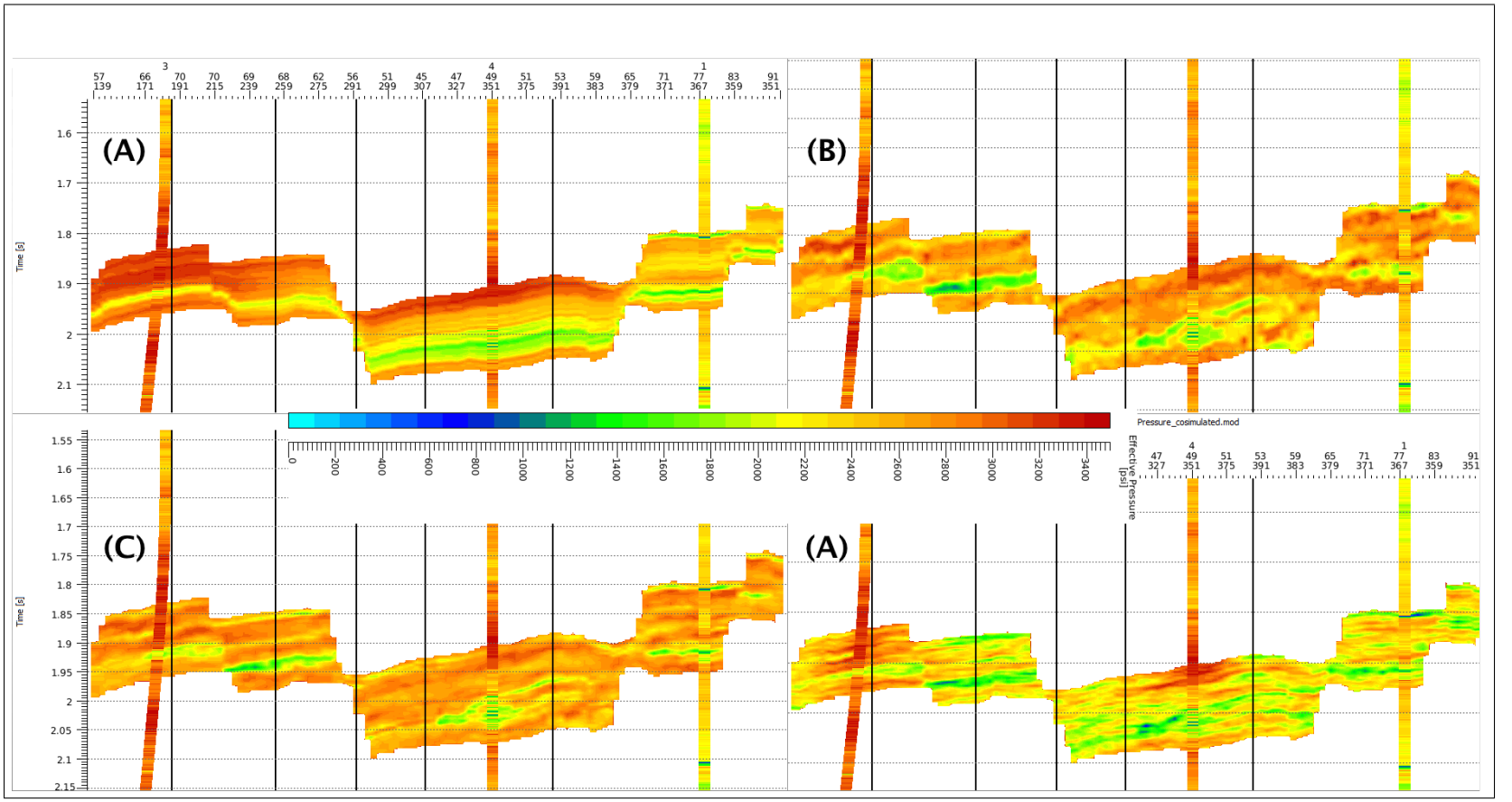

Figure A.22: Effective pressure section view through Wells-1,3 and 4 using (A) log aerial weighted interpolation, (B) linear regression tranformation (deterministic inversion), (C) linear regression transformation (geostatistical inversion) and (D) cosimulated transformation (geostatistical inversion).

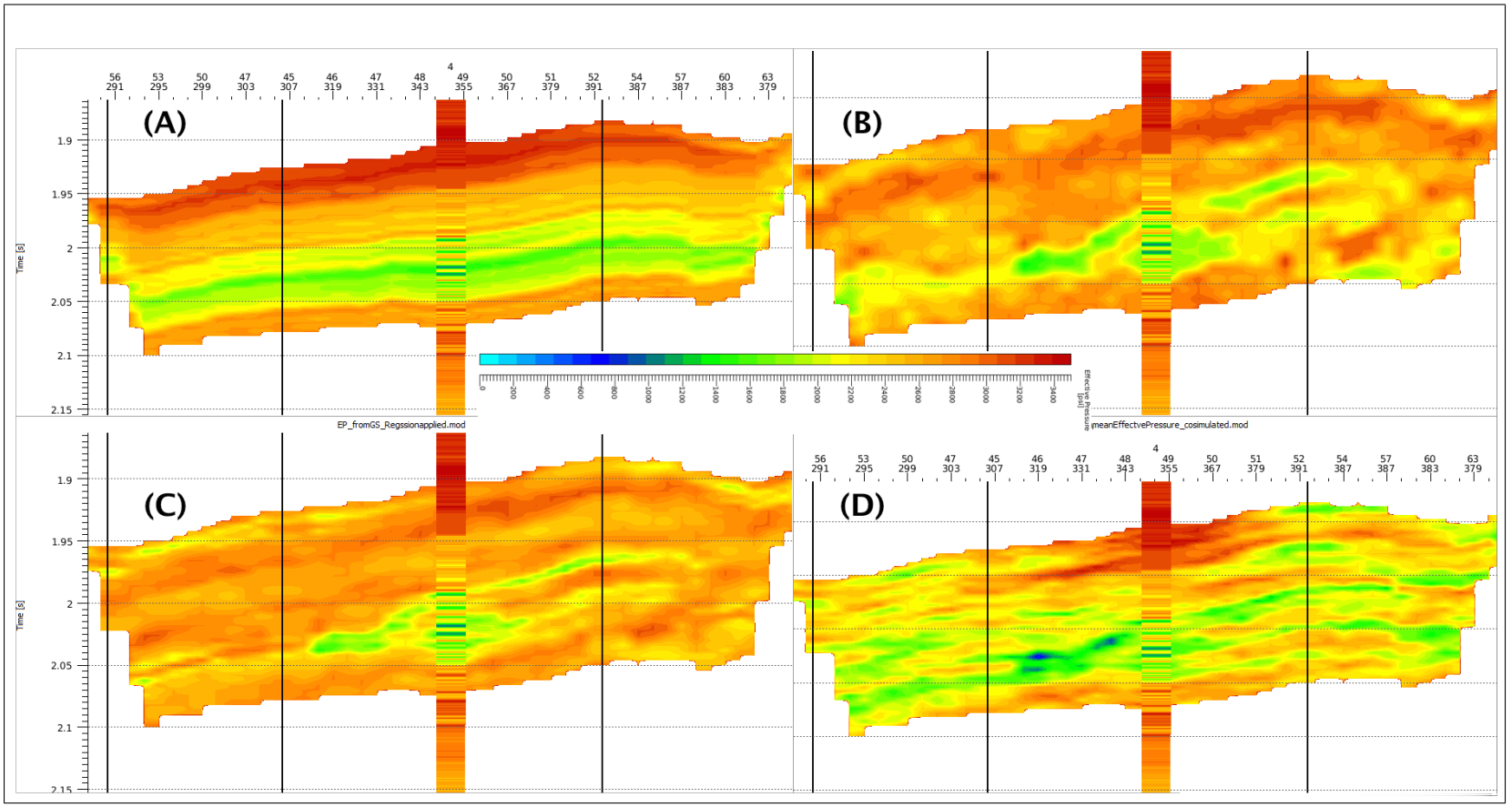

Figure A.23: Zoomed version of the effective pressure volume at Well-4 using (A) log aerial weighted interpolation, (B) linear regression tranformation (deterministic inversion), (C) linear regression transformation (geostatistical inversion) and (D) cosimulated transformation (geostatistical inversion).

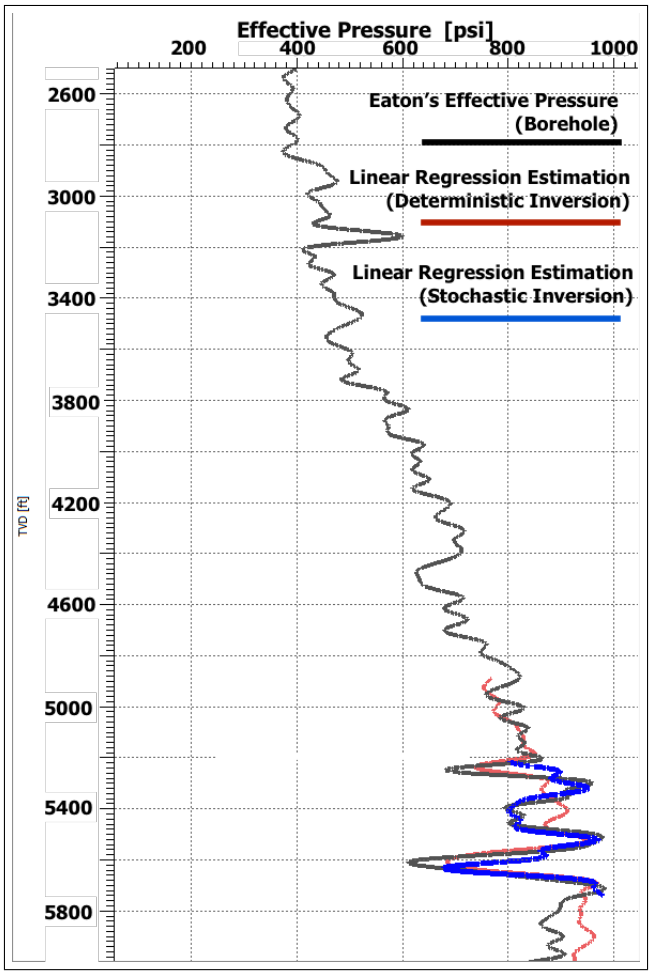

Figure A.24: Effective pressure at Well-1: Our wellbore calculated effective pressure based on our proposed method in black versus linear regression-based deterministic solution in red and linear regression-based stochastic solution in blue. Both regressions methods captured the general trend at the well location after applying the linear regression transformation from acoustic impedance to effective pressure. However, blue curve shows better correlation in comparison with the red curve.

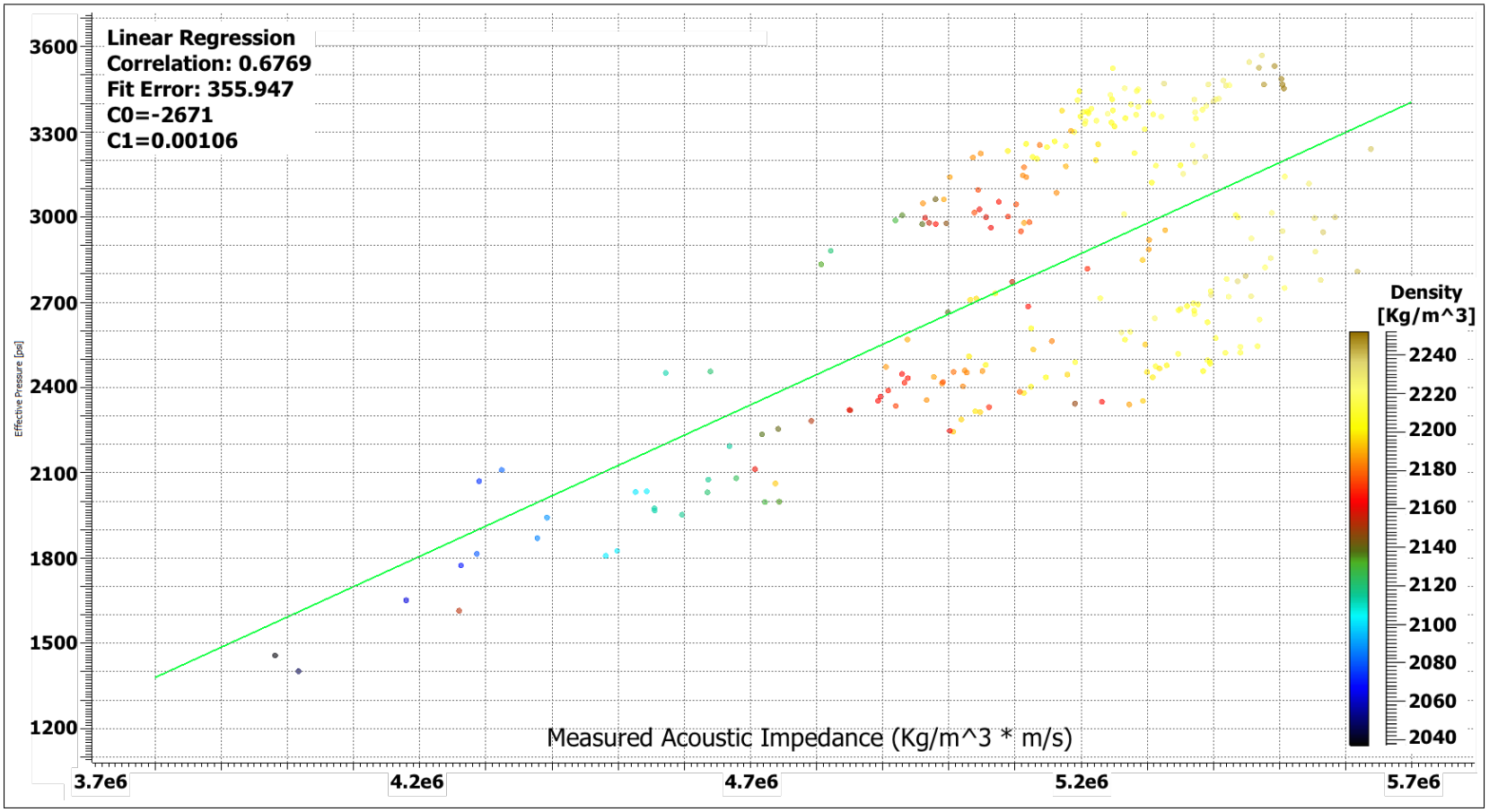

Figure A.25: The linear regression of effective pressure (psi) as a function of acoustic impedance ($kg/m^3 \times m/s$) color coded by density. Linear regression showed a 67% correlation between the two properties.

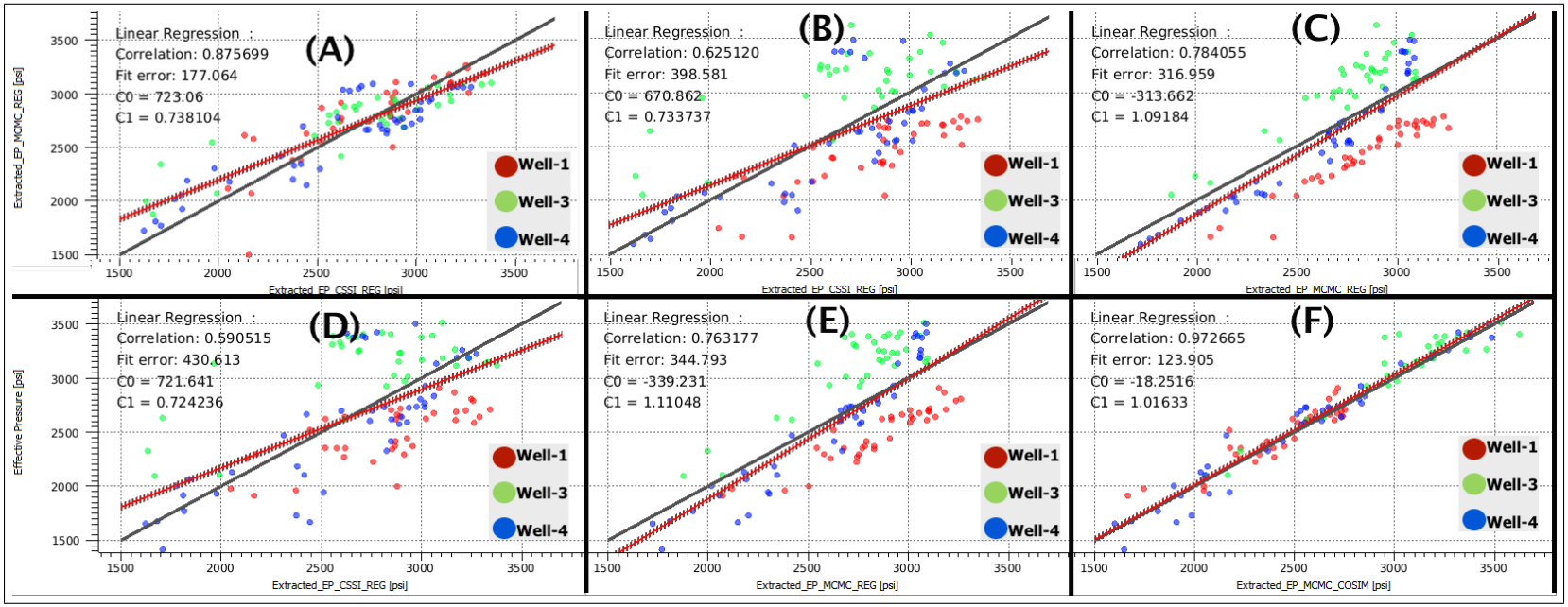

Figure A.26: Effective pressure via crossing each approach value against the calculated wellbore effective pressure and against each other to determine their correlation and reduce uncertainty. Red dotted lines represent the correlation in each cross plot, black line represents the 45 degree line and data points are colored by well number: (A) the effective pressure based on the linear regression of the stochastic solution vs. the effective pressure based on the linear regression of the deterministic solution, (B) the effective pressure based on the statistically cosimulation of the stochastic solution vs. the effective pressure based on the linear regression of the stochastic solution, (C) the effective pressure based on the statistically cosimulation of the stochastic solution vs. the effective pressure based on the linear regression of the stochastic solution, (D) wellbore calculated effective pressure vs. the effective pressure based on the linear regression of the deterministic solution, (E) wellbore calculated effective pressure vs. the effective pressure based on the linear regression of the stochastic solution, (F) wellbore calculated effective pressure vs. the effective pressure based on the statistically cosimulation of the stochastic solution.

APPENDIX B

COMPUTER CODES

The script calculates pore pressure using Bowers' equation (Bowers, 1995) and Eaton's equation (Eaton, 1969). The script generates different plots and quality control the results by crossplotting the two methods against each other to show their deviation from the 45-degree line. This script imports ascii file into MATLAB; it is not designed to import LAS files. The imported data file must be sorted in depth (ft), Compressional velocity (m/s), density (kg/cc) and interpreted normal compaction trend velocity (m/s)

B.1 Pore Pressure Prediction at the Borehole: MATLAB Script

```
1
2  %% (0) Import data from text file.
3  filename = '/Users/Haider/Documents/MATLAB/well1_v2.txt';
4  delimiter = '\t';
5  startRow = 2;
6  % Format string for each line of text:
7  formatSpec = '%f%f%f%f%[^\n\r]';
8  % Open the text file.
9  fileID = fopen(filename,'r');
10
11 %% Read inputfile
12 dataArray = textscan(fileID, formatSpec, 'Delimiter',
       delimiter, 'EmptyValue' ,0.0,'HeaderLines' ,startRow-1, '
```

```
    ReturnOnError', false);
13
14 % Close the text file.
15 fclose(fileID);
16
17 %% Read pre-defined column and assign them to data type;
    could be change
18 % user has a different order.
19 depth = dataArray{:, 1};
20 vp = dataArray{:, 2};
21 density = dataArray{:, 3};
22 VpNCT = dataArray{:, 4};
23
24 % Clear temporary variables
25 clearvars filename delimiter startRow formatSpec fileID
    dataArray ans;
26 ------------------------------------------------------------
27 (1) Calculating Hydrostatic pressure (HSP). Unit: PSI
28 promote user to enter pressure pressure gradient
29 p_grad = input('What is your hydrostatic pressure gradient
    in PSI (ex. GOM=0.49)? ');
30 p_grad = 0.49;
31 calculate HSP at each depth point
32 for j=1 : length(depth)
33     hsp(j)= depth(j) .* p_grad;
```

```
34 end
35 hsp=hsp.';                % transpote vector for consistency
36 ------------------------------------------------------------------
37 (2) Calculating Lithostatic pressure (LSP). Unit: PSI
38 gravity= 9.8;% gravitational consant
39 pa2psi=0.000145037;% conversion factor from Pa to PSI
40 lsp_wellhead=###% pressure at wellhead
41 seafloor=162;% array containing the depth of seafloor
42
43 for j=2 : seafloor% Calculate lithostatic pressure of water
      column
44     lsp(j)= ((depth(j)./3.048) .* density(j) .* gravity .*
          pa2psi);
45 end
46
47 for j=seafloor+1 : length(depth)% Calculate lithostatic
      pressure of lithology from seafloor to bottom
48     lsp(j)= ((depth(j)./3.048) .* density(j) .* gravity .*
          pa2psi)+lsp(seafloor);
49 end
50
51 lsp=lsp.'; % transpote vector for consistency
52 % ------------------------------------------------------------------
53
```

```
54 % (3) Calculating a user-defined normal compaction trend fit
       . Unit: m/s
55
56 for j=1 : length(depth) % Calculate Bowers' from seafloor
57     VpNCT(j)=1/((4100-(depth(j)./3.048))./6000000);
58 end
59 % ---------------------------------------------------------
60
61 % (4) Calculating Bowers' Pore pressure (BPP). Unit: PSI
62
63 seawater_velocity=5000;% sea water velocity (ft/s)
64 cca_bowers=9.18448;% Bowers's calibration coefficent
65 ccb_bowers=0.764984;% Bowers's calibration coefficent
66 %cca_bowers=6;% Bowers's calibration coefficent
67 %ccb_bowers=0.7;% Bowers's calibration coefficen
68
69 for j=seafloor+1 : length(depth) % Calculate Bowers' from
       seafloor
70     bpp(j)= -power(((vp(j) .* 3.048 - 5000)./cca_bowers), 1/
           ccb_bowers)+lsp(j);
71 end
72
73 % ---------------------------------------------------------
74 % (5) Calculating Eaton's Pore pressure (EPP). Unit: PSI
```

```
75 for j=seafloor+1 : length(depth) % Calculate Bowers' from
   seafloor
76     epp(j)= -( (lsp(j)-hsp(j)) .* power( (vp(j)./VpNCT(j))
          ,3))+ lsp(j);
77 end
78
79 %-------------------------------------------------------------
80 % (6) Plots
81 %   I.  Figure-1: Curves are plotted in depth domain. Plot
   Vp,
82 %   VpNCT, Density, Bowers' and Eaton's pore pressure bounded
    by lithostatic
83 %   and hydrostatic pressure using figure1 script pre-
   defined by user.
84     figure1(vp, depth, VpNCT, density, hsp, lsp, bpp, epp)
85
86 %   II. Figure-2: Crossplot of Bowers' pore pressure vs.
   Eaton's pore
87 %   pressure to infer correlation between them.
88     for j=1 : length(depth) % 45-degree line (display)
89         yy(j)=j;
90         xx(j)=j;
91     end
92     figure2(epp,bpp,vp,yy,xx)
```

[Listing-1: MATLAB Scripts to load data and calculate pressures using Eaton's and

Bower's Pore pressure. N.B. that codes are partially auto generated by MATLAB R2014a]

Listing B.1: Matlab script to generate a standard depth curves for the petrophysical logs

```
function createfigure1(vp, depth, VpNCT, density, hsp, lsp,
    bpp, epp)
%CREATEFIGURE1(VP1, DEPTH1, VPNCT1, DENSITY1, HSP1, LSP1,
    BPP1, EPP1)
%  VP1:  vector of x data
%  DEPTH1:  vector of y data
%  VPNCT1:  vector of x data
%  DENSITY1:  vector of x data
%  HSP1:  vector of x data
%  LSP1:  vector of x data
%  BPP1:  vector of x data
%  EPP1:  vector of x data

%  Auto-generated by MATLAB on 05-Dec-2015 17:20:27

% Create figure
figure1 = figure;

% Create subplot
subplot1 = subplot(1,4,1,'Parent',figure1,'YGrid','on','YDir
    ','reverse',...
     'XGrid','on');
```

```
20 xlim(subplot1,[1500 3000]);
21 ylim(subplot1,[0 11500]);
22 box(subplot1,'on');
23 hold(subplot1,'all');
24
25 % Create plot
26 plot(vp,depth,'Parent',subplot1);
27
28 % Create xlabel
29 xlabel('Compressional Velocity (m/s)');
30
31 % Create ylabel
32 ylabel('Depth (ft)');
33
34 % Create plot
35 plot(VpNCT,depth,'Parent',subplot1,'DisplayName','depth vs
      VpNCT');
36
37 % Create subplot
38 subplot2 = subplot(1,4,2,'Parent',figure1,'YGrid','on','YDir
      ','reverse',...
39       'XGrid','on');
40 xlim(subplot2,[1900 2300]);
41 ylim(subplot2,[0 11500]);
42 box(subplot2,'on');
```

```
43 hold(subplot2,'all');
44
45 % Create xlabel
46 xlabel('Density (Kg/cc)');
47
48 % Create plot
49 plot(density,depth,'Parent',subplot2,'DisplayName','depth vs
       density');
50
51 % Create subplot
52 subplot3 = subplot(1,4,3,'Parent',figure1,'YGrid','on','YDir
       ','reverse',...
53     'XGrid','on');
54  xlim(subplot3,[0 12000]);
55 ylim(subplot3,[0 11500]);
56 box(subplot3,'on');
57 hold(subplot3,'all');
58
59 % Create xlabel
60 xlabel('Bowers'' Eqn Pore Pressure');
61
62 % Create plot
63 plot(hsp,depth,'Parent',subplot3,'DisplayName','depth vs hsp
       ');
64
```

```
65 % Create plot
66 plot(lsp,depth,'Parent',subplot3,'DisplayName','depth vs lsp
       ');
67
68 % Create plot
69 plot(bpp,depth,'Parent',subplot3,'DisplayName','depth vs bpp
       ');
70
71 % Create subplot
72 subplot4 = subplot(1,4,4,'Parent',figure1,'YGrid','on','YDir
       ','reverse',...
73     'XGrid','on');
74 xlim(subplot4,[0 12000]);
75 ylim(subplot4,[0 11500]);
76 box(subplot4,'on');
77 hold(subplot4,'all');
78
79 % Create xlabel
80 xlabel('Eaton''s Eqn Pore Pressure');
81
82 % Create plot
83 plot(epp,depth,'Parent',subplot4,'DisplayName','depth vs epp
       ');
84
85 % Create plot
```

```
86 plot(lsp,depth,'Parent',subplot4,'DisplayName','depth vs lsp
       ');
87
88 % Create plot
89 plot(hsp,depth,'Parent',subplot4,'DisplayName','depth vs hsp
       ');
```

Listing B.2: Matlab script to generate a crossplot of Eaton's vs. Bowers' pore pressure along with their linear regression fit function and the 45-degree line for comparison

```
function createfigure1(epp, bpp, vp, yy, xx)
%CREATEFIGURE1(X1, Y1, S1, VP1, XX1)
%  X1:  scatter x
%  Y1:  scatter y
%  S1:  scatter s
%  VP1:  scatter c
%  XX1:  vector of x data

%  Auto-generated by MATLAB on 06-Dec-2015 00:36:37

% Create figure
figure1 = figure;

% Create axes
axes1 = axes('Parent',figure1,'YGrid','on','XGrid','on');

ylim(axes1,[0 14000]);
box(axes1,'on');
hold(axes1,'all');

% Create scatter
scatter1 = scatter(epp,bpp,30, vp,'Parent',axes1,'
    DisplayName','Velocity (m/s)');
```

```
23
24 % Create xlabel
25 xlabel('Eaton''s Eqn Pore Pressure (psi)','FontWeight','bold
       ','FontSize',16);
26
27 % Create ylabel
28 ylabel('Bowers'' Eqn Pore Pressure (psi)','FontWeight','bold
       ','FontSize',16);
29
30 % Create plot
31 plot(xx,xx,'Parent',axes1,'DisplayName','45 Degree line');
32
33 % Get xdata from plot
34 xdata1 = get(scatter1, 'xdata');
35 % Get ydata from plot
36 ydata1 = get(scatter1, 'ydata');
37 % Make sure data are column vectors
38 xdata1 = xdata1(:);
39 ydata1 = ydata1(:);
40
41
42 % Remove NaN values and warn
43 nanMask1 = isnan(xdata1(:)) | isnan(ydata1(:));
44 if any(nanMask1)
45     warning('GeneratedCode:IgnoringNaNs', ...
```

```
46          'Data points with NaN coordinates will be ignored.')
                ;
47      xdata1(nanMask1) = [];
48      ydata1(nanMask1) = [];
49  end
50
51  % Find x values for plotting the fit based on xlim
52  axesLimits1 = xlim(axes1);
53  xplot1 = linspace(axesLimits1(1), axesLimits1(2));
54
55  % Preallocate for "Show equations" coefficients
56  coeffs1 = cell(1,1);
57
58
59  fitResults1 = polyfit(xdata1, ydata1, 1);
60  % Evaluate polynomial
61  yplot1 = polyval(fitResults1, xplot1);
62
63  % Save type of fit for "Show equations"
64  fittypesArray1(1) = 2;
65
66  % Save coefficients for "Show Equation"
67  coeffs1{1} = fitResults1;
68
69  % Plot the fit
```

```
70 fitLine1 = plot(xplot1,yplot1,'DisplayName','    linear','
   Parent',axes1,...
71     'Tag','linear',...
72     'Color',[1 0 0]);
73
74 % Set new line in proper position
75 setLineOrder(axes1, fitLine1, scatter1);
76
77 % "Show equations" was selected
78 showEquations(fittypesArray1, coeffs1, 2, axes1);
79
80 % Create colorbar
81 colorbar('peer',axes1);
82
83 % Create legend
84 legend1 = legend(axes1,'show');
85 set(legend1,...
86     'Position',[0.684135990010953 0.15468888052431
         0.104769175498473 0.115456322515554],...
87     'FontSize',14);
88
89 %-------------------------------------------------------------%
90 function setLineOrder(axesh1, newLine1, associatedLine1)
91 %SETLINEORDER(AXESH1,NEWLINE1,ASSOCIATEDLINE1)
92 %  Set line order
```

```
93  %  AXESH1:  axes
94  %  NEWLINE1:  new line
95  %  ASSOCIATEDLINE1:  associated line
96
97  % Get the axes children
98  hChildren = get(axesh1,'Children');
99  % Remove the new line
100 hChildren(hChildren==newLine1) = [];
101 % Get the index to the associatedLine
102 lineIndex = find(hChildren==associatedLine1);
103 % Reorder lines so the new line appears with associated data
104 hNewChildren = [hChildren(1:lineIndex-1);newLine1;hChildren(
        lineIndex:end)];
105 % Set the children:
106 set(axesh1,'Children',hNewChildren);
107
108 %------------------------------------------------------------%
109 function showEquations(fittypes1, coeffs1, digits1, axesh1)
110 %SHOWEQUATIONS(FITTYPES1,COEFFS1,DIGITS1,AXESH1)
111 %  Show equations
112 %  FITTYPES1:  types of fits
113 %  COEFFS1:  coefficients
114 %  DIGITS1:  number of significant digits
115 %  AXESH1:  axes
116
```

```
117 n = length(fittypes1);
118 txt = cell(length(n + 1) ,1);
119 txt{1,:} = ' ';
120 for i = 1:n
121     txt{i + 1,:} = getEquationString(fittypes1(i),coeffs1{i
        },digits1,axesh1);
122 end
123 text(.05,.95,txt,'parent',axesh1, ...
124     'verticalalignment','top','units','normalized');
125
126 %-------------------------------------------------------------------------%
127 function [s1] = getEquationString(fittype1, coeffs1, digits1
    , axesh1)
128 %GETEQUATIONSTRING(FITTYPE1,COEFFS1,DIGITS1,AXESH1)
129 %  Get show equation string
130 %  FITTYPE1:  type of fit
131 %  COEFFS1:  coefficients
132 %  DIGITS1:  number of significant digits
133 %  AXESH1:  axes
134
135 if isequal(fittype1, 0)
136     s1 = 'Cubic spline interpolant';
137 elseif isequal(fittype1, 1)
138     s1 = 'Shape-preserving interpolant';
139 else
```

```
140     op = '+-';
141     format1 = ['%s %0.',num2str(digits1),'g*x^{%s} %s'];
142     format2 = ['%s %0.',num2str(digits1),'g'];
143     xl = get(axesh1, 'xlim');
144     fit =  fittype1 - 1;
145     s1 = sprintf('y =');
146     th = text(xl*[.95;.05],1,s1,'parent',axesh1, 'vis','off'
        );
147     if abs(coeffs1(1) < 0)
148         s1 = [s1 ' -'];
149     end
150     for i = 1:fit
151         sl = length(s1);
152         if ~isequal(coeffs1(i),0) % if exactly zero, skip it
153             s1 = sprintf(format1,s1,abs(coeffs1(i)),num2str(
                    fit+1-i), op((coeffs1(i+1)<0)+1));
154         end
155         if (i==fit)&&~isequal(coeffs1(i),0)
156             s1(end-5:end-2) = []; % change x^1 to x.
157         end
158         set(th,'string',s1);
159         et = get(th,'extent');
160         if et(1)+et(3) > xl(2)
161             s1 = [s1(1:sl) sprintf('\n      ') s1(sl+1:end)];
162         end
```

```
163     end
164     if ~isequal(coeffs1(fit+1),0)
165         sl = length(s1);
166         s1 = sprintf(format2,s1,abs(coeffs1(fit+1)));
167         set(th,'string',s1);
168         et = get(th,'extent');
169         if et(1)+et(3) > xl(2)
170             s1 = [s1(1:sl) sprintf('\n      ') s1(sl+1:end)];
171         end
172     end
173     delete(th);
174     % Delete last "+"
175     if isequal(s1(end),'+')
176         s1(end-1:end) = []; % There is always a space before
                the +.
177     end
178     if length(s1) == 3
179         s1 = sprintf(format2,s1,0);
180     end
181 end
```